Spiropyran-Functionalized Hydrogels as a Designable Platform for Responsive Nonlinear Optics

Citation

Meeks, Amos. 2021. Spiropyran-Functionalized Hydrogels as a Designable Platform for Responsive Nonlinear Optics. Doctoral dissertation, Harvard University Graduate School of Arts and Sciences.

Permanent link

https://nrs.harvard.edu/URN-3:HUL.INSTREPOS:37368236

Terms of Use

Share Your Story

HARVARD UNIVERSITY

Graduate School of Arts and Sciences

DISSERTATION ACCEPTANCE CERTIFICATE

The undersigned, appointed by the

Harvard John A. Paulson School of Engineering and Applied Sciences
have examined a dissertation entitled:

"Spiropyran-Functionalized Hydrogels as a Designable Platform for Responsive
Nonlinear Optics"

presented by: Amos Meeks

Signature _____

    Typed name: Professor J. Aizenberg

Signature _____

    Typed name: Professor V. Manoharan

Signature _____

    Typed name: Professor M. Kolle

April 20, 2021

Spiropyran-Functionalized Hydrogels as a Designable Platform for Responsive Nonlinear Optics

A DISSERTATION PRESENTED
BY
AMOS MEEKS
TO
THE JOHN A. PAULSON SCHOOL OF ENGINEERING AND APPLIED SCIENCES

IN PARTIAL FULFILLMENT OF THE REQUIREMENTS
FOR THE DEGREE OF
DOCTOR OF PHILOSOPHY
IN THE SUBJECT OF
APPLIED PHYSICS

HARVARD UNIVERSITY
CAMBRIDGE, MASSACHUSETTS
APRIL 2021

Spiropyran-Functionalized Hydrogels as a Designable Platform for Responsive Nonlinear Optics

ABSTRACT

Hydrogels, materials composed of a crosslinked polymer network swollen in water, are an incredibly versatile class of materials, finding applications in fields ranging from ionotronics, to microfluidics, to medicine, to consumer items. This work explores the use of hydrogels in an entirely new area: nonlinear optics. The ability for light-responsive gels to swell or contract due to a local optical field creates an intensity dependent refractive index, resulting in nonlinear optical phenomena including self-trapping, beam bending, spiraling, and spontaneous filamentation. The goal of this thesis is to provide a foundation for the design and application of spiropyran-functionalized, light-responsive hydrogels as nonlinear optical materials.

We will begin by giving a brief overview of nonlinear optical materials and the respective features of their nonlinear optical behavior, including power requirements, reversibility, and long-range interactions between self-trapped beams. This highlights the uniqueness of spiropyran-functionalized hydrogels as a nonlinear optical material that operates reversibly at low laser powers and also demonstrates unique long-range interactions. In Chapter 2 we will establish a basic physical theory of nonlinear optics in spiropyran-functionalized hydrogels, combining spiropyran photoisomerization, environmentally responsive gel poroelasticity, light propagation, and thermal transport. We will show that this model can explain the observed phenomena, and especially that thermal effects are needed to explain novel repulsive and inhibitory long-range interactions.

Chapter 3 builds off of this by considering the ways in which the polymer backbone chemistry can be rationally designed to control the nonlinear optical behaviors of spiropyran-functionalized hydrogels. As examples we show that incorporating N-isopropylacrylamide to change a gel's thermal response can eliminate long-range repulsive interactions and allow for short-range attractive interactions, and that beam bending can be externally controlled by making gels responsive to external thermal or electric fields. In Chapter 4 we turn our focus from the gel's response to the spiropyran chromophore's photoisomerization dynamics, exploring how these dynamics are affected by incorporation into different polymer backbones. We show that there is substantial aggregation of singly-tethered spiropyran even at low concentrations, and that this aggregation has significant affects on the observed photokinetics. Isomerization dynamics are also strongly affected by buffering effects of the polymer backbone, making this a crucial factor to consider when designing a spiropyran-functionalized hydrogel system.

In Chapter 5 we demonstrate spontaneous pattern formation in the form of spatial modulation instability in spiropyran-functionalized hydrogels. While spatial modulation instability is ubiquitous

among nonlinear optical materials, we further demonstrate the tremendous potential of hydrogel-based nonlinear optics by showing that the addition of a diffusing inhibitor can theoretically lead to the formation of optical Turing patterns. Based on the results of the previous chapters we suggest that this could be accomplished with a poly(2-(4-Aminophenyl)ethyl methacrylate) based gel containing both tethered and untethered spiropyran.

Finally we conclude with an outlook on the potential of spiropyran-functionalized hydrogels as nonlinear optical materials. The ability for hydrogel swelling to be responsive to so many different stimuli, such as temperature, humidity, electric fields, magnetic fields, pH, ionic strength, chemical reactions, and specific biomolecules, presents a potential paradigm shift in the way in which nonlinear optics can be coupled to and interact with the environment. These materials have the potential to be the foundation of entirely soft, low-power, non-electronic sensing and computing for soft robotics, microfluidics, or biomedical applications.

Contents

Author List

The following authors contributed to Chapter 1: Derek R. Morim, Ankita Shastri, Andy Tran, Anna V. Shneidman, Victor V. Yashin, Fariha Mahmood, Anna C. Balazs, and Kalaichelvi Saravanamuttu.

The following authors contributed to Chapter 2: Derek R. Morim, Ankita Shastri, Andy Tran, Anna V. Shneidman, Victor V. Yashin, Fariha Mahmood, Anna C. Balazs, Kalaichelvi Saravanamuttu, Rebecca Mac, and Simran Chathanat.

The following authors contributed to Chapter 4: Thomas B. H. Schroeder, Michael M. Lerch

Publication List

Portions of Chapter 1 and Chapter 2 have appeared in the following publication: Morim, D. R. et al. Opto-chemo-mechanical transduction in photoresponsive gels elicits switchable self-trapped beams with remote interactions. *Proc. Natl. Acad. Sci. U. S. A.* 117, 3953–3959 (2020).

Portions of Chapter 3 have appeared in the following publication: Meeks, A., Mac, R., Chathanat, S. & Aizenberg, J. Tunable Long-Range Interactions between Self-Trapped Beams driven by the Thermal Response of Photoresponsive Hydrogels. *Chem. Mater.* 32, 10594–10600 (2020).

Portions of Chapters 3, 4, and 5 are presently unpublished but likely to be included in one or more academic publications in the future.

Listing of figures

To my family.

Acknowledgments

THIS THESIS REPRESENTS THE WORK OF A GREAT MANY PEOPLE, only a fraction of whom I have the space to acknowledge here. First, when beginning my grad school career I was given the advice that the most important factor in choosing a lab is not the particular research subject you pursue, but having a good advisor. I was fortunate enough to get the best of both worlds in Prof. Joanna Aizenberg's lab.

I am also greatly appreciative of the early mentorship I received from Prof. Peter Korevaar. He provided the support I needed to get my feet under me when I first joined the lab. After Prof. Korevaar's departure I have the privilege of receiving mentorship and friendship from two more postdocs, Dr. Thomas Schroeder and Dr. Michael Lerch.

One of the best aspects of the Aizenberg lab is the feeling of really being part of a team, even with so many disparate subjects of research. Lab members are always willing to help each other out to learn a skill or conduct and experiment. I am especially grateful to Dr. Anna Shneidman and Nikolaj Mandsberg for getting me set up to do optics experiments when I had no prior background. I was lucky to also have the support and friendship of the older graduate students, especially Cathy Zhang and Sören Brandt. Thank you to the many other members of the lab who gave me trainings or answered my incessant questions. I hope you all will forgive me for not listing your names explicitly, as that would result in my listing almost every member of the lab over the past five years.

I had the great privilege of mentoring a number of undergraduate researchers during my time in the Aizenberg lab. The works of Rebecca Mac and Simran Chathanat are all included here, but I am also extremely grateful to my earlier mentees, Sahad Vasanji, Michael DiMartino, and Carla Cabal Fernandez, for their unending dedication and enthusiasm.

This work is also the result of several collaborations. Prof. Kalaichelvi Saravanamuttu, Prof. Anna Balazs, and Dr. Victor Yashin all provided crucial mentorship for many aspects of this project. It was also a pleasure to work with Prof. Saravanamuttu's students, Derek Morim and Fariha Mahmood.

While I never met her in person, this work relies heavily on the prior work of Dr. Anikta Shastri. I am grateful to her for meeting with us and answering questions well after she had graduated and moved on, and for writing such a clear and comprehensive thesis. Dr. Shastri's thesis was a guiding star throughout this project.

I would also like to express my gratitude to the small army of people who indirectly supported

1

Introduction

Hydrogel materials composed of 3D polymer networks swollen in water are ubiquitous in nature[1, 2, 3], and are increasingly being used for artificial applications such as super-absorbent materials, drug delivery, wound dressing, environmental sensing, and tissue scaffolding[4]. The equilibrium degree of swelling of a hydrogel is determined by the thermodynamic balance of forces that tend to collapse the polymer network, such as polymer-polymer interactions and the entropic favorability of unstretched chain conformations, and forces that tend to swell the polymer network, such as stronger polymer-

solvent interactions and the osmotic pressure created by charged mobile counterions[5]. So-called responsive hydrogels can be created when the hydrogel materials is designed such that the balance between swelling and contraction is affected by different environmental stimuli, such as temperature, humidity, ionic strength, pH, electric fields, light, and many other potential stimuli[6]. Such responsive hydrogels have been used as the basis for drug-delivery systems[4], soft robotic actuators[7], microfluidic valves[8, 9], sensors[4] and numerous other applications.

This thesis specifically considers light-responsive hydrogel materials that contract due to the isomerization of a photochromic spiropyran molecule[10, 11]. Other types of light-responsive hydrogels have been developed, such as ones using the absorption of light to thermally trigger gel contraction[12, 13], but spiropyran-based gels have the advantage of undergoing much more local photoactuation. The photoresponsivity of spiropyran-functionalized hydrogels (SP gels) is largely attributed to the light-driven isomerization of the hydrophilic, charged, ring-open merocyanine (MCH^+) to the more hydrophobic ring-closed spiropyran (SP) isomer[14, 15, 16, 10, 17, 18, 19] (Figure 1.1A). The decrease in hydrophobicity of the polymer backbone leads to weaker polymer-solvent interactions and thus a shifting of the thermodynamic swelling equilibrium towards a less swollen state. SP gels have been used to create light-responsive microfluidic systems[19, 20, 18, 21, 22], soft robotics[23, 17], and drug delivery systems[24]. However, these applications largely rely on broad actuation of the hydrogel structure. Recent work[14] has shown that the local nature of the light-responsive contractions can create a local intensity-dependent increase in the refractive index, changing the shape of light propagating through the hydrogel and leading to nonlinear optical behavior such as self-trapping of focused laser beams. This makes SP gels an exciting platform for future applications of nonlinear optical phenomena.

Self-trapped light beams and spatial solitons emerge in a rich variety of photoresponsive materials that display intensity-dependent changes in refractive index[25, 26, 27, 28]. These beams propagate without diverging through self-inscribed waveguides and exhibit intriguingly particle-like interactions such as collisions[29], fusion and birth[30], annihilation[31], and spiraling[32], typically in the short-range (where there is significant overlap in their optical fields) and in rare cases, over long distances (where overlap is negligible and beams are remote)[33, 34]. Because they travel without changing shape, self-trapped beams hold potential for optical interconnects[35], applications in image transmission[36], rerouting light[37, 38], and logic gates for computing[33]. Importantly, they form the basis of the next-generation light-guiding-light approach to optical signal processing, which envisions a circuitry-free, reconfigurable and multi-layered photonics technology powered by the dynamic interactions of self-trapped beams[37, 38]. Despite these promising applications, as of yet there does not exist a nonlinear optical material with the combination of properties needed to realize them. In this thesis I hope to show that the tremendous design space of light-responsive, spiropyran-functionalized hydrogels makes them a promising candidate to realize these and other potential applications.

We will start with a brief introduction to the relevant nonlinear optics. Nonlinear optical phenomena occur when the optical properties of a system (e.g. the refractive index n) are modified by the presence of light. This can lead to a large number of interesting phenomena, such as second-harmonic generation, four-wave mixing, self-trapping, modulation instability, and many more[39]. In this thesis we will specifically focus on the nonlinear optical phenomena associated with an intensity-dependent refractive index, $n(I)$, such as self-trapping and modulation instability. The propagation of a beam through such a nonlinear optical medium can be described mathematically with the nonlinear paraxial

wave equation, also known as the nonlinear Schrödinger equation[39]:

$$\frac{\partial A}{\partial z} = \frac{1}{2\mathrm{i}k}\nabla^2_T A - \mathrm{i}k\frac{\Delta n(I)}{n_0}A \tag{1.1}$$

where A is the complex optical field amplitude, z is the direction of propagation, k is the wavenumber ($k = 2\pi/\text{wavelength}$), n_0 is the refractive index of the medium in the absence of light, and $\Delta n(I) = n(I) - n_0$ is the local intensity-dependent change in the refractive index. In the case of a self-trapped beam $\partial A/\partial z = 0$. Solving equation (1.1) with this condition yields solutions with the shape of the Townes profile[27, 40]. However we can estimate the magnitude of Δn needed for self-trapping by using a Gaussian intensity profile of radius w, $A = \sqrt{I_0}e^{-2(x^2+y^2)/w^2}$, and setting $x = y = 0$. Solving for Δn yields the condition:

$$\Delta n = \frac{2n_0}{w^2k^2} \tag{1.2}$$

For a beam radius of $w = 10$ microns, $n_0 = 1.41$, and $k = 2\pi/532$ nm, corresponding to the SP gel experiments described in this work, we find a Δn of only $\approx 2.0 \times 10^{-4}$ is needed for self-trapping.

1.2   NONLINEAR OPTICAL MATERIALS

An intensity-dependent Δn of at least this magnitude can be obtained in a wide variety of different materials due to mechanisms ranging from a nonlinear electronic polarization at high optical field intensities to the change in refractive index that occurs due to light-induced chemical reactions. For applications like sensing or optical computing it is desirable to use a material that undergoes fully reversible self-trapping at low laser powers (mW scale or less, similar to the power of a handheld laser pointer) and, depending on the desired application, shows long-range interactions or response to additional non-optical stimuli. We will briefly review several common types of nonlinear optical materials

4

with an eye towards these desired properties.

1.2.1 Kerr materials

The refractive index of a Kerr material is a linear function of the intensity, $n(I) = n_2 I$, equivalent to a third-order term in the material's polarizability[39]. This nonlinear polarizability can arise from a variety of mechanisms, including a non-quadratic electronic potential, molecular dipole reorientation, and electrostriction[39]. Thus many materials, including crystalline ceramics, glasses, polymers, liquids, and gases have values of n_2 that can lead to significant nonlinear optical behavior at high laser powers (kW to GW)[39]. While Kerr materials include a number of desired nonlinear optical properties, such as an extremely fast, reversible response, the high laser powers required prevent them from being used in most applications. Furthermore, the lack of saturation in the nonlinearity can lead to catastrophic failure, when high-power light becomes so strongly self-focused that it leads to breakdown of the material.

1.2.2 Lead glass

An intensity-dependent refractive index can also arise out of a material's thermal response, such as in the case of lead glass. This has the advantage of being fast and reversible while requiring lower laser powers ($\sim$W) than Kerr materials. Long-range thermal transport can also lead to long-range attraction between self-trapped beams[34]. However, power requirements are generally still too high for broad application, and the use of thermal effects for both local self-trapping and long-range interactions means that the long-range interactions can only be attractive and they cannot be avoided, limiting designability of the nonlinear optical system.

1.2.3 Photorefractive crystals

In photorefractive crystals the intensity-dependent refractive index is achieved through the creation of electron-hole pairs and subsequent charge-separation under a large applied electric field ($\sim$kV/cm). This spatial charge separation creates an internal electric field that then locally effects the refractive index through the Pockels effect[39]. This can lead to self-trapped beams at low laser powers ($\sim$ μW)[41], and the diffusion of charge carriers outside of the applied optical field can lead to long-range interactions[42]. However, the demanding requirements for nonlinear optical behavior in photorefractive crystals, such as high applied fields and specific orientation with respect to the crystal's optical axis, limits their practical application.

1.2.4 Liquid crystals

Liquid crystals are an extremely versatile nonlinear optical material, and they have already been used to demonstrate optical logic gates[33] and optical Turing patterns[43]. The intensity-dependent refractive index in liquid crystal systems arises from the combination of the molecular birefringence of the liquid crystal molecules and the tendency for liquid crystal molecules to align themselves with an applied electric field. Thus a thin film of liquid crystal will align under an electric field, and when light is shone into the film with a polarization angle slightly different from the overall alignment, this will locally cause liquid crystal molecules to align with the polarized light, increasing the refractive index compared to areas that are not aligned.

These systems use low laser power ($\sim$mW) and are fully reversible, while the elastic propagation of liquid crystal alignment direction can lead to long-range interactions between beams[44]. However, the nonlinear optical behavior in liquid crystal systems relies on a significant amount of external equipment and related symmetry-breaking, such as the requirement for an applied field, polarized light, and control of the relative angle between the two.

1.2.5 Photochemical systems

An additional class of nonlinear optical systems are systems in which a photochemical reaction locally changes the refractive index. Two examples are photopolymerizing systems[45, 46, 47, 26, 35] and the photochemical oxidation of I^- to I_3^- [48]. Photopolymerizing systems show nonlinear optical behavior even at extremely low laser powers ($\sim$nW) due to the compounding and irreversible nature of photopolymerization. However, this irreversibility makes them unsuitable to optical computing applications, although it can be used to fabricate photonic structures from the bottom up[47, 35]. The iodide-based photochemical systems show short-term reversibility due to the diffusion of I_3^- away from the light beam, but the nonlinear optical response degrades as I^- is consumed.

1.3 Spiropyran-functionalized hydrogels as nonlinear optical materials

Overall there is still a need for nonlinear optical materials that operate reversibly at low laser powers to serve as a foundation for functional nonlinear optical devices. The light-responsive, spiropyran-functionalized hydrogels described here have the potential to serve as this foundation. The spiropyran photoisomerization is fully reversible and has a high degree of robustness when integrated into the polymer network[10]. The bulk contraction of SP gels demonstrated previously[15] is more than enough to lead to self-trapping, and as we will demonstrate throughout this thesis the hydrogel nature of these gels allows for a wide variety of designable nonlocal interactions.

Figure 1.1 provides an overview of the spiropyran-functionalized gels first used to demonstrate self-trapping, reversibility, and interactions between beams. An acrylated spiropyran moiety was copolymerized with acrylamide (AAm) and acrylic acid (AAc) monomers with a methylenebisacrylamide crosslinker (see Appendix A for detailed materials and methods). UV-vis spectroscopy showed absorption peaks characteristic of the MCH^+ isomer that could be reversibly depleted upon irradiation with visible light. A 6 mW 532 nm laser focused down to a 20 μm $1/e^2$ beam width on the entrance
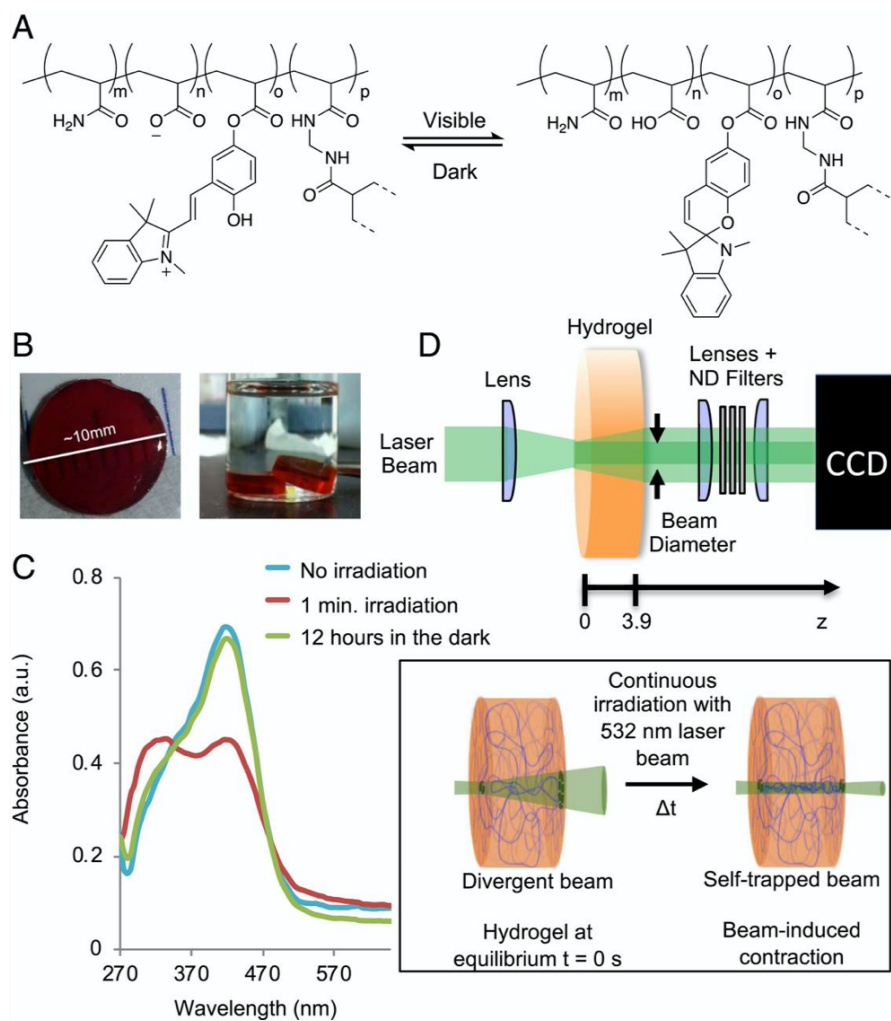
Figure 1.1: Overview of spiropyran-functionalized hydrogels. **(A)** Photoisomerization scheme of chromophore substituents from the protonated merocyanine (MCH$^+$, Left) to ring-closed spiropyran (SP, Right) forms in the methylenebis(acrylamide) cross-linked poly(AAm-co-AAc) hydrogel. **(B)** Photographs of chromophore-containing poly(AAm-co-AAc) hydrogel monoliths employed in experiments. **(C)** UV-visible absorbance spectra demonstrating reversible isomerization of MCH$^+$ (absorption $\lambda_{max} = 420$ nm) to SP ($\lambda_{max} = 320$ nm) in solution. **(D)** Experimental setup (Top) to probe laser self-trapping due to photoinduced local contraction of the hydrogel, schematically depicted on the Bottom. A laser beam is focused onto the entrance face of the hydrogel while its exit face is imaged onto a CCD camera. Figure reproduced from [14].
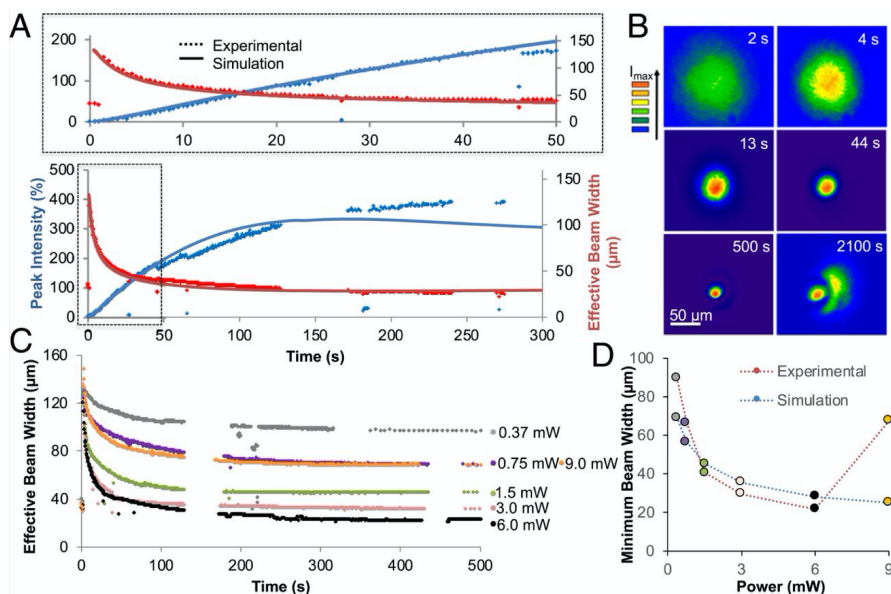
Figure 1.2: Evolution of self-trapping in the SP-modified hydrogel; experiments and simulations. **(A)** Experimentally measured temporal evolution of peak intensity (blue) and effective width (red) of a laser beam (532 nm, 6.0 mW, with a width of 20 µm, corresponding peak intensity = 3.77 kW cm^2) acquired at the sample exit face; the beam is turned on at $t = 0$. Breaks in plots are time lapses between image logs. The experimental plots (dotted lines) are compared to numerical simulations (solid lines); the dashed black box above provides a zoomed-in view from 0 to 50 s, emphasizing the match between the experimental results and simulations. **(B)** Two-dimensional (2D) spatial intensity profiles experimentally acquired at select times. **(C)** Temporal evolution of beam width during self-trapping experiments at different optical powers. **(D)** Comparison of calculated and experimental values of minimum self-trapped beam width as a function of beam power. Figure reproduced from [14].

face of an SP gel was observed to undergo self-trapping on a timescale of minutes (Figure 1.2), and this process was found to be highly repeatable (Figure 1.3).

We also observe inhibitory and repulsive interactions between self-trapped beams in spiropyran-functionalized poly(AAm-co-AAc) gels at ranges of up to 10 times the beam width (Figure 1.4). In Chapter 2 we develop a physical model of single-beam self-trapping and long-range two-beam interactions. We will show that while the gel's swelling response to light is sufficient to explain single-beam self trapping, it cannot explain long-range interactions. These are instead explained by the gel's thermal response. This is a significant departure from long-range interactions in other nonlinear optical materials like lead glass, photorefractive crystals, and liquid crystals, as in SP gels the long-range interac-
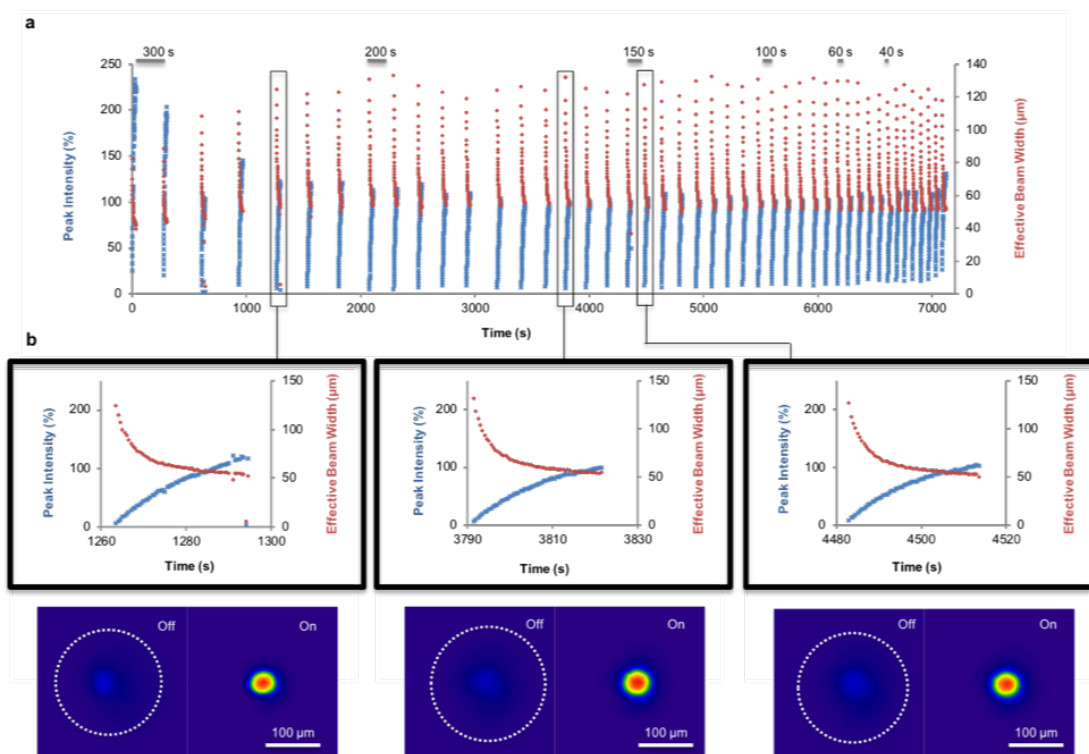
Figure 1.3: Rapidly reversible self-trapping in the SP-modified p(AAm-co-AAc) gels. **(A)** Temporal plots of peak intensity (blue) and effective diameter (red) over 45 cycles of self-trapping of a laser beam. Cycles of 30 s were separated by dark periods ranging from 300 to 40 s (indicated above the plots). **(B)** Scheme and spatial intensity profiles showing the "off" (divergent) and "on" (self-trapped) states of the laser beam over select cycles. White circles trace the diameter ($1/e^2$) of the initially divergent beam in the off state. Figure reproduced from [14].

tions are caused by a secondary field rather than the primary field that drives single beam self-trapping. This allows for long-range repulsive interactions, while previous long-range nonlinear optical interactions in materials like lead glass or liquid crystals are attractive by necessity.

In chapter 3 we build off of this insight to show how a gel's response to secondary stimuli can be tuned by changing the gel chemistry, allowing for long-range interactions to be designed and for self-trapped beams to bent by external stimuli, such as a thermal gradient or electric field. These experiments demonstrate the tremendous potential for spiropyran-functionalized hydrogels to serve as a designable platform for nonlinear optical applications that involve interaction with external systems, such as in sensing, soft robotics, or interactions between different components in all-optical computing applications.

In chapter 4 we explore the interactions between the gel chemistry and the spiropyran photoisomerization chemistry. We observe surprising triexponential dynamics that are well-explained by a model that includes slower aggregation and protonation of the ring-open merocyanine (MC) isomer. We conclude that aggregation and protonation rates are both significantly affected by the gel chemistry, primarily through the buffering effect of charged polymer moieties, providing insight for how choices in polymer chemistry will affect the spiropyran photoisomerization dynamics.

In chapter 5 we explore spontaneous optical pattern formation in SP gels. We observe a spatial modulation instability, a process by which small variations in a broadly uniform optical intensity profile lead to self-reinforcing filamentation of the light, in poly(N-isopropylacrylamide-co-AAc) gels. The observations are well-explained by a linear stability analysis of the self-trapping model presented in Chapter 2. We then go one step further and, using all of the insights of the previous chapters, demonstrate the potential for tethered and untethered spiropyran in an aniline-functionalized poly(2-(4-Aminophenyl)ethyl methacrylate) (poly(APEMA)) gel to form optical Turing patterns, in which local self-focusing is coupled to long-range inhibition to create patterns with a much sharper characteristic wavelength compared to spatial modulation instability.
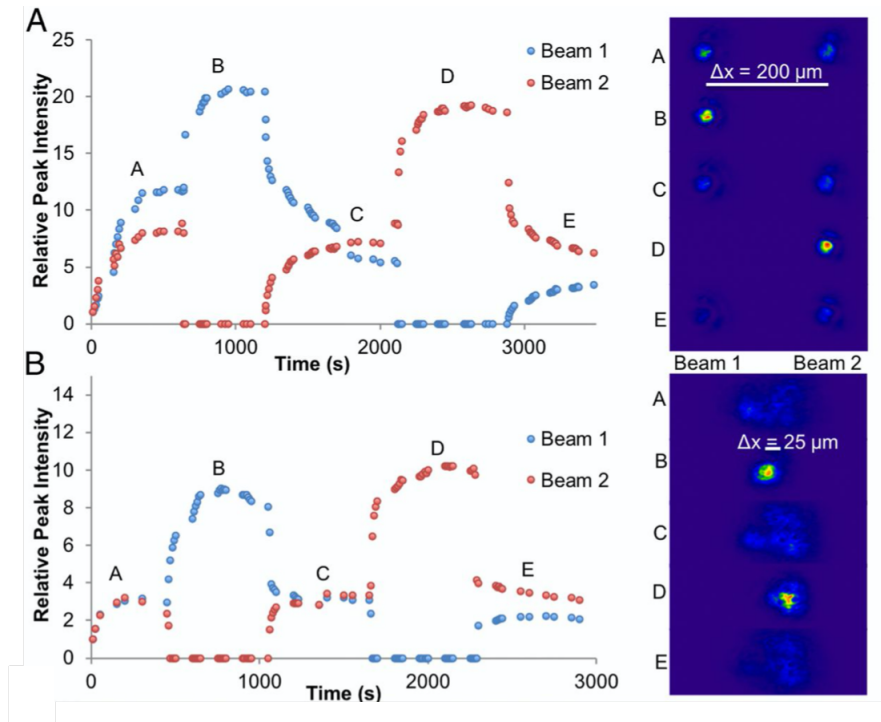
Figure 1.4: Dynamic interactions of two parallel self-trapped beams. **(A)** Temporal plots of relative peak intensities (Left) and corresponding 2D spatial intensity profiles (Right) acquired at select times at the sample exit face for two beams separated by $\Delta x \approx 200$ µm. When propagating together, beam 1 (blue) and beam 2 (red) self-trapped over 625 s to a relative peak intensity of 12 and 9, respectively (from an initial value of 1), and comparable widths of ~ 40 µm (labeled as region A on the plot and intensity profile). When beam 2 was selectively blocked, beam 1 rapidly returned to high self-trapping efficiency, increasing in relative intensity to ~ 20 with a minimum width of ~ 28 µm over 250 s (labeled as region B). When beam 2 was reintroduced, however, beam 1 diminished in self-trapping efficiency, decreasing in relative peak intensity to 5.3 and broadening again to ~ 40 µm over 800 s; beam 2 also showed reduced efficiency, attaining a maximum relative peak intensity of only 7 and a width of ~ 40 µm (region C). The equivalent effect was observed when beam 1 was blocked in the next cycle of the same experiment (region D). **(B)** Temporal plots of relative peak intensities and corresponding 2D spatial intensity profiles for two beams separated by $\Delta x = 25$ µm. Figure reproduced from [14].

Finally we conclude with an outlook on future work and potential applications of rationally designed nonlinear optical materials based on SP gels. The tunable long-range interactions of these materials makes them ideally suited to potential applications in all-optical computing. Furthermore, the large design space of potential stimuli, such as electric fields, magnetic fields, pH, and specific biomolecules, makes SP gels a promising platform for sensing, especially in situations requiring entirely-soft materials or where traditional electronic sensors are difficult, such as microfluidics or soft robotics. We also suggest that the rationally designable bottom up pattern formation explored in Chapter 5 could lead to photomasks for creating micron scale patterns over large and complicated surface topologies. In all of these potential applications the insights from this thesis on how to rationally design and model SP gel systems will serve as an important foundation.

2

Nonlinear Optics of
Spiropyran-Functionalized Hydrogels

IN THE PREVIOUS CHAPTER WE SHOWED how spiropyran-functionalized hydrogels (SP gels) are
light-responsive and show robust nonlinear optical behavior in the form of self-trapped beams. These
novel materials provide a combination of low power, reversibility, processability, ease of use, and tun-

able coupling to external stimuli that is not seen in any other nonlinear optical system. This unique combination makes them potentially useful in applications like sensing or optical computing. However, in order for this potential to be realized the physical underpinnings of the nonlinear phenomena in SP gels must be understood well enough to be predicted and designed.

There are a wide range of physical processes that may contribute to and effect the nonlinear optical behavior of SP gels. Irradiation of the SP gel with light causes a ring-closing isomerization that changes hydrophilicity but can also release a diffusing proton that changes the local pH (Figure 1.1A). Absorption of light can also lead to local heating, which may effect the swelling of the gel or the SP isomerization rates. Furthermore, contraction of the gel in one area results in the expulsion of water into surrounding areas, causing those areas to swell, and potentially influencing the dynamics of other nearby beams. All of these processes are complex and interrelated.

The goal of this chapter is to lay the foundation for understanding and designing the processes that lead to the nonlinear optical behavior of SP gels. We will start by considering a minimal model necessary to reproduced the experimentally observed phenomena of optical spatial solitons in SP gels. While other work has modeled the intensity-dependent deformations of light-responsive hydrogels[49, 50], none of this work has considered the feedback of gel swelling dynamics on the propagation of light.

Our minimal model will be sufficient to explain single-beam dynamics, but we will also show that it is not able to replicate the fast, long-range interactions between self-trapped beams. We find that these long-range interactions are driven by the response of the gel to temperature increases induced by absorption of the incident light. With this element we show how the nonlinear optical dynamics of self-trapped beams in SP gels is intimately linked with the gel's response to additional stimuli, with significant implications for the design of SP gel systems for applications like optical computing and sensing.
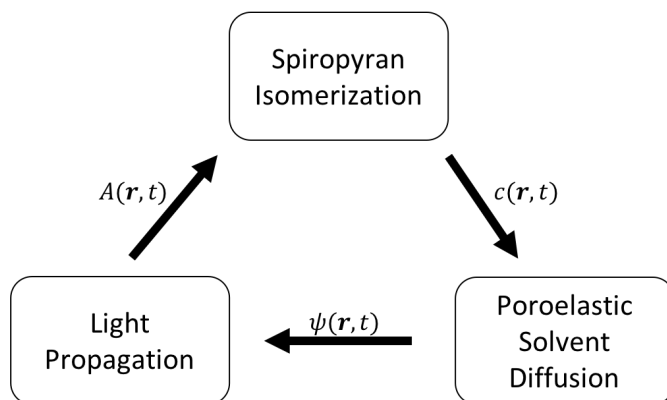
Figure 2.1: Proposed minimal model of opto-chemo-mechanical feedback leading to self-trapping and other nonlinear optical behaviors of SP gels. The three variables are c, the normalized concentration of ring-closed SP; ψ, the normalized change in the volume fraction of polymer; and A, the optical field. An incident optical field A produces local changes in c through the process of spiropyran isomerization (Equation (2.2)), which then drives changes in ψ governed by the process of poroelastic diffusion (Equation (2.5)). Local changes in ψ then lead to local changes in the refractive index, $n(\psi)$, which affects the propagation of light through the materials as determined by the nonlinear Schrödinger equation (Equation (2.7)).

2.1 Minimal Model of Self-trapping in SP Gels

We propose that self-trapping in SP gels is driven by the opto-chemo-mechanical feedback shown in Figure 2.1. In this model, photoisomerization of the spiropyran chromophore from the hydrophilic ring-open merocyanine (MC) or protonated merocyanine (MCH$^+$) form to the hydrophobic ring-closed spiropyran (SP) form leads to the local expulsion of water and densification of the polymer network. Due to the higher refractive index of the polymer compared to water, this locally raises the refractive index compared to regions without significant photoisomerization. This creates a refractive index gradient Δn that bends light towards regions of higher n as it propagates through the material, leading to local concentration of light that triggers further photoisomerization, completing the feedback loop. Each of these processes is presented in detail below.

For the sake of this minimal model we will refer to MC and MCH$^+$ collectively as MC and consider only the light-driven ring-closing isomerization of MC to SP, and the corresponding thermally driven ring-opening of SP to MC. A fuller description of the isomerization dynamics of spiropyran in hydrogels is presented in chapter 4 and includes the protonation and aggregation of MC. This lumping of MC and MCH$^+$ is valid for the relatively long timescales in acidic environments considered here, due to the relatively fast rates of protonation and deprotonation. For now we consider the simple equilibrium reaction:

$$\text{MC} \underset{\Delta}{\overset{h\nu}{\rightleftharpoons}} \text{SP}$$
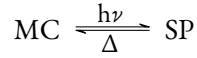
MC is converted to SP at a rate $k_{MC \to SP}$ that is linearly dependent on the local intensity: $k_{MC \to SP} = k_1 I(\mathbf{r})$, while SP thermally converts to MC at a rate $k_{SP \to MC}$. Denoting the local concentration of SP by C and normalizing it by the total chromophore concentration C_0 we can define the local isomerization percentage:

$$c(\mathbf{r}, t) = \frac{C(\mathbf{r}, t)}{C_0} \tag{2.1}$$

In order to write an expression for the total change in the local spiropyran concentration it is important to note that the chromophore is attached to the polymer backbone and thus as the polymer becomes more concentrated so too does the chromophore. With this we can write:

$$\frac{\partial c(\mathbf{r}, t)}{\partial t} = -\nabla \cdot \left(c(\mathbf{r}, t) \mathbf{J}_\psi \right) + k_1 I \left(1 + \psi(\mathbf{r}, t) - c(\mathbf{r}, t) \right) - k_{SP \to MC} c(\mathbf{r}, t) \tag{2.2}$$

Where ψ is the relative variation of polymer volume fraction φ from the equilibrium dark value

φ_{eq}, defined as:

$$\psi(\mathbf{r}, t) = \frac{\varphi(\mathbf{r}, t) - \varphi_{\text{eq}}}{\varphi_{\text{eq}}} \tag{2.3}$$

And $\mathbf{J}_\psi$ is the polymer flux, which is defined by the poroelastic dynamics of the gel.

2.1.2 POROELASTIC GEL DYNAMICS

Our model of gel dynamics follows the model of light-responsive hydrogels previously laid out by Yashin and Balazs[51], and Kuksenok and Balazs[49]. It uses a neo-Hookean model for the stretching of polymer chains and assumes that gel deformations are small, which is valid for the observed stretches on the order of a few percent or less as is discussed later with respect to Figure 2.8. The isomerization of MC to SP is assumed to produce an isotropic osmotic pressure with magnitude $\chi_{SP}\varphi C_0 c$. χ_{sp} is the parameter that reflects the strength of the change in hydrophilicity between MC and SP. This results in an expression for the polymer flux:

$$\mathbf{J}_\psi = -\Lambda[(\lambda + 2\mu)\nabla\psi(\mathbf{r}, t) - \chi_{\text{sp}}C_0\varphi_{\text{eq}}\nabla c(\mathbf{r}, t)] \tag{2.4}$$

Where λ and μ are Lamé's first and second parameters respectively, and Λ is the kinetic coefficient defined as

that is related to the friction between the solvent and the polymer. From this we can write the expression for the change in the relative polymer volume fraction:

$$\frac{\partial\psi(\mathbf{r}, t)}{\partial t} = -\nabla \cdot \mathbf{J}_\psi = \Lambda[(\lambda + 2\mu)\nabla^2\psi(\mathbf{r}, t) - \chi_{\text{sp}}C_0\varphi_{\text{eq}}\nabla^2 c(\mathbf{r}, t)] \tag{2.5}$$

We see that the gel dynamics consist of a diffusive equation where areas of concentration in the polymer volume fraction spread out with a poroelastic diffusivity of $D_p = \Lambda(\lambda + 2\mu)$, while the

light-driven isomerization of MC to SP causes the gel to locally concentrate. The strength of the gel's light response can be characterized by the dimensionless parameter

$$\kappa = \frac{\chi_{sp} C_0 \varphi_{eq}}{\lambda + 2\mu} \tag{2.6}$$

2.1.3 Light Propagation

Previous work has considered the dynamics of SP gels to a prescribed static intensity profile[49]. However, modeling the nonlinear dynamics of these materials requires modeling the effect of changes in the gel swelling on the light propagation through the material. This is commonly done using the nonlinear paraxial wave equation, also known as the nonlinear Schrödinger equation, presented here with an additional absorption term:

$$\frac{\partial A}{\partial z} = \frac{1}{2ik} \nabla_T^2 A - ik \frac{\Delta n(\psi)}{n_0} A - \alpha(c) A, \tag{2.7}$$

where A is the complex field amplitude normalized by a factor of $2/n_0 \varepsilon_0 c$ such that $|A|^2 = I$, z is the direction of propagation, k is the wavenumber ($k = 2\pi/\text{wavelength}$), $\alpha(c)$ is the isomerization-dependent absorption coefficient of the SP gel, defined as:

$$\alpha(c) = \alpha_0 + (\alpha_1 - \alpha_0)c \tag{2.8}$$

Which assumes that the absorption is linearly dependent on c with a value α_0 when $c = 0$ and α_1 when $c = 1$. This arises because the ring-open form is much more absorbing than the ring-closed form, but at complete isomerization there will be other sources of loss, such as scattering.

n_0 is the refractive index of the gel at equilibrium under dark conditions, and the change in the

19

index of refraction Δn is defined as:

$$\Delta n = (n_p - n_s)\varphi_{\text{eq}}\psi \tag{2.9}$$

where n_p is the refractive index of the pure polymer. We use a value of $n_p = 1.49$ based on an average of the refractive index of poly(acrylamide) (1.45) and poly(acrylic acid)[52]. We used $n_s = 1.33$ as the refractive index of water. The transverse Laplacian ∇_T^2, defined as:

$$\nabla_T^2 = \frac{\partial^2}{\partial x^2} + \frac{\partial^2}{\partial y^2} \tag{2.10}$$

arises because the nonlinear paraxial wave equation assumes that the angle between the optical axis z and the wave vector $\mathbf{k}$ is small, meaning that $|\frac{\partial^2 A}{\partial z^2}| \ll |k\frac{\partial A}{\partial z}|$. Overall equation (2.7) can be understood as the light intensity diffusing and spreading out as it propagates, while also concentrating and bending towards regions of higher refractive index.

2.1.4 BOUNDARY CONDITIONS, INITIAL CONDITIONS, AND NUMERICAL SOLVING

The three equations (2.2), (2.5), and (2.7) constitute our minimal model of the feedback loop in SP gels that leads to nonlinear optical phenomena. To complete this model for numerical simulation we need to specify boundary conditions and initial conditions. For simplicity we assume that the gel is affixed to a wall, meaning that $\psi = 0$ and $\mathbf{n} \cdot \nabla(\psi - \kappa c) = 0$ (where $\mathbf{n}$ is the unit vector normal to the gel surface) at the boundaries. We justify this by observing that in the simulations the effects of the boundaries do not penetrate deeply into the bulk of the gel. For light propagation the boundary conditions are $A = 0$ at infinity. For initial conditions we set $\psi = 0$ and $c = 0$ everywhere, and we have a Gaussian intensity input $A = \sqrt{I_0}e^{\frac{-2(x^2+y^2)}{w_0^2}}$ at $z = 0$, where I_0 is the initial peak intensity of the beam and w_0 is the waist radius of the Gaussian beam focused onto the entrance face of the gel.

2.1.5 Parameter values

All parameter values utilized in the model are shown in Table 2.1. λ and μ were estimated based on the measured modulus of elasticity of the spiropyran-doped poly(AAm-co-AA) gels[53] and the Poisson ratio of similar poly(AAm) gels[54, 55]. The kinetic coefficient Λ was estimated by measuring the poroelastic diffusivity using the method of Hu et al[56] (See Appendix B for details). χ_{sp} was treated as a fitting parameter. C_0 and φ_{eq} are assumed to be equal to their values in the prepolymer solution, while k, I_0, and w_0 are prescribed by the optical setup of the experiments.

Parameter	Value Used	Units
φ_{eq}	0.4	-
Λ	6×10^{-16}	$m^2 \, Pa^{-1} \, s^{-1}$
C_0	14	mM
λ	58	kPa
μ	3.4	kPa
χ_{sp}	71.43	$kPa \, M^{-1}$
k_1	1.53×10^{-7}	$m^2 \, W^{-1} \, s^{-1}$
$k_{SP \rightarrow MC}$	0.015	s^{-1}
k	1.2×10^7	m^{-1}
α_0	1200	m^{-1}
α_1	800	m^{-1}
n_p	1.49	-
n_s	1.33	-
I_0	0.24×10^7 to 5.7×10^7	$W \, m^{-2}$
w_0	1×10^{-5}	m

Parameter	Value Used	Units

Table 2.1: Parameter values used in the minimal model of self-trapping.

The reaction rates k_1 was estimated by matching the initial rate of self-focusing while $k_{SP \to MC}$ was estimated based on the observation from repeated self-trapping experiments that full relaxation of the gel does not occur for dark periods of 60 s or less (Figure 1.3). Assuming that the SP→MC isomerization limits the relaxation time gives an isomerization timescale of approximately $1/60$ s ≈ 0.015 s^{-1}.

The refractive index of the polymer n_p was taken to be an average of the index of poly(acrylic acid) (1.53) and poly(acrylamide) (1.45) while n_s is the refractive index of water (1.33). The optical loss coefficient α_0 was estimated based on measurements of the relative initial maximum beam intensity after passing through the sample compared to the intensity of the beam passing through the sample holder filled with water only. α_1 was chosen to match the experimental rate and extent of self-trapping.

2.1.6 MODEL EVALUATION

The model was implemented in Mathematica version 11.1.1 and solved numerically using the built in NDSolve differential equation solver. Single beam simulations were carried out by employing cylindrical coordinates while double beam simulations employed a 2D coordinate system. Because the light responds effectively instantaneously to changes in the gel swelling simulation was done in an iterative manner where an intensity profile throughout the gel was calculated based on the value of $\psi(\mathbf{r})$ at a particular time, then this intensity profile was used to solve for changes in $c(\mathbf{r}, t)$ and $\psi(\mathbf{r}, t)$ over a timestep Δt. This process was repeated until the final time was reached.

2.1.7 Model results

This model accurately captures the short-term (< 500 s) self-trapping dynamics along with the intensity-dependent self-trapping efficiency of a single laser beam in the hydrogel (Figure 2.2). As in experiments, the simulated self-trapping efficiency increases monotonically with beam power spanning 0.37 mW to 6.0 mW. This trend originates from the intensity-dependence of the photoisomerization process: at lower intensities, the proportion of merocyanine isomerized to spiropyran does not extend far enough into the hydrogel to create the Δn needed for appreciable self-trapping, while at higher intensities the concentration of isomerized spiropyran molecules rapidly saturates to a plateau in self-trapping efficiency.

The strength of self-trapping in SP gels is found to decrease at intensities above 6.0 mW. This is due to the saturation of isomerization at the beam center at large intensities combined with significant isomerization that occurs in the lower-intensity tails of the beam. This forms a flat-top concentration profile that extends beyond the beam width, creating a wider waveguide that supports higher-order optical modes[57]. This phenomena is captured by the model, although the perfect cylindrical symmetry of the model leads to a less extreme drop in self-trapping efficiency (Figure 2.3).

2.2 Interactions between self-trapped beams

Self-trapped beams in spiropyran-functionalized poly(AAm-co-AAc) gels have been observed to undergo significant mutual inhibition (Figure 2.4) and repulsion (Figure 2.5) over the short range ($\sim$beamwidth) and the long range ($\sim 10\times$ beamwidth)[14, 58]. Such repulsive long-range interactions are unique among nonlinear optical materials, where previously only attractive long-range interactions have been reported[34, 42, 33]. Repulsive or inhibitory long-range interactions are potentially interesting for all-optical computing and logic gates.

While the model presented in section 2.1 is able to capture many of the dynamics of single-beam

24
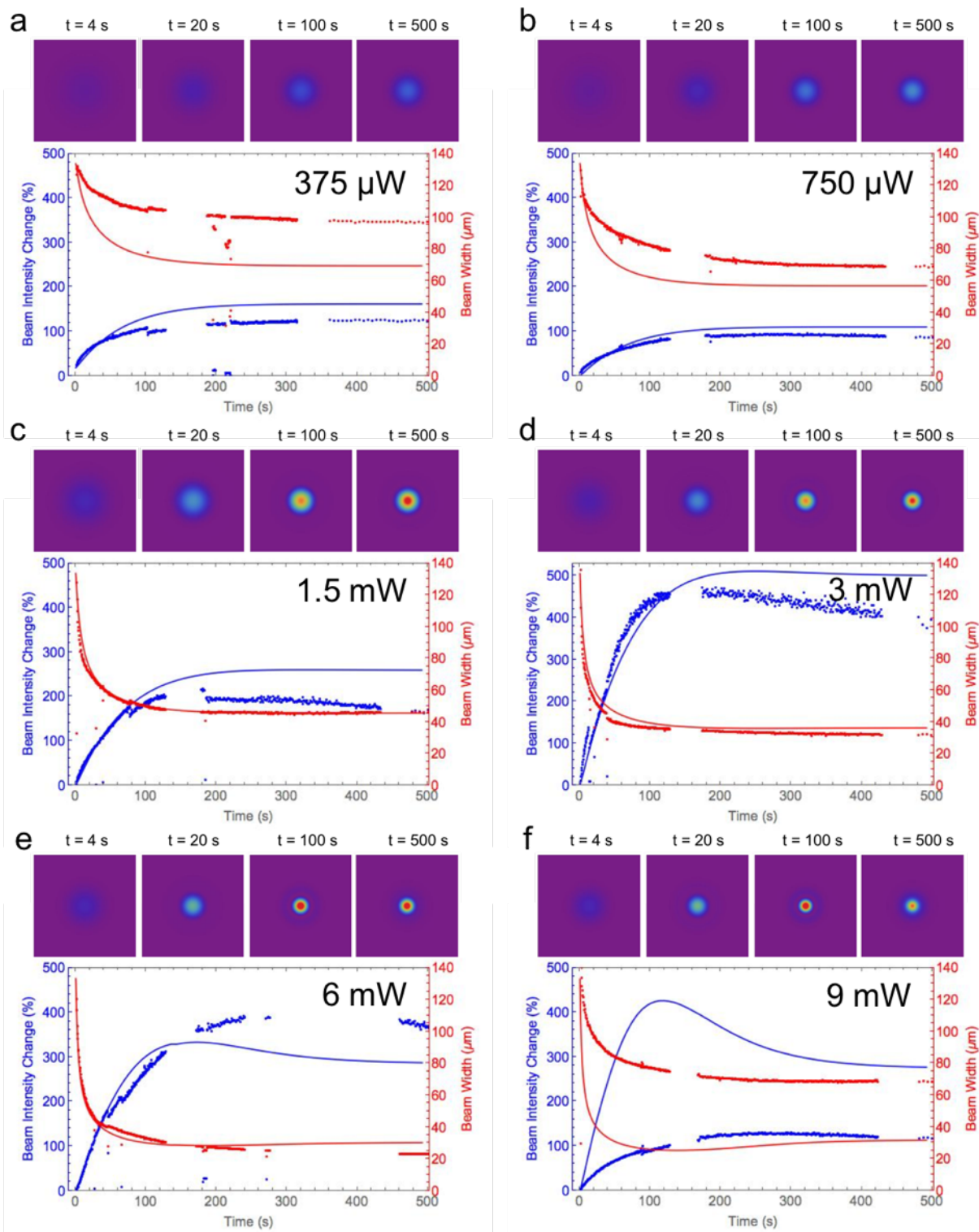
Figure 2.2: Simulated spatial intensity profiles for the self-trapping of light in spiropyran-modified p(AAm-co-AAc) and the corresponding peak intensity (blue, solid line is simulated) and beam diameter (red, solid line is simulated) as a function of time. Incident beam power is (a) 0.37 mW, (b) 0.75 mW, (c) 1.5 mW, (d) 3 mW, (e) 6 mW, and (f) 9 mW.
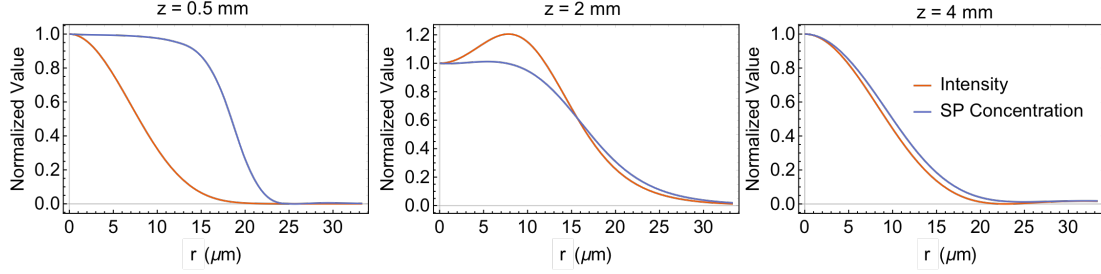
Figure 2.3: Simulated spiropyran concentration and intensity profile within the SP-modified p(AAm-co-AAc) gel at $t = 100$ s and $z = 0.5, 2$, and 4 mm. The simulated beam power is 6 mW. Towards the entrance face of the gel we see the clear creation of a flat-top profile of spiropyran isomerization, with almost complete isomerization even on the tail of the Gaussian intensity profile. Δn is small within the flat top profile, allowing the light to spread as it propagates through the gel until it encounters a steep n gradient, leading to the ring formation seen at $z = 2$ mm. As the intensity decreases due to absorption the flat top profile diminishes, but a faint ring at the exit face of the gel ($z = 4$ mm) is still seen at around 30 μm from the beam center.

self-trapping in p(AAm-co-AAc) SP gels, it is not able to capture the long-range interactions of multiple beams, as illustrated in Figure 2.4. In experiments beams separated by 25 and 200 μm are observed to repel each other on a timescale of seconds (Figures 2.4D and 2.5). Modeled beams reproduce similar interactions short length scales (Figure 2.4A and B) but they do not significantly interact at longer length scales (Figure 2.4C). This suggests that the minimal model presented above is still lacking some significant aspect of the dynamics of self-trapped beams in SP gels.

Analysis of the interaction timescale suggests that the missing process is thermally driven. We consider three different transport processes that may play a role in long-range beam interactions: i) water transport within the gel mediated by poroelastic diffusion, ii) heat transport through thermal diffusion, and iii) chemical diffusion of protons released by the conversion of MCH+ to SP, which would be expected to locally swell the gel due to the osmotic pressure effect of mobile counterions in the polyelectrolyte gel[59].

We can estimate the interaction timescale for each of these three processes (poroelasticity, thermal diffusion, and chemical diffusion) by considering that they are all governed by diffusion equations of the form $\frac{\partial^2 P}{\partial t^2} = D\nabla^2 P$, where P is the quantity of interest (pressure, temperature, or concentration)
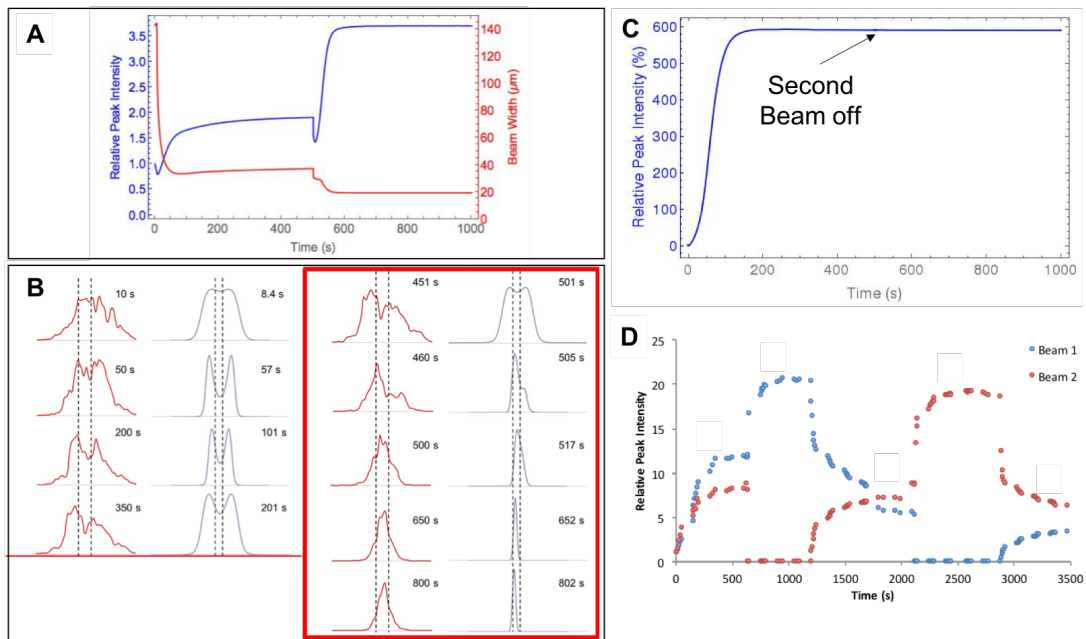
Figure 2.4: Two beam interactions, simulations and experiments. **(A)** Simulated relative peak intensities and corresponding beam widths for two co-propagating 6.7 mW beams with a separation of 25 μm. The second beam is turned off at 500 s, resulting in full self-focusing of the remaining beam. **(B)** Comparison between transverse intensity cross-sections on the outlet face of the gel in experiment (left columns) and simulation (right columns). The red box denotes when the beam on the right side (Beam 2) is blocked. Beams are observed in both cases to initially focus and repel each other, and when one beam is blocked the remaining beam bends towards the blocked beam's position. **(C)** Simulated relative peak intensities and corresponding beam widths for two co-propagating 6.7 mW beams with a separation of 200 μm. The second beam is turned off at 500 s with no significant impact on the remaining beam. **(D)** Experimental peak intensity of two co-propagating 6 mW beams separated by a distance of 200 μm. Beams respond significantly and within seconds of the other beam being turned off or on. Figure reproduced from [14].
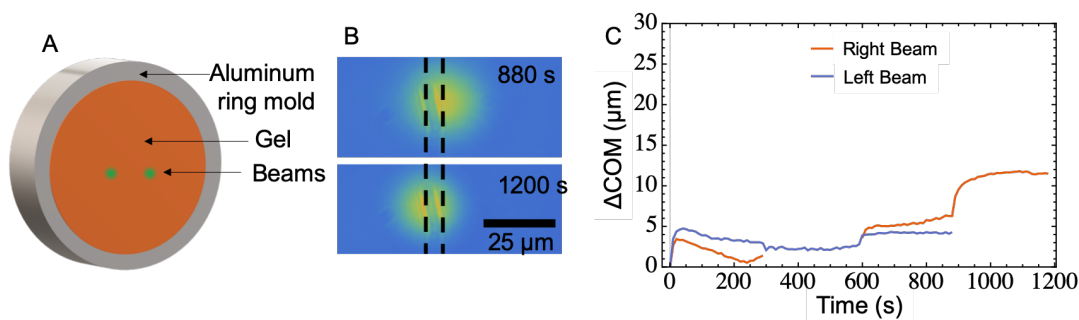
Figure 2.5: Long-range repulsions of self-trapped beams in SP gels. **(A)** Diagram of two-beam experiment with beams separated by a distance of 200 μm. **(B)** Still images of the right beam showing the change in beam center in response to the left beam being switched off. **(C)** Change in the center of mass of each beam over time. Beams are bent away from the other beam when it is on, and move towards the direction of the other beam when that beam is off. Reprinted with permission from *Chem. Mater.* 2020, 32, 24, 10594–10600[58]. Copyright 2020 American Chemical Society.

as a function of time t and space, and D is the corresponding diffusivity. This means that in all cases the expected timescale for interaction given a beam separation of distance L is $\tau = L^2/D$. Poroelastic diffusivities for the spiropyran-functionalized gels were measured (Appendix B), while the chemical diffusivity was assumed to be on the order of $10^{-9}\,\mathrm{m^2\,s^{-1}}$ [60] and the thermal conductivity was found in the literature to be $0.4\,\mathrm{W\,m^{-1}\,K^{-1}}$ for similar gels[61]. For $L \sim 10^{-4}$ m, this gives a poroelastic interaction timescale of $\tau_P \sim 10^3$ s, a chemical interaction timescale of $\tau_C \sim 10^1$ s, and a thermal interaction timescale of $\tau_T \sim 10^{-1}$ s. It can be seen from Figures 2.5 that one beam responds to a second beam being switched on in < 1 s, suggesting that thermal effects must be the primary physical process resulting in long-range beam interactions.

We also show that the observed long-range interactions cannot be explained by scattered light. This is clear from three different arguments: 1) the intensity of scattered light is too low to create significant interactions on a reasonable timescale; 2) optical interactions should lead to attractive interactions, contrary to the observed repulsive interactions; and 3) scattered light interactions would be expected to be stronger in the less absorbing spiropyran-functionalized poly(N-isopropylacrylamide-co-acrylic acid) (poly(NIPAAm-co-AAc)) hydrogels, while observed interactions are weaker in these gels.

First, we consider the intensity of scattered light. We assume that scattering is uniform from the cylindrical beam and find that

$$\frac{I(R)}{I_0} = \frac{\alpha_0 w^2}{2R} \approx 1 \times 10^{-4} \tag{2.11}$$

Where $I(R)$ is the intensity of scattered light at a distance R away from the beam, I_0 is the peak intensity of the beam from which light is scattering, w is the width of the cylindrical beam, and α_0 is the scattering coefficient. We can get a high estimate for the intensity of the scattered light by assuming that all power loss as the beam propagates through the gel is due to scattering. The loss coefficient was previously shown to be about 800 m^{-1} (Table 2.1). Using this value for α_0, a beam width of 20 μm, and a distance R of 200 μm we get an intensity ratio on the order of 1×10^{-4}. Noting that the timescale of self-trapping dynamics are inversely proportional to light intensity, and that self-trapping occurs on a timescale of $\sim 10^1$ s, this suggests that beam interactions mediated by scattered light would occur with a timescale of $\sim 10^5$ s, which is not consistent with the observed large and fast interactions.

Second, we point out that light causes the gel to contract, which increases the refractive index. Thus any scattered light from a co-propagating beam should contract the gel more in the direction of the beam, which would bend the beams towards each other and lead to an attractive interaction. This is at odds with the observed repulsive interactions.

Finally, we consider that, in addition to scattering, these gels absorb green light. Specifically, the poly(AAm-co-AAc) hydrogels can be seen by eye to be more red than poly(NIPAAm-co-AAc) hydrogels, suggesting that they absorb more strongly in the green region of the spectrum. If these gels absorb more strongly, and if scattered light plays a role in beam interactions, then it would be expected that beam interactions would be stronger in the poly(NIPAAm-co-AAc) gel compared to the poly(AAm-co-AAc) gel. However, the opposite trend is observed (studied in detail in Chapter 3), which shows that scattered light cannot play a dominant role in long-range beam interactions.
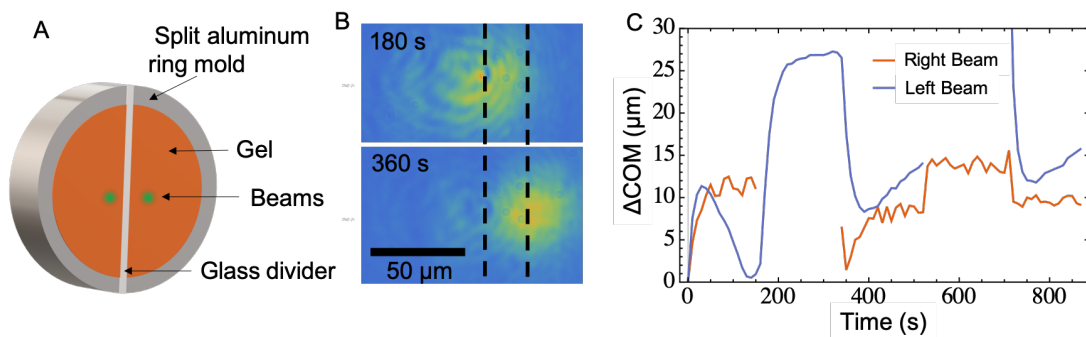
Figure 2.6: Interactions of two beams separated by a glass coverslip. **(A)** Diagram of the gel with a glass coverslip separator that completely bisects the gel, isolating each half with respect to chemical and pressure transport, but not to thermal transport. **(B)** Still images of the left beam showing the change in beam center in response to the right beam being switched off. **(C)** Change in the center of mass of each beam. Beams bend away from the other beam when the second beam is on, and then move towards the second beam location when that beam is off. While the right beam does respond, it does so at a much smaller magnitude due to a lower degree of self-trapping that occurred due to partial reflection off the glass divider. Reprinted with permission from *Chem. Mater.* 2020, 32, 24, 10594–10600[58]. Copyright 2020 American Chemical Society.

We experimentally confirmed the thermal interaction hypothesis by conducting two-beam experiments in which the beams were shone into a gel on either side of a ∼100 μm thick glass separator that completely bisects the gel (Figure 2.6). The glass barrier removes any chemical or poroelastic transport between the two sides of the gel such that any beam response must be a result of thermal effects. The results of this experiment show that parallel beams interact quickly and strongly even when separated by a glass barrier, proving that thermal effects dominate their interactions. In fact, these interactions are more significant than those of beams separated by the same distance without a glass separator (Figure 2.5), likely due to the higher thermal conductivity of the glass compared to the gel.

Estimation of the magnitude of thermally-driven long-range interactions is able to provide quantitative predictions that match the experimental data. Direct measurement of the local temperature changes is difficult due to the small area and the inaccessibility of the beam path within the bulk hydrogel sample. Instead we estimate the local temperature changes using analytical and numerical methods. We model the heat transport in cylindrical coordinates as diffusive with a heat source that

is dependent on the local intensity:

$$\frac{\partial u(r,z,t)}{\partial t} = \frac{k}{\rho c_P}\left(\frac{1}{r}\frac{\partial u(r,z,t)}{\partial r} + \frac{\partial^2 u(r,z,t)}{\partial r^2} + \frac{\partial^2 u(r,z,t)}{\partial z^2}\right) + \frac{2\alpha}{\rho c_P}I(r,z,t) \qquad (2.12)$$

Where $u(r,z,t)$ is the temperature as a function of radial distance from the beam, distance along the beam path, and time. k is the thermal conductivity, which was measured to be approximately 0.4 W m^{-1} K^{-1} for similar gels[61]; ρ is the density of water, 1000 kg m^{-3}; c_P is the heat capacity of water, 4,182 J kg^{-1} K^{-1}; and α is the absorption coefficient, which was previously estimated to be about 800 m^{-1} (Table 2.1). $I(r,z,t)$ is the intensity of the beam as a function of radial distance, distance along the beam path, and time. For the purpose of estimation we assume that the beam is fully self-trapped throughout the gel (its width does not change with z) and that it is constant in time. The beam's initial input intensity I_0 is determined by the beam power and the beam intensity decreases exponentially due to absorption, leading to the expression for the intensity:

$$I(r,z) = I_0 e^{\frac{-r^2}{w^2}} e^{-\alpha z} \qquad (2.13)$$

Where w is the constant beam width, which we assume is 20 μm, and outside of the appropriate z boundaries of the gel we assume that $I = 0$. On the front and back sides of the gel we model a 1 mm thick piece of glass, with a thermal conductivity of 1 W m^{-1} K^{-1}. Fixed temperature boundary conditions were used.

This problem was solved using Mathematica's built-in finite-element solving methods. The simulation results are shown in Figure 2.7. The maximum simulated temperature increase was found to be about 3.6 K.

Changes in temperature affect the propagation of light through the thermal swelling/deswelling of
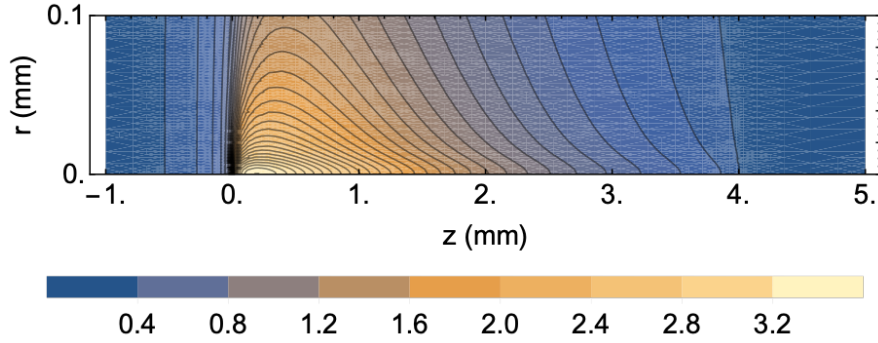
Figure 2.7: Finite Element Modeling results of the steady state temperature increase in degrees K due to a self-trapped 20 μm wide, 6 mW c.w. beam. The gel domain runs from $z = 0$ to $z = 4$ mm, with 1 mm of glass on both ends. Temperature difference is fixed to zero at the boundaries. The maximum temperature reached occurs at about $z = 0.2$ mm and corresponds to an increase of about 3.6 K. Reprinted with permission from *Chem. Mater.* 2020, 32, 24, 10594–10600[58]. Copyright 2020 American Chemical Society.

the hydrogel. The changes in swelling are related to the engineering strain e by

$$e = \left(\frac{V}{V_0}\right)^{1/3} - 1 \tag{2.14}$$

Using this we measure, near room temperature, an engineering strain of 0.43 %/K for poly(AAm-co-AAc) hydrogels near room temperature (Figure 3.2). In the linear approximation the volume fraction φ is related to the strain as $\varphi = \varphi_{eq}(1 - 3e)$. Thus the dimensionless change in the volume fraction of polymer $\psi = \frac{\varphi - \varphi_{eq}}{\varphi_{eq}} = -3e$, which is related to the refractive index by equation (2.9). The refractive index in terms of the engineering strain is thus $\Delta n = -3(n_p - n_s)\varphi_{eq}e$. Using $n_p = 1.49$, $n_s = 1.33$, and $\varphi_{eq} = 0.4$ we estimate a change with temperature of -0.0008/K for poly(AAm-co-AAc).

What matters for light propagation is not the absolute change in refractive index, but rather the local gradient. Thus, while the absolute change of around 4 K near the beam center is fairly large, the temperature difference one beam radius (10 μm) away from the beam center is only about 0.5 K. This leads to a local refractive index contrast that is smaller than but still comparable to the Δn due

to spiropyran isomerization, suggesting that temperature effects likely play some role in single beam self-trapping.

The situation is different for two beams. In this case the rotational symmetry is broken, so even a small temperature gradient seen across the beam as a result of the other beam can lead to measurable bending of the beam. The numerical model shown in Figure 2.7 suggests that at a distance about 200 μm away from the beam center the average temperature difference over 20 μm is about 0.025 K, corresponding in poly(AAm-co-AAc) to a refractive index difference of about 2×10^{-5}, or a gradient of about $1 \, \mathrm{m}^{-1}$. We can estimate the beam bending that would result from this by considering the ray tracing equation:

$$\frac{d}{ds}\left[n(\vec{r})\frac{d\vec{r}}{ds}\right] = \nabla n(\vec{r}) \tag{2.15}$$

Where $\vec{r}$ is the beam path, n is the spatially varying refractive index, and d/ds is the line derivative along the beam. We assume that the beam begins propagating directly along the x axis and that n varies only along the y direction. Noting that, if θ is the angle between the beam direction and the x axis, $\tan \theta = dy/dx$, then the equation becomes

$$\frac{d^2 r_y(x)}{dx^2} = \frac{n'(y)}{n(y)}(\tan^2 \theta(x) + 1) \tag{2.16}$$

Where $r_y(x)$ is the y position of the beam as a function of x. Given that the beam bends by a small amount over the distances considered, we can assume that $\tan^2 \theta(x) \ll 1$, which simplifies the problem to that of a particle under a constant acceleration of $n'(y)/n(y)$. The solution is thus $r_y(x) = \frac{n'(y)}{2n(y)}x^2$. As mentioned previously, at a distance of about 200 μm from the beam center, $n'(y) \approx 1 \, \mathrm{m}^{-1}$, and $n \approx 1.49$. For a propagation distance of 4 mm this gives an approximate deflection in the y direction of about 5.4 μm, which corresponds very well to the observed deflections shown in Figure 2.5. This shows that thermal effects drive the observed long-range interactions, and that

thermal effects likely play a role in single-beam self-trapping in poly(AAm-co-AAc) gels.

2.3   Conclusions and Outlook

In this chapter we have laid the foundation for understanding the physical processes that lead to beam self-trapping and beam interactions in spiropyran-functionalized hydrogels. We have identified that the processes of photoisomerization and gel swelling/deswelling are sufficient to explain single beam-self trapping dynamics, but that thermal transport and the gel's thermal response are required in order to explain relatively fast, long-range interactions between beams. Estimations of the magnitude of these thermal effects suggest that they may play an important role in single-beam dynamics as well, suggesting that they must be considered in a full model of the nonlinear optical dynamics of spiropyran-functionalized hydrogels.

This theoretical understanding is a necessary foundation for the design and optimization of spiropyran-functionalized gel systems for future applications. While SP gels have a unique combination of desirable properties, including reversibility, low power requirements, and long-range interactions, they also have a number of drawbacks compared to other nonlinear optical materials, such as a relatively slow response (∼minutes) and significant optical loss (∼95% over 4 mm).

Both of these factors appear to be significantly limited by the spiropyran isomerization dynamics. The poroelastic L^2/D timescale for a 10 μm radius spot in these gels is approximately 5 seconds, suggesting that the timescales of self-trapping and recovery are currently limited by the ring-closing and ring-opening isomerization rates. Many different spiropyran chemistries have been evaluated in an effort to optimize the photoisomerization and recovery rates[19, 17, 62, 63, 64], and these studies suggest that the use of optimized chromophores could significantly speed up the timescale of reversible self-trapping in spiropyran-functionalized gels.

Optical loss, on the other hand, can be optimized by designing a spiropyran-functionalized gel sys-

tem that exhibits a larger response to photoisomerization, and by choosing an excitation wavelength that best balances chromophore absorption and the rate of isomerization. For example, all of the experiments presented here use a 532 nm laser and acrylic acid based gels. The acidity of these gels results in most of the spiropyran being present in the protonated ring-open MCH^+ form, which has an absorption peak at about 430 nm[19, 10, 15, 65], far from the laser wavelength. It is the deprotonated MC form that has an absorption peak of 530 that is primarily excited by the laser. The relatively low concentration of MC means that absorption at this wavelength is low, but that can also potentially lead to slower photoisomerization and a less complete isomerization of MC and MCH^+ to SP. It is possible that an excitation wavelength closer to the MCH^+ peak could be optimized to find the best balance between photoisomerization and absorption.

Another approach would be to use a sacrificial guide beam, such as a 532 nm laser, that is largely absorbed, coupled with a signal beam at a wavelength that is not significantly absorbed. The signal beam would see the refractive index profile created by the guide beam and would thus still be shaped, but with minimal power loss[66].

A final approach to minimizing absorptive losses is simply to reduce the concentration of spiropyran moieties in the system. Measurement of the magnitude of the gel contraction in response to irradiation with 532 nm laser light (Figure 2.8) yields an effective χ_{sp} of about 600 kPa M^{-1}, which is an order magnitude larger than the value found by fitting the model of single-beam self-trapping to the experimental data. This discrepancy is likely explained by the swelling effect of the local temperature increase in the gels. This suggests that, in gels without this inhibitory temperature response such as poly(NIPAAm-co-AAc), the concentration of spiropyran could potentially be reduced by an order of magnitude or more, reducing absorption correspondingly.

Overall, applications will require the careful design and optimization of various aspects of the system in order to fit particular requirements. Much of this can be accomplished by changing the chemistry of the polymer backbone itself. The effects of the polymer backbone composition on self-
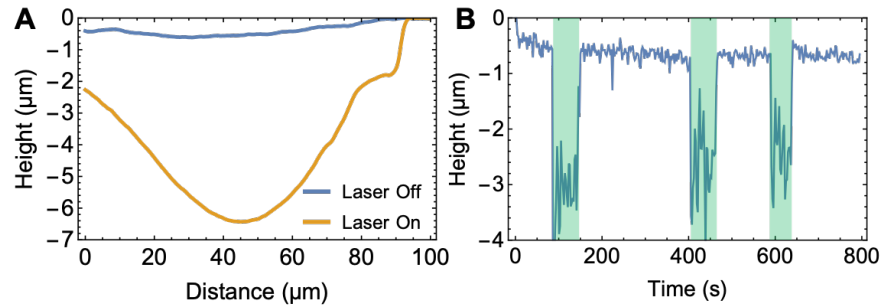
Figure 2.8: Direct AFM measurement of light-driven gel contraction. **(A)** AFM measurements of the change in the surface topology of a $\sim$340 μm thick spiropyran-functionalized poly(AAm-co-AAc) gel film before and after a 532 nm laser is switched on. The laser is switched on as the AFM probe is at about 95 μm during the retrace, leading to the fast contraction of the gel surface. The maximum decrease of the surface height is about 6 μm in this example, corresponding to an engineering strain of about -1.8%. The gel is thin and immersed in water, so local temperature changes due to absorption are expected to be minimal. **(B)** Change in the gel height at the center of the beam as the laser is switched on and off. Green regions indicate when the laser is on. Large variability in height while the laser is on corresponds to fluctuations in the laser power by several mW. Reprinted with permission from *Chem. Mater.* 2020, 32, 24, 10594–10600[58]. Copyright 2020 American Chemical Society.

trapping and beam interactions are demonstrated in the next chapter, while the effects of the polymer backbone on the spiropyran isomerizaton dynamics are explored in chapter 4.

3

Designable Responsivity of Spiropyran-Functionalized Hydrogels

IN THE PREVIOUS CHAPTER we showed how the swelling of a poly(AAm-co-AAc) gel with increasing temperature drives repulsive long-range interactions. Different gels compositions can lead to widely different swelling responses to changes in temperature, such as in N-isopropylacrylamide (NIPAAm)

based gels which contract with increasing temperatures and show lower critical solution temperature (LCST) behavior. This suggests the possibility that design of the gel composition could significantly affect the dynamics and interactions of self-trapped beams, paving the way for complex multi-beam applications that could be used for optical computing or machine learning.

This chapter will demonstrate how the effect of monomer choice on the gel's temperature response can be used to design nonlinear optical materials with tunable long-range beam interactions. We will then go further and show how the designable ability of gels to respond to external conditions such as temperature, pH, and electric fields, allows self-trapped beams to be externally controlled. Prior to these experimental demonstrations, however, we will first explore the underlying reasons for why spiropyran isomerization causes light-responsive swelling or contraction in hydrogels to begin with, and how changes to the polymer composition may affect this..

3.1   WHY ARE SPIROPYRAN-FUNCTIONALIZED HYDROGELS LIGHT-RESPONSIVE?

Spiropyrans and related chromophores are somewhat unique among light-responsive molecules in that they can undergo a significant change in both charge and hydrophilicity, and can function as a photoacid. In contrast, azobenzenes, another common light-responsive molecule, only undergo relatively small changes in polarity and conformation[67, 68]. These three aspects of the spiropyran photoisomerization (hydrophilicity, charge, and photoacidity) make spiropyrans an extremely versatile class of molecules, eliciting either swelling or contraction of a hydrogel upon illumination depending on a variety of factors such as environmental conditions, hydrogel composition, or whether or not the spiropyran molecule is attached to the polymer network.

This dependence, and hence the ways in which spiropyrans affect gel swelling, is well-illustrated by two similar experiments that produce very large and opposite results. Shi et al.[69] use a water-soluble, sulfonated spiropyran molecule to trigger the reversible contraction of a pH-sensitive poly(AAm-co-

37

AAc) hydrogel. Li et al.[62] use a similar water-soluble, sulfonated spiropyran molecule, but in their experiment it is polymerized into the backbone of a NIPAAm hydrogel immersed in an acidic solution. Upon irradiation these gels swell by close to 100%. From these two experiments we see that nearly the same spiropyran molecule can lead to completely opposite gel responses depending on the gel composition and whether or not the spiropyran is attached to the polymer backbone.

We interpret these results based on the Flory-Rehner theory of gel swelling[70] and the theory of swelling of weak polyelectrolytes[71]. In the Flory-Rehner theory the degree of swelling depends on the competition between the entropy loss of polymer chain stretching and the entropy gain of mixing between the polymer and the solvent. In the case of water as a solvent the hydrophilcity or hydrophobicity of the polymer is accounted for in the Flory-Huggins χ parameter, with more hydrophobicity leading to less swelling. Thus in the case of spiropyran attached to the polymer backbone we would expect the hydrophilic, charged, ring-open MC and MCH$^+$ isomers to lead to more swelling, and the hydrophobic, ring-closed SP isomer to lead to more contraction. However, this cannot explain the contraction of the gel observed by Shi et al.[69], as in their experiment the spiropyran is not attached to the hydrogel and thus its hydrophobicity should have no effect on χ. This also cannot explain the results of Li et al.[62], who observe a gel swelling upon the ring-closing isomerization of an attached spiropyran moiety.

These results are instead explained by changes in the osmotic pressure induced by counterions in weak polyelectrolyte gels. Polyelectrolyte gels contain charges directly on the polymer backbone. These charges must be locally balanced in order to maintain electroneutrality, and often they are balanced by the presence of mobile counterions in solution. The ability for mobile counterions to diffuse outside of the polyelectrolyte network combined with the requirements for electroneutrality inside and outside of the gel results in a difference in the concentration of mobile ions inside and outside of the gel. These concentration differences create an ideal gas pressure that swells the gel. Thus increasing the charge density of the polymer backbone leads to swelling, while decreasing the charge density

leads to contraction of the gel.

Gels are pH responsive if the polymer charge density depends on the pH, such as in the case of weakly acidic acrylic acid gels. This is the mechanism for gel contraction in the unattached, sulfonated spiropyran case[69]: MCH releases a proton when it is converted to SP^- upon irradiation, which lowers the pH and protonates some of the carboxylic acid moieties on the polymer backbone, lowering the charge density and thus the mobile counterion osmotic pressure, resulting in gel contraction.

The polymer charge density can also be changed when the spiropyran moiety is directly attached to the polymer backbone. Due to the negative charge on the sulfonate group the protonated ring open MCH form is zwitterionic and electrically neutral, while the ring-closed SP^- form is negatively charged. Thus isomerization of MCH to SP^- increases the mobile counterion pressure and causes the gel to swell[62].

While the polyelectrolyte effects are most important for explaining the results of Shi et al.[69] and Li et al.[62], our experiments with spiropyran-functionalized poly(AAm-co-AAc) hydrogels illustrate the strength and importance of the change in hydrophilicty that accompanies the ring-closing isomerization. In our case the positively-charged MCH^+ isomer lowers the charge density of the polymer backbone by balancing out some of the negatively-charged carboxylic acid groups. When the pH is lowered during the photoisomerization of MCH^+ to SP the charge density is actually increased, since the loss in positive charge is not fully compensated for by the protonation of some carboxylic acid moieties. This should lead to an increase in the counterion pressure, which should lead to gel swelling, in contrast to our observations of light-induced contraction. The driving force of contraction in this case must then be the increased hydrophobicity of the SP isomer compared to MCH^+.

While self-trapping only requires small changes in the gel swelling, on the order of a few percent or less, the magnitude of a gel's response to light can be greatly increased by coupling it to a lower critical solution temperature (LCST) or upper critical solution temperature (UCST) phase transition. In this case the relatively small change in hydrophobicity or counterion pressure can shift the critical

temperature above or below the environmental temperature, leading to a nonlinear change in the gel's swelling state. This is commonly done with NIPAAm based gels[72], but the versatility in the design of LCST or UCST gels means that it could be done with a wide variety of gel types with a wide variety of critical temperatures[73].

The combination of ways in which spiropyran photoisomerization and gel chemistry can affect the swelling state of the gel provides a huge design space for spiropyran-functionalized light-responsive hydrogels: they can be designed to swell or contract in response to light, the response can be small or large depending on environmental conditions like temperature or pH, and it can be done with spiropyran that is attached or diffusing.

Using these principles we propose a novel gel composition designed to lead to gel swelling in the presence of non-attached spiropyran. In order for non-attached spiropyran to affect the gel swelling it must be found predominantly in the protonated MCH form in the dark, which requires an environmental pH below the pK_a of MC. However, in order for isomerization to cause gel swelling the gel must have moieties that become charged upon protonation, and that are not already fully protonated at the dark pH, suggesting that they must have a pK_a below the environmental pH.

One promising gel moiety is the aniline moiety, which has a pK_a of about 4.6[74]. We developed a model that calculates the counterion pressure as a function of gel composition, spiropyran isomer concentrations, external ionic strength, and external pH, based on the model of Doi et al.[71] (See Appendix C for model details). As shown in Figure 3.1, this model predicts that a poly(2-(4-Aminophenyl)ethyl methacrylate) (poly(APEMA)) hydrogel containing unattached spiropyran would be expected to swell significantly upon irradiation under a wide range of external pHs, while acidic gels and basic gels with higher pK_as would not. Beyond being a novel light-responsive gel system, this combination of light-induced swelling and spiropyran diffusibility could be used to create gels that are able to form optical Turing patterns, which is explored in Chapter 5.
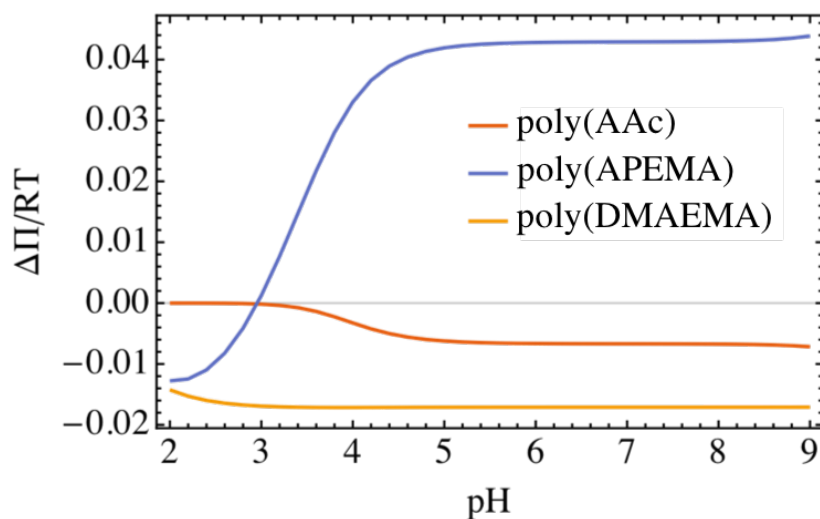
Figure 3.1: Model results of the change in mobile counterion osmotic pressure due to isomerization of unattached sulfonated spiropyran in different polyelectrolyte gels. A negative value of $\Delta\Pi$ indicates gel contraction upon light exposure, while a positive value indicates gel swelling. The model assumes a solution ionic strength of 20 mM with varying pH. Poly(AAc) and poly(2-dimethylaminoethyl methacrylate) (poly(DMAEMA)) gels always contract upon radiation, while poly(2-(4-Aminophenyl)ethyl methacrylate) (poly(APEMA)) can either swell or contract depending on the external solution pH. The radically different behaviors of polycations poly(APEMA) ($pK_a \approx 4.6$) and poly(DMAEMA) ($pK_a \approx 8.5$) shows the importance of having a gel monomer pK_a that is below the pK_a of MC ($pK_a \approx 6.5$).

.
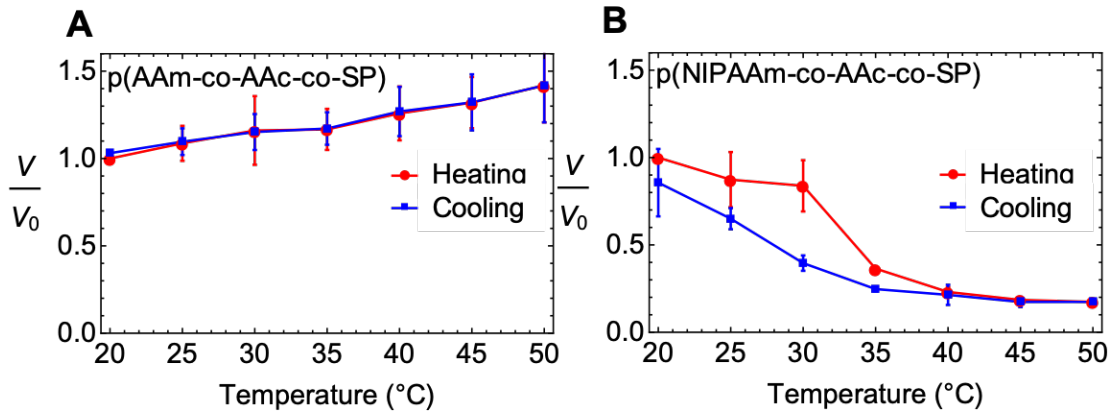
Figure 3.2: Temperature response of spiropyran-functionalized poly(AAm-co-AAc) and poly(NIPAAm-co-AAc) hydrogels. **(A)** Measurement of the swelling ratio of spiropyran-functionalized p(AAm-co-AAc) hydrogel disks as a function of temperature. V_0 is the initial volume at 20 $^\circ$C before heating. Error bars show standard error with N=3. **(B)** Measurement of the swelling ratio of spiropyran-functionalized p(NIPAAm-co-AAc) hydrogel disks as a function of temperature. V_0 is the initial volume at 20 $^\circ$C before heating. Error bars show standard error with N=2.

3.2 Designable Nonlinear Optics

Now that we understand the ways in which the polymer and the spiropyran work together to determine the gel's response to light, we can apply this to design and tune the nonlinear optical response. Given the importance of the gel's thermal response that we identified in the previous chapter, one of the simplest demonstrations of this designability is to use a NIPAAm based gel that contracts rather than swelling with increasing temperature (Figure 3.2).

Figure 3.3 demonstrates how spiropyran-functionalized poly(NIPAAm-co-AAc) show similar behaviors in terms of self-trapping to poly(AAm-co-AAc) gels, but at greatly different incident beam powers. While a 6 mW single beam in poly(AAm-co-AAc) gels self-traps down to ≈20 μm, a 6 μW in the same material undergoes significant defocusing, reaching a maximum beam width of about 220 μm (Figure 3.3A). We hypothesize that this self-defocusing may be due to a relatively weak strength of contraction due to very low levels of photoisomerization combined with still significant thermal swelling, but this needs to be confirmed through further experiments or modeling.

42
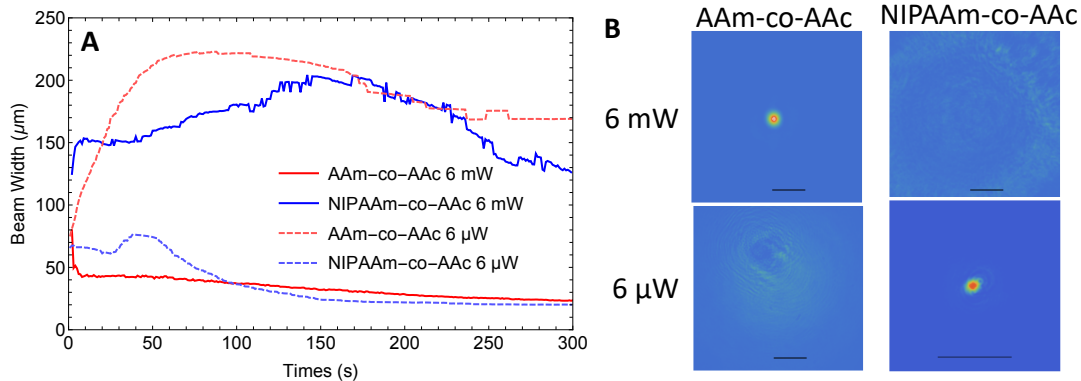
Figure 3.3: Comparison of single-beam self-trapping in spiropyran-functionalized poly(NIPAAm-co-AAc) and poly(AAm-co-AAc) gels. **(A)** Plots of beam width vs. time at high and low powers. We see that both AAm and NIPAAm based gels can undergo full self-trapping (beam width $\approx$20 μm) and self-defocusing (beam width >100 μm). **(B)** Images at $t = 300$ s for each type of gel and each power shown in (A). Scale bars correspond to a length of 100 μm.

In contrast to the AAm based gels, full self-trapping is observed for a 6 μW beam in poly(NIPAAm-co-AAc), while a 6 mW beam undergoes significant defocusing in the same gel, reaching a maximum width of about 200 μm (Figure 3.3). We hypothesize that this reversal in beam behavior with power may occur due to the reversal in thermal response of the gel: at lower laser powers there is no thermal inhibition and even relatively small amounts of spiropyran photoisomerization can lead to gel contraction and beam self-trapping, while at high powers there is a large amount of photoisomerization and thermal contraction over a large area, which leads to poor confinement of the beam. This simple experiment demonstrates the potential of the wide design space for interactions between the spiropyran isomerization and the gel's response, which can be used to program in a range of nonlinear optical responses, from self-focusing to self-defocusing, for a range of incident beam powers.

Long-range interactions between multiple beams can also be rationally designed by changing the gel composition. While spiropyran functionalized poly(AAm-co-AAc) gels showed repulsive long-range interactions due to thermal swelling, a poly(NIPAAm-co-AAc) gel would be expected to potentially demonstrate attractive interactions due to thermal contraction of the gel. However, it is important to note that replacing AAm monomers with NIPAAm monomers changes more than just the response

of the gel to temperature. It also has a significant effect on the equilibrium concentrations of spiropyran isomers, the mechanical response of the gel to isomerization, and on the isomerization kinetics (Chapter 4), all of which could affect interactions. However, none of these effects would lead to repulsive interactions, so we expect to observe attractive or minimal interactions. Results of an experiment involving two beams in poly(NIPAAm-co-AAc) hydrogel with a separation distance of 210 μm are shown in Figure 3.4A-B. Indeed, we observe minimal interaction between the beams, in contrast to the strong repulsive interactions seen in poly(AAm-co-AAc) hydrogels.

While we observe long-range thermal swelling leading to repulsion between beams, short separation distances where there is overlap in the optical field of the beams is expected to lead to attractive interactions, especially in cases where thermal effects are minimal. Attractive interactions between beams are of great interest, as they can lead to the emergence of particle-like behavior, such as beam spiraling[75] and merging[25]. Attractive interactions were not observed previously in the case of two 6 mW beams separated by 25 μm in spiropyran-functionalized p(AAm-co-AAc) hydrogels (Figure 2.4), likely due to the large thermal inhibition that results from doubling the incident beam power in a small area. However, as we show here, spiropyran-functionalized poly(NIPAAm-co-AAc) hydrogels do not have inhibitory thermal interactions, and are thus expected to display attractive interactions at short separations. Indeed, experiments with two beams separated by 25 μm in a poly(NIPAAm-co-AAc) gel exhibit both spiraling and merging (Figure 3.4C-D). At early times (red color), there is one peak located at (0 μm,0 μm). This peak quickly separates into two focused spots aligned with the vertical axis. Over time these peaks defocus and rotate counterclockwise around the original center peak. After a rotation of approximately 90°, at later times (blue color) the peaks merge into a single peak located at about (−6 μm,−2 μm), with a less clearly distinguished peak at about (0 μm,4 μm). The blurring of the beams and the lack of strong focusing in the final merged beam is likely due to the relatively slow MC protonation rate in the poly(NIPAAm-co-AAc) gels, which is on the order of hours (Chapter 4). This means that, in the several-minute long experiment, as the beams move they leave behind regions

of contracted gel that take hours to fully relax, leading to blurring and spreading of the incident light. This behavior is in stark contrast to the mutual inhibition that occurs for two beams separated by 25 μm in spiropyran-functionalized poly(AAm-co-AAc) hydrogels (Figure 2.4), showing the critical role that gel chemistry plays in beam behaviors.

3.3   External Beam Control

These results demonstrate how the polymer composition can be used to tune long-range interactions between beams, in essence building towards the idea of all-optical computation based on light-guiding-light[38]. However, gels can also be designed to respond to a wide variety of external stimuli, including temperature, pH, electric fields, and magnetic fields[76]. If these external stimuli are non-symmetrical then they can induce a swelling gradient across the hydrogel, resulting in a refractive index gradient that can lead to beam bending in much the same manner of that observed in spiropyran-functionalized poly(AAm-co-AAc) gels (Figure 2.5). This environmentally responsive beam bending could potentially be used for applications ranging from sensing to optical computing devices that are able to respond and interact with their environment.

We have demonstrated this concept with external thermal and electrical stimuli. To apply an external thermal gradient on a spiropyran-functionalized poly(NIPAAm-co-AAc) we placed the gel on a PDMS shelf in a water-filled cuvette with an electric resistance heater adhered to the bottom (Figure 3.5A). Turning the heating element on leads to reversible diagonal bending of over 30 μm after a delay related to the rate of thermal transport through the water and the distance between the gel and the heater. This bending is completely reversible, with beams returning close to their original location after the heater is turned off and with the same delay (Figure 3.5B). The observed change in the beam's center-of-mass was three times the 10 μm beam radius, indicating a large response to even a small non-symmetrical temperature change.

45
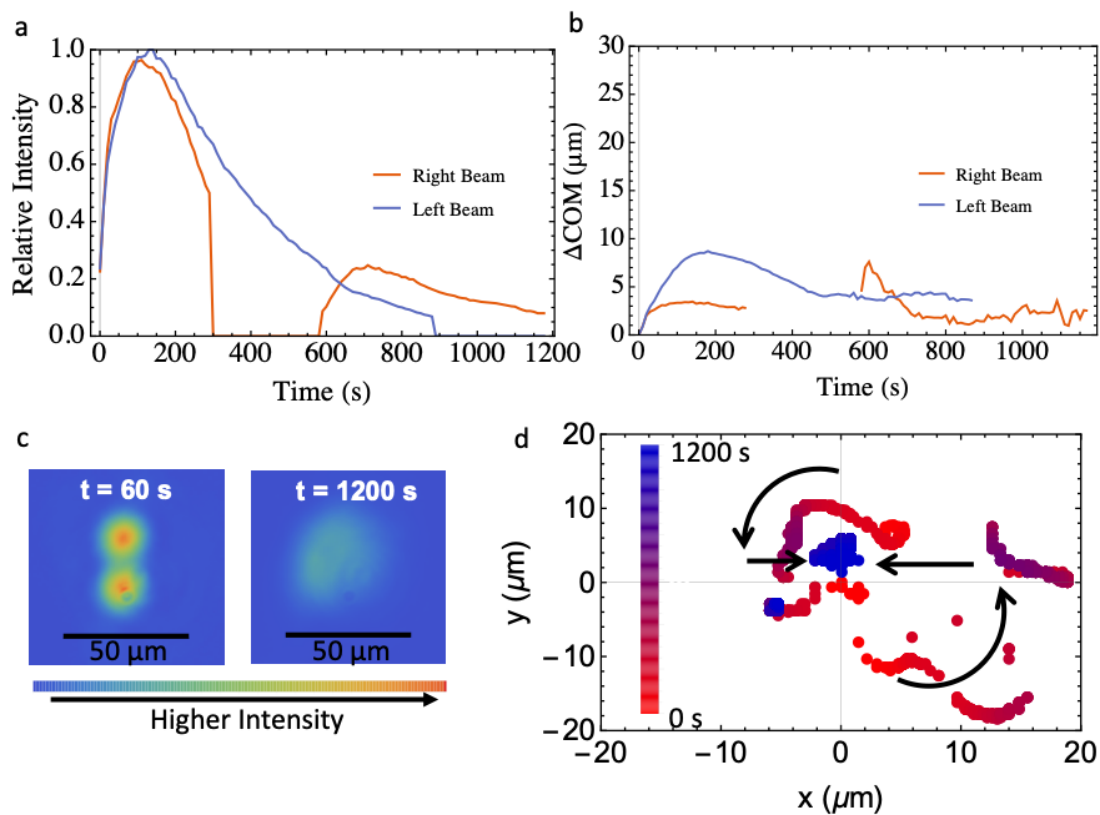
Figure 3.4: Two-beam experiments in a spiropyran-functionalized poly(NIPAAm-co-AAc) hydrogel. **(a)** Relative peak intensity of two beams separated by 210 μm. Peak intensity does not appear to respond to changes in the second beam. **(b)** Changes in the center of mass of each beam show no significant response to the other beam being switched on or off. **(c)** For beams separated by 25 μm, initial repulsion followed by attraction was observed. At $t = 60$ s the two beams are individually self-trapped, while at $t = 1200$ s the same two beams have merged. d) The dynamics of two close beams are shown by lowpass filtering the data and then tracking peak positions. Color indicates time through the experiment, with red indicating earlier times and blue indicating later times. Arrows added as guides.

Self-trapped beams in spiropyran-functionalized poly(AAm-co-AAc) gels were found to undergo large, reversible bending in response to applied voltages of 8 and 2 V. Graphite foil electrodes were placed above and on either side of a gel slab, with a separation distance of 8 mm, and immersed in a 10 mM solution of NaCl salt (Figure 3.6). Changes in the beam center-of-mass on the order of 20 to 30 μm were then observed when the voltage was applied (Figure 3.6B). Intriguingly, 8 V applied horizontally leads almost entirely to vertical bending, while 2 volts lead to a combination of primarily horizontal and some horizontal deflection. This may be attributed to two separate voltage-dependent effects: local changes in pH due to the hydrolysis of water, and the migration of mobile counterions due to the applied field[71]. A detailed analysis of the mechanisms and prediction of electrically-controlled beam bending in SP gels is a promising area for future study.

Thus we have shown that both thermal and electrical stimuli can lead to significant beam bending in both the direction of the applied stimulus and, surprisingly, orthogonal to that direction. This can potentially be used for environmental sensors, where the degree of beam bending acts as a readout, or all-optical logic and switching, where external control and guide beams to trigger different operations in a microfluidic or soft robotic system. Understanding what factors determine the direction and magnitude of the beam bending response will be an important part of realizing these potential applications.

3.4 Conclusions and Outlook

In this chapter we have elucidated the ways in which spiropyran isomerization and additional stimuli interact with the polymer chemistry to trigger the swelling or contraction that controls light within these materials. We demonstrate how the gel chemistry can be rationally designed to tune the nonlinear optical response of SP gels, such as in poly(NIPAAm-co-AAc) gels that show short-range attractive interactions and no long-range interactions, in contrast to poly(AAm-co-AAc) gels that show long-
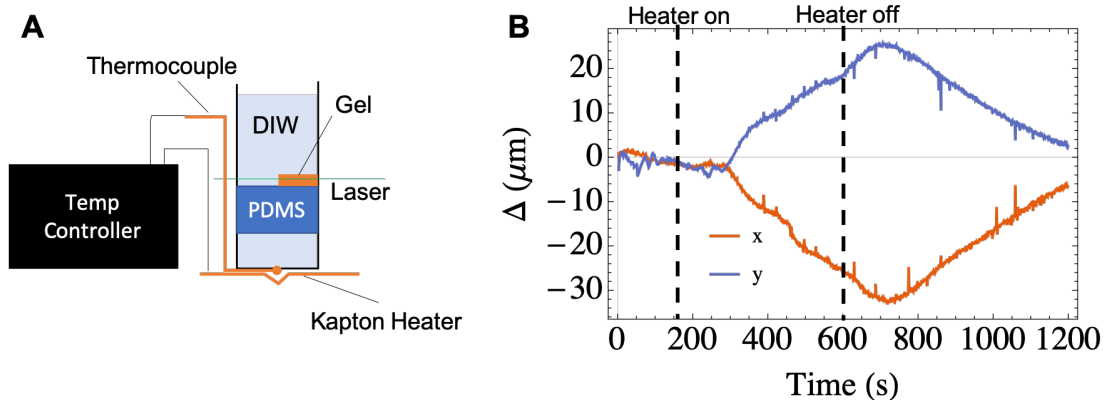
Figure 3.5: External thermal beam bending in spiropyran-functionalized 1:1 poly(NIPAAm-co-AAc) gels. **(A)** Diagram of the thermal beam bending experimental setup. Heating was done from below the sample to create a vertical temperature gradient across the gel. **(B)** A self-trapped beam responds to the heating being turned off and on by translating diagonally. The consistent delay between the heater being turned on or off and the beam response is related to the rate of thermal transport between the heater and the gel. Total reversible diagonal translation of over 30 μm was observed.
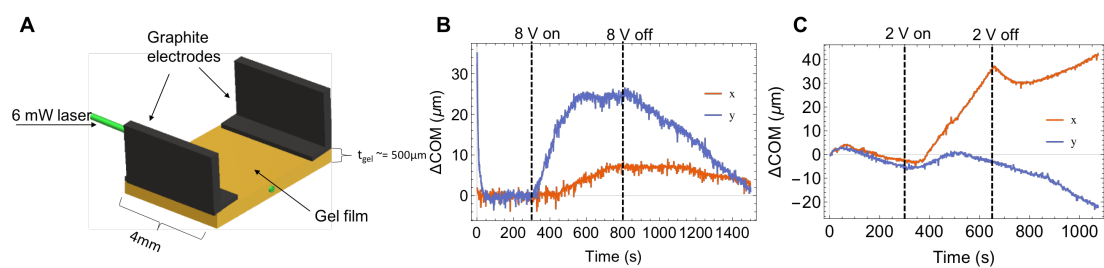
Figure 3.6: External electrical beam bending in spiropyran-functionalized poly(AAm-co-AAc) gels. **(A)** Diagram of the electrical beam bending experimental setup. **(B)** A self-trapped beam with an applied voltage of 8 V responds by translating vertically by about 25 μm, despite the field being applied horizontally. **(C)** Under 2 V a self-trapped beam bends about 40 μm horizontally when the voltage is on, and then diagonally when the voltage is turned off.

and short-range repulsion. Finally, we demonstrated how external environmental stimuli can be used to create a large beam-bending response. The details of these beam bending responses are not well understood and are an interesting area for future study.

While we have only shown thermal and electrical responses, gels can be made responsive to a wide variety of additional external stimuli, including magnetic fields[77], salts[8], and even biomolecules[78, 79]. This tremendous design space provides a huge opportunity for combined optical-chemical systems with active feedback, with potential for soft-robotics or combined optical and microfluidic systems. For example, an aptamer-functionalized hydrogel could be made responsive to a particular biomolecule of interest. While the swelling response of such gels is small compared to the collapsing phase transition of traditional responsive gels, it is more than enough to cause beam bending. Thus different biomolecular gradients could bend a beam into different waveguides, perhaps directing light onto light-responsive microfluidic valves that could then control flow to indicate the outcome of a diagnostic test or to provide nutrients to a particular group of cells.

Nonlinear self-trapping is important in applications like this because the magnitude of beam bending is proportional to the square of the path length. Thus longer path lengths lead to greater sensitivity, but under linear optical conditions it will also lead to significant beam spreading and lower peak intensity, which lowers sensitivity. This trade off is avoided in the case of the self-trapped beams demonstrated here, which maintain a consistent beam size through long path lengths while also being significantly responsive to external stimuli. Thus there is tremendous future potential for rationally designed gels that combine a gel response to light and to another specific stimuli of interest. The effect of changes to the polymer backbone needed to create additional stimuli-responsiveness on the spiropyran photoisomerization dynamics, and thus the nonlinear optical properties of the gel, is explored in the next chapter.

49

4

Photochemistry of Spiropyran-Functionalized Hydrogels

THE PREVIOUS CHAPTER HAS SHOWN how the chemistry of the gel backbone can be used to make SP gels responsive to a wide variety of different external stimuli, allowing for complex beam interactions and external control of beams. However, changes to the polymer backbone can also affect the
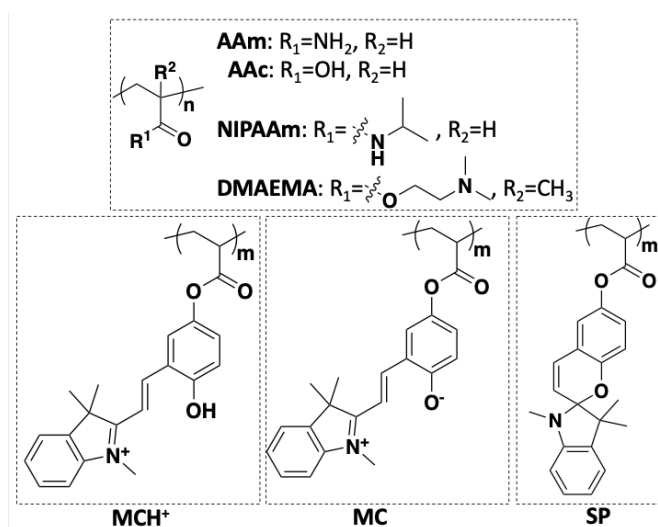
Figure 4.1: Schematic of the co-monomers (acrylamide (AAm), acrylic acid (AAc), N-isopropylacrylamide (NIPAAm), 2-(dimethylaminoethyl) methacrylate (DMAEMA)) and chromophore isomers (ring-closed spiropyran (SP), ring-open merocyanine (MC), protonated merocyanine (MCH+)) making up the hydrogels studied in this chapter.

isomerization dynamics of the spiropyran itself. The goal of this chapter is to better understand these interactions and to identify important principles for designing the overall SP gel system.

We approach this by probing the isomerization dynamics in a variety of responsive materials using fluorescence microscopy and UV-vis spectroscopy. We study four different commonly-used hydrogel materials: thermally responsive N-isopropylacrylamide (NIPAAm) gels, pH responsive acrylic acid (AAc) and 2-(dimethylamino) methacrylate (DMAEMA) gels, and nonresponsive acrylamide (AAm) gels (Figure 4.1). These gels differ significantly in terms of charge, acidity, and hydrophobicity, all of which could affect the spiropyran isomerization dynamics. While significant work has been done to understand the effects of modifications to the spiropyran moiety itself on its aqueous photochemistry[19, 17, 62, 63, 64] and the effects of incorporation into a dense polymer matrix[80], less work has been done to explore the effects that co-monomers in an aqueous hydrogel environment have on spiropyran dynamics[65, 81].

51
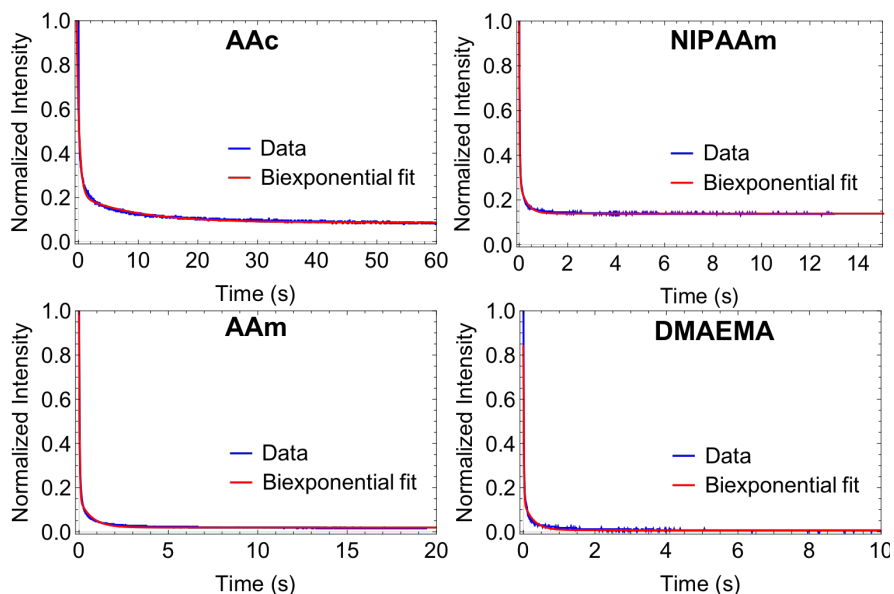
Figure 4.2: Fluorescence intensity dynamics under high-intensity 561 nm light are well-fit by a biexponential function for all gel compositions, suggesting minimal photoisomerization of aggregates upon irradiation with 561 nm light.

4.1 Experimental Results

Spiropyran-functionalized hydrogels were prepared by free radical UV polymerization of a 40wt% monomer (AAc, NIPAAm, AAm, or DMAEMA) and 0.49wt% acrylated spiropyran solution. We used excitation wavelengths of 561 nm and 405 nm in order to separately excite the MC ($\lambda_{max} \approx 530$ nm) and MCH$^+$ ($\lambda_{max} \approx 430$ nm) isomers. We observe that high-intensity ($\sim$mW) irradiation with 561 nm light leads to biexponential photoisomerization kinetics (Figure 4.2), which is the expected behavior for the MCH$^+$/MC/SP isomerization system considered in previous work. We also observe single exponential recovery in the dark (Figure 4.3), corresponding to the rate of ring-opening of SP to form MC.

In contrast, high-intensity 405 nm irradiation leads to unexpected triexponential, non-monotonic photoisomerization kinetics (Figure 4.4) and an unexpected increase in 405 nm and 561 nm fluorescence in the dark up to a month after high-intensity irradiation (Figure 4.5). Triexponential dynamics
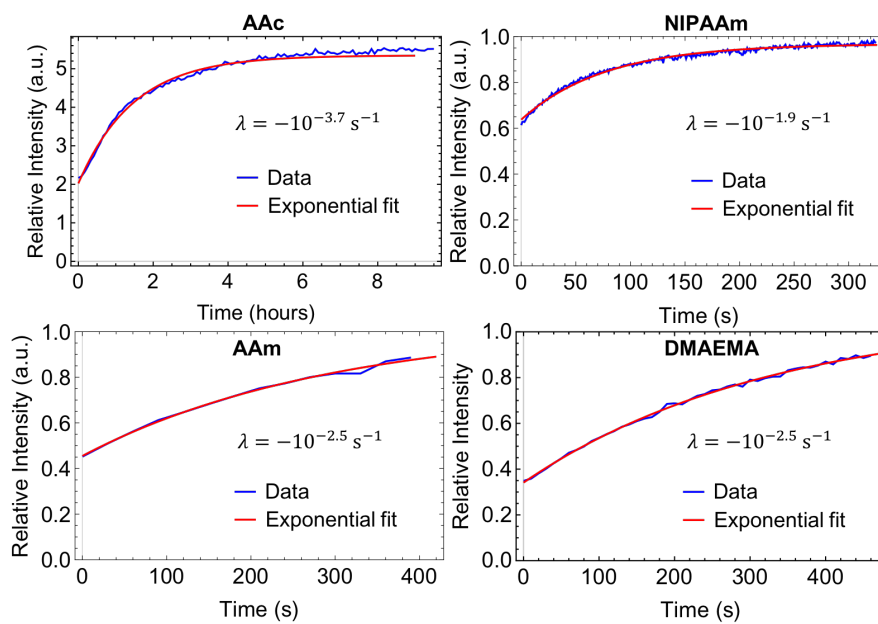
Figure 4.3: Short-term fluorescence recovery after high-intensity irradiation (AAc: 405 nm; NIPAAm, AAm, DMAEMA: 561 nm) in spiropyran-functionalized hydrogels. Solid red lines depict a single exponential fit to the experimental data, and the rate constant of each fit is shown.
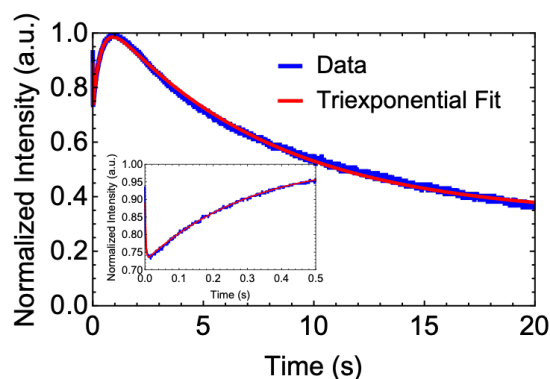
Figure 4.4: Fluorescence intensity data (blue line) of a spot under high-intensity 405 nm excitation in a poly(AAc-co-SP) hydrogel. Inset shows the first 0.5 s to highlight the initial drop and then increase of intensity. The intensity profile is non-monotonic and is well-fit by a triexponential function (red line). A mass-conserving system comprised of only linear isomerization reactions between SP, MC, and MCH$^+$ cannot lead to triexponential dynamics.

cannot be explained by a mass-conserving system comprised of only linear isomerization reactions between SP, MC, and MCH$^+$, while the long-term fluorescence increases are not commensurate with the relatively fast observed rate of fluorescence recovery due to the spontaneous ring-opening of SP (Figure 4.3). Taken together, these results strongly suggest that an additional spiropyran-based species exists in the spiropyran-functionalized gel system, and that it undergoes reactions predominantly at longer timescales or under intense 405 nm irradiation. This is a significant departure from prior work on spiropyran-functionalized hydrogels, which only consider isomerization reactions involving SP, MC, and MCH$^+$[10, 14, 15, 18, 16, 62, 19, 22, 82, 17].

We hypothesize that this fourth species consists of H-aggregated merocyanine stacks (H-MC) which disaggregate upon exposure to intense 405 nm light and which slowly reform at long timescales (Figure 4.6). Merocyanine dyes of all types are consistently observed to form H-aggregates, where the zwitterionic dyes align their dipoles by stacking with opposite alignment, and J-aggregates, where positively and negatively charged ends are joined such that all molecules have the same alignment[10]. In particular, H-aggregates have been identified in spiropyran pendant group homopolymers based on the observation of an absorption peak blue-shifted from the main MC peak that shows slower kinetics un-
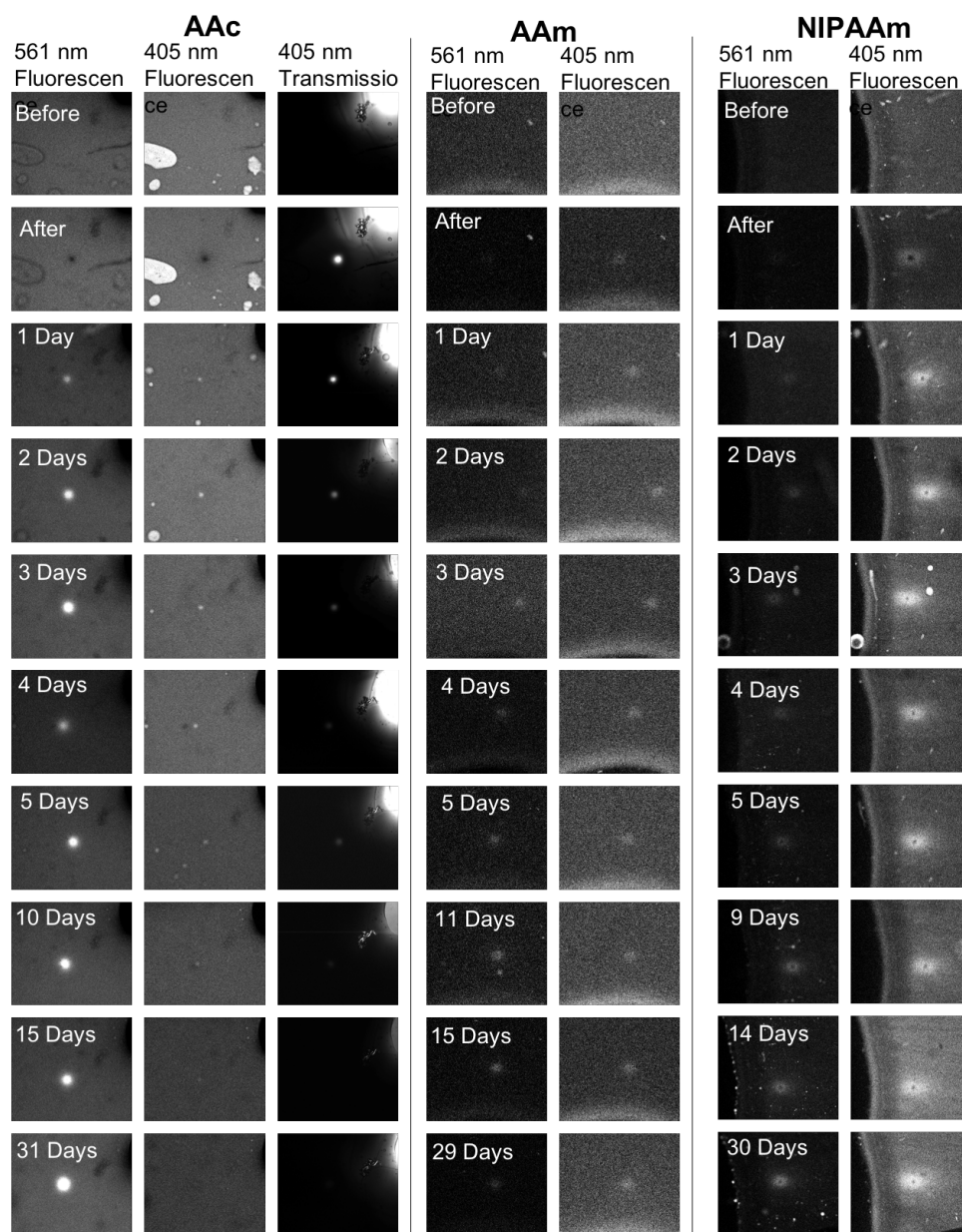
Figure 4.5: Long term fluorescence and transmission of a spot after irradiation with focused, high-intensity 405 nm laser light. Contrast and brightness of images were adjusted for visual clarity using Mathematica's built-in ImageAdjust function. Fluorescence of the irradiated spot is depressed immediately after high-intensity irradiation, but in all cases it increases in the days and weeks after irradiation. Data for poly(AAc-co-SP) gels show a strong increase in 405 nm transmission immediately following irradiation, possibly due to the reduction in MCH$^+$ and aggregates that absorb at 405 nm. This increased transmission decays over time along with the increased 405 nm fluorescence, while 561 nm fluorescence continues to increase, which we hypothesize corresponds to the formation of relatively small H-aggregates.
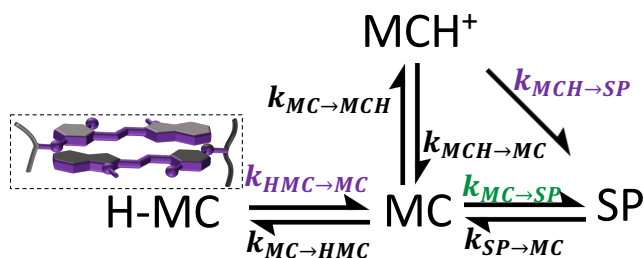
Figure 4.6: The reaction scheme including H-aggregated MC (H-MC) that we propose to explain the observed triexponential and long-term dynamics. The labels for rate constants used in this work are written next to the corresponding arrow, and violet-colored rate constants ($k_{MCH \to SP}$ and $k_{HMC \to MC}$) indicate a dependence on 405 nm light intensity, while green rate constants ($k_{MC \to SP}$) indicate a dependence on 561 nm light intensity. Inset shows a schematic representation of H-aggregated MC attached to a polymer backbone.

der visible light irradiation than the MC peak[83, 84]. These polymers have also been directly observed to crystallize into a zipper-like structure in which long stacks of H-aggregated merocyanines bind together two separate polymer backbones[85]. Light-responsive merocyanine H-aggregates have also been identified in poly(DMAEMA-co-SP) hydrogels[65], but have not been observed in more acidic gel environments.

We find further evidence for the existence of H-MC in the UV-vis spectra of aged spiropyran-functionalized polymers. Figure 4.7A shows UV-vis spectra for linear poly(AAm-co-AAc-co-SP) dissolved in solutions buffered between pH 3.0 and pH 8.5. These spectra were taken between zero and two hours after adding buffers to the respective polymer solutions. We observe peaks at 530 and 370 nm under neutral to basic conditions, which we ascribe to the MC isomer. An absorption peak at 430 nm arises as the pH becomes more acidic, identifying this peak as corresponding to the MCH$^+$ isomer. These identifications align well with the previous literature[19, 10, 15, 65].

Figure 4.7B shows UV-vis spectra of the same solutions five days later. We observe that in the solutions at pH 6 or higher the peaks at 430 and 530 nm disappear, being replaced instead with peaks at around 370 and 470 nm. We hypothesize that the peak at 470 nm represents a blue-shifting of the 530 nm MC peak due to the formation of H-aggregates[65, 83, 84], while the 370 peak could correspond

to a non-polar MC isomer[65], possibly suggesting the presence of microphase separation, or to the *cis*-MCH$^+$ isomer[86].

The aggregation hypothesis is further supported by considering the UV-vis spectra of spiropyran-functionalized poly(AAm-co-DMAEMA-co-SP) gels where the spiropyran moieties are either singly tethered as a pendant group (Figure 4.7C) or doubly tethered as a crosslinker (Figure 4.7D). DMAEMA-based gels are strongly basic even at relatively low external solution pH, and correspondingly the only observed absorption peak in the singly-tethered case is located around the proposed H-MC peak at 470 nm, with some shifting towards 430 nm as the external pH is lowered. In the doubly-tethered case, however, we recover the peaks corresponding to MC and MCH$^+$, and there is no evidence of a peak at 470 nm. This is expected if the 470 nm peak corresponds to an aggregated form of MC that is bound to the polymer backbone, as the doubly-tethered spiropyran would not be expected to be able to form aggregates due to the steric constraints on both ends of the chromophore.

4.2   Analytical Model of Isomerization Dynamics

Based on this evidence we propose the spiropyran isomerization scheme shown in Figure 4.6. We can use this scheme to develop an analytical model for the spiropyran dynamics that will explain the non-monotonic, triexponential dynamics under high-intensity 405 nm light. The isomerizaton network can be described by a system of three coupled, linear ODEs:

$$
\begin{aligned}
\frac{d\,[\mathrm{MC}]}{dt} = & -\left(k_{MC\rightarrow MCH}\left[\mathrm{H}^+\right] + k_{MC\rightarrow SP}\right)[\mathrm{MC}] + k_{MCH\rightarrow MC}\left[\mathrm{MCH}^+\right] \\
& + k_{HMC\rightarrow MC}\left[\mathrm{HMC}\right] + k_{SP\rightarrow MC}\left(\mathrm{SP}_{\mathrm{tot}} - [\mathrm{MC}] - \left[\mathrm{MCH}^+\right] - [\mathrm{HMC}]\right)
\end{aligned} \quad (4.1)
$$
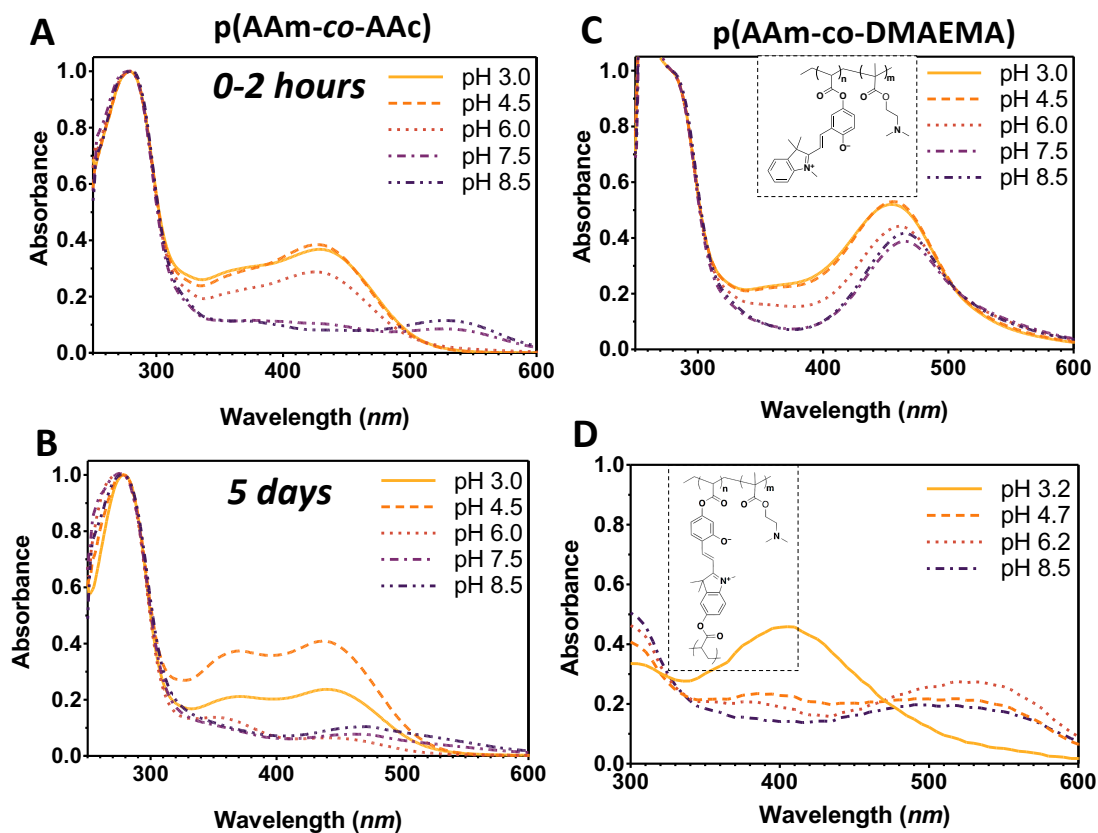
Figure 4.7: UV-vis Evidence of H-aggregated MC in spiropyran-functionalized hydrogels. **(A)** UV-vis spectra of linear spiropyran-functionalized poly(AAm-co-AAc) polymers dissolved in buffered solutions with pH ranging from 3 to 8.5. Spectra were taken between zero and two hours after adding buffer solutions to the polymer stock solution. We assign peaks at 530 and 370 to MC, while we assign the peak at 430 nm to MCH^+. **(B)** UV-vis spectra of the same solutions shown in (A) taken five days later. The 530 nm peak originally observed under neutral to basic conditions is now observed to blue-shift to about 470 nm, which we assign to H-aggregated MC. **(C)** UV-vis spectra of linear poly(AAm-co-DMAEMA) polymers with singly-tethered spiropyran (inset) dissolved in buffered solutions of pH ranging from 3 to 8.5. The three peaks observed in poly(AAm-co-AAc-co-SP) polymers are replaced by a single peak at about $460 - 470$ nm, even under acidic conditions. **(D)** UV-vis spectra of poly(AAm-co-DMAEMA) polymers with doubly-tethered spiropyran (inset) dissolved in buffered solutions of pH ranging from 3 to 8.5. The single peak of singly-tethered DMAEMA gels is replaced by peaks at 370, 430, and 530 nm. We propose that this is due to the tethering constraints inhibiting the aggregation of MC. Note that the observed 279 nm peak in all spectra is an artifact of leftover photoinitiator and does not correspond to a spiropyran isomer.

$$\frac{d\left[\text{MCH}^+\right]}{dt} = k_{MC \to MCH}\left[\text{H}^+\right]\left[\text{MC}\right] - (k_{MCH \to MC} + k_{MCH \to SP})\left[\text{MCH}^+\right] \tag{4.2}$$

$$\frac{d\left[\text{HMC}\right]}{dt} = -k_{HMC \to MC}\left[\text{HMC}\right] \tag{4.3}$$

Where [MC] is the concentration of unprotonated ring-open merocyanine, $\left[\text{MCH}^+\right]$ is the concentration of protonated ring-open merocyanine, [HMC] is the concentration of merocyanine that is contained within H-aggregates, and $\left[\text{H}^+\right]$ is the concentration of hydronium ions in the gel environment. $k_{X \to Y}$ is the rate constant corresponding to the reaction going from X to Y. Since the total number of spiropyran molecules SP_{tot} is conserved, the concentration of ring-closed spiropyran is replaced by $\left(\text{SP}_{\text{tot}} - \left[\text{MC}\right] - \left[\text{MCH}^+\right] - \left[\text{HMC}\right]\right)$. This system of equations can be written

$$\frac{d}{dt}\vec{x}\left(t\right) = \vec{x}\left(t\right)\widehat{W} \tag{4.4}$$

Where $\vec{x}\left(t\right) = \{\left[\text{MC}\right], \left[\text{MCH}^+\right], \left[\text{HMC}\right]\}$ is the vector of concentrations while $\widehat{W}$ is the rate-matrix

$$\widehat{W} = \begin{pmatrix} -\left(k_{MC \to MCH}\left[H^+\right] + k_{MC \to SP} + k_{SP \to MC}\right) & k_{MCH \to MC} - k_{SP \to MC} & k_{HMC \to MC} - k_{SP \to MC} \\ k_{MC \to MCH}\left[\text{H}^+\right] & -\left(k_{MCH \to MC} + k_{MCH \to SP}\right) & 0 \\ 0 & 0 & -k_{HMC \to MC} \end{pmatrix} \tag{4.5}$$

The solution to this system of equations has the form

$$\vec{x}\left(t\right) = \vec{x}_{\text{eq}} + A_1\vec{c}_1 e^{\lambda_1 t} + A_2\vec{c}_2 e^{\lambda_2 t} + A_3\vec{c}_3 e^{\lambda_3 t} \tag{4.6}$$

Where λ_i and $\vec{c}_i$ are the ith eigenvalue and eigenvector of $\widehat{W}$, $\vec{x}_{\text{eq}}$ is the equilibrium solution found
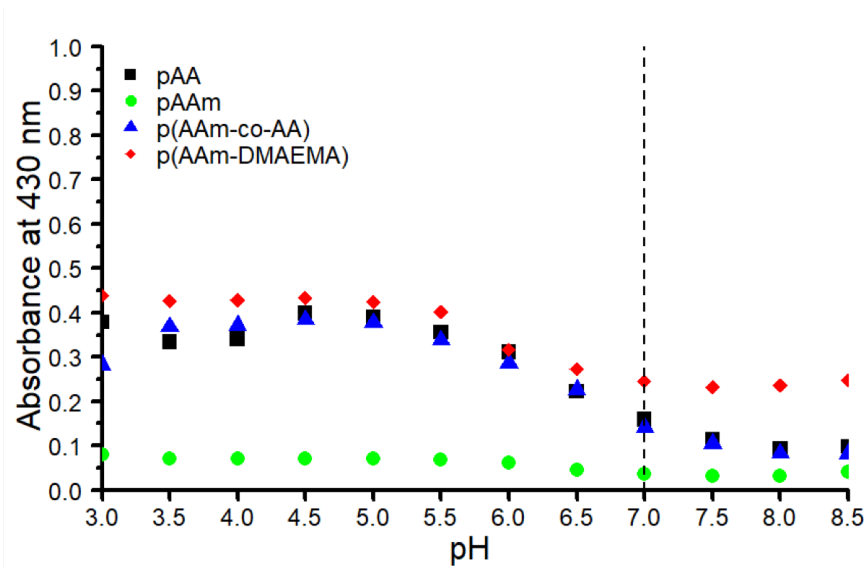
Figure 4.8: Absorbance at 430 nm measured in solutions of linear polymers with attached SP as a function of buffered solution pH. From this we estimate by eye a pK_a of about 7 for MC.

by setting equations (4.1), (4.2), and (4.3) equal to zero, and A_1, A_2, A_3, are constants determined by the initial conditions. Initial conditions were set by having $[HMC]_{init}$ as an adjustable parameter, setting $k_{MCH \rightarrow SP} = 0$ in the dark, and having the dark value of $k_{MC \rightarrow SP}$ as a separate fitting parameter.

In order to fit this analytical solution to the fluorescence intensity observations we assume that the fluorescence intensity is linearly proportional to $[MCH^+]$ with a fitted proportionality constant s. In addition, the initial fluorescence intensity observed is consistently far lower than expected, possibly due to a combination of system delay in the confocal microscope between the laser being turned on and the beginning of data collection and self-quenching of the spiropyran fluorescence[87]. We account for this by not fitting the magnitude of the initial exponential, A_1 from equation (4.6). The six parameters used to fit the data are thus:

$$\vec{\xi}_{analytical} = \{sA_2c_{MCH^+,2}, sA_3c_{MCH^+,3}, \lambda_1, \lambda_2, \lambda_3, sx_{MCH^+,eq}\} \tag{4.7}$$

The ten parameters of the dynamic model are $[H^+]$, s, $[\text{HMC}]_{\text{init}}$, $k_{MC \to MCH}$, $k_{MCH \to MC}$, $k_{HMC \to MC}$, $k_{MCH \to SP}$, $k_{MC \to SP}$, $k_{MC \to SP,dark}$, and $k_{SP \to MC}$. The protonation and deprotonation reaction rates are related by the estimated pK_a of 7 (Figure 4.8). Consideration of the dependence of the eigenvalues on each parameter (Table 4.2) suggested that the fastest eigenvalue in all cases is completely determined by the rate of MCH$^+$ photoisomerization, while the slowest eigenvalues of DMAEMA and AAc and the middle eigenvalue of NIPAAm and AAm are determined solely by the rate of disaggregation. Thus these reaction rates were set to the corresponding timescale of the triexponential fit. Finally, the rate of spontaneous ring-opening was set to our previously measured values (Figure 4.3). This leaves six independent parameters that were used for fitting:

$$\vec{p} = \left\{ \left[H^+ \right], s, \left[\text{HMC} \right]_{\text{init}}, k_{MC \to MCH}, k_{MC \to SP}, k_{MC \to SP,dark} \right\} \tag{4.8}$$

In order to fit the analytical model parameters we first use Mathematica's built-in FindFit function to find a triexponential fit to the first 12 (AAc) or 24 (AAm, NIPAAm, DMAEMA) seconds of the normalized fluorescence intensity data for each hydrogel material. These fits have six parameters $\vec{\xi}_{\text{fit}}$ corresponding to $\vec{\xi}_{\text{analytical}}$ of the analytical solution, ignoring the prefactor to the fastest exponential. Analytical model parameter fit were then acquired by minimizing the difference between these parameters and the equivalent expressions from the analytical model using the error function:

$$E\left(\vec{p}\right) = \sum_j \left(\frac{\vec{\xi}_{\text{fit}_j} - \vec{\xi}_{\text{analytical}_j}}{\vec{\xi}_{\text{fit}_j}} \right)^2 \tag{4.9}$$

A best fit was found by choosing 500 points randomly from a large potential range of values for each parameter, and then using Mathematica's built-in FindMinimum function to find the local minimum subject to physically relevant constraints (e.g. $0 \leq [\text{HMC}]_{init} \leq 1$). The resulting best fit parameters (lowest value of $E\left(\vec{p}\right)$ found from all 500 starting points) for each gel are shown in Table 4.1, and the

	AAc	NIPAAm	DMAEMA
$k_{MCH \to SP}$ (s^{-1})	$10^{2.691}$	$10^{1.492}$	$10^{1.299}$
$k_{MC \to MCH}$ $(s^{-1}\,M^{-1})$	$10^{3.563}$	$10^{5.386}$	$10^{6.504}$
$k_{HMC \to MC}$ (s^{-1})	$10^{-0.773}$	$10^{-0.245}$	$10^{-0.886}$
$k_{SP \to MC}$ (s^{-1})	$10^{-3.7}$	$10^{-1.9}$	$10^{-1.501}$
$k_{MC \to SP}$ (s^{-1})	$<10^{-1.5}$	$10^{-1.570}$	$10^{0.294}$
$k_{MC \to SP,dark}$ (s^{-1})	$<10^{-1.5}$	$<10^{-3}$	$10^{-0.690}$
pH	3.184	7.147	>7.5
$[HMC]_{init}/SP_{tot}$	0.21%	28.81%	34.98%
s	7.464×10^7	$123,600$	5.755×10^8

Table 4.1: Full results of parameter fitting of the analytical model to the high-intensity 405 nm fluorescence data. It was observed that the values of some parameters had a negligible effect on the resulting fit so long as they were above or below some threshold. These are shown in with a less than or greater than sign.

resulting fits are shown in Figure 4.9A-C. Separate parameters are not provided for AAm gels because the initial fast increase in intensity is not commensurate with the model, while the slower dynamics match very closely with the dynamics of NIPAAm gels, suggesting that the relevant parameters are very similar between the two gels. It is unclear what causes the anomalous initial fluorescence increase in AAm gels, although one significant difference between AAm gels and the other gels tested here is that the AAm gels are opaque after polymerization, suggesting a large amount of microscopic phase separation. It's possible that irradiation could affect the opacity or microphase separation in a way that increases fluorescence. It is also possible for strong self-quenching to lead to an increase in fluorescence in response to a decreasing concentration of fluorophore.

The mechanism behind each part of the triexponential dynamics can be illuminated by considering the elasticity of the eigenvalues with respect to each parameter, $p_i d\lambda_i / \lambda_i dp_j$, evaluated at the best fit parameter values (Table 4.2). From this we see that in all cases the fasted eigenvalue, λ_1, represents the rate of light-driven isomerization of MCH^+ to SP. For each gel there is always a timescale determined solely by the rate of H-MC disaggregation, and in AAc and DMAEMA this is found the be
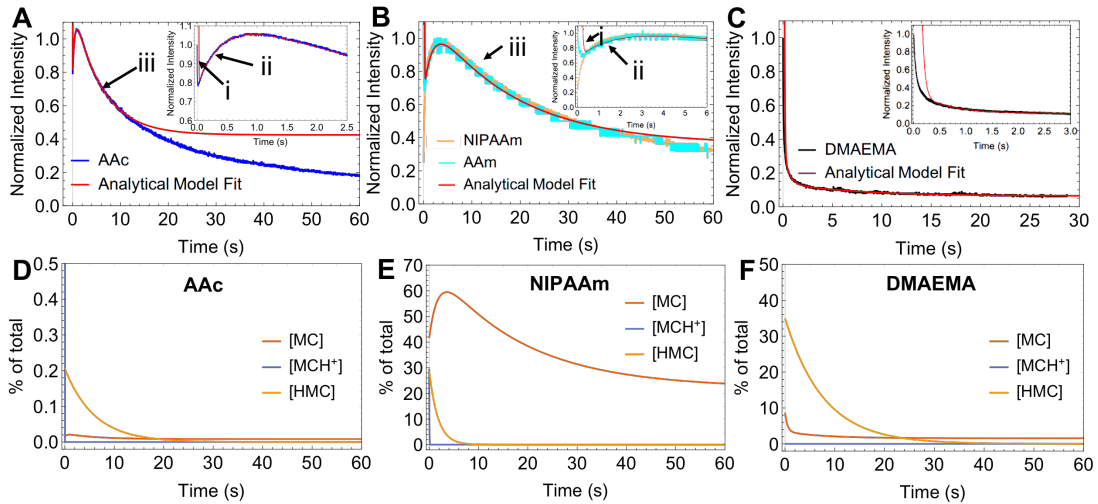
Figure 4.9: Example fits of 405 nm fluorescence observations from an analytical model incorporating aggregation and disaggregation. **(A)** Analytical model fit to poly(AAc-co-SP) data. Fluorescence intensity is normalized to the maximum value of the peak. Inset shows a magnification of the first 0.5 seconds. **(B)** Analytical model fit to poly(NIPAAm-co-SP) data with poly(AAm-co-SP) data also shown. Fluorescence intensity is normalized to the maximum value of the peak. Inset shows a magnification of the first 6 seconds. **(C)** Analytical model fit to poly(DMAEMA-co-SP) data. Fluorescence intensity is normalized to the maximum value in the data. Inset shows a magnification of the first 3 seconds. **(D)** Model results of the MC, MCH^+, and HMC concentration as a percentage of the total chromophore over time in the poly(AAc-co-SP) gel. The graph focuses on the dynamics of small amount of MC and H-MC, while nearly 100% of initial chromophore is in the MCH^+ isomer. **(F)** Model results of the MC, MCH^+, and HMC concentration as a percentage of the total chromophore over time in the poly(NIPAAm-co-SP) gel. While the MCH^+ concentration drops nearly to zero very quickly, the MC concentration increases by nearly 50% before decreasing over the course of several minutes. **(G)** Model results of the MC, MCH^+, and H-MC concentrations as a percentage of the total chromophore over time in the poly(DMAEMA-co-SP) gel. The MCH^+ concentration is near zero due to the strongly basic internal gel environment. All model results use the parameters shown in Table 4.1.

the slowest timescale, λ_3, while in NIPAAm gels disaggregation is the middle eigenvalue, λ_2. The third timescale of each gel is related to the equilibration of MC through either protonation (AAc), ring-closing (DMAEMA), or a mix of both processes (NIPAAm).

In the AAc, AAm, and NIPAAm gels we observe a further and even slower decrease in the fluorescence at times greater than 30-60 seconds that deviates from the triexponential model. We do not believe that this corresponds to a photodegradation process, as no long-term decrease in fluorescence is observed even after long periods of intense irradiation (Figure 4.3). We instead hypothesize that ag-

	AAc			NIPAAm			DMAEMA		
	λ_1	λ_2	λ_3	λ_1	λ_2	λ_3	λ_1	λ_2	λ_3
$\lambda\,(s^{-1})$	-485	-2.4	-0.17	-30	-0.57	-0.057	-20	-2.0	-0.13
$k_{MCH \to SP}$	1	0	0	1	0	0	1	0	0
$k_{HMC \to MC}$	0	0	1	0	1	0	0	0	1
$k_{SP \to MC}$	0	0	0	0	0	0.22	0	0	0
$k_{MC \to SP}$	0	0	0	0	0	0.47	0	1	0
$k_{MC \to MCH}$	0	1	0	0	0	0.30	0	0	0
$[H^+]$	0	1	0	0	0	0.30	0	0	0

Table 4.2: Eigenvalues and their elasticity with respect to each parameter evaluated at the best fit values shown in Table 4.1. Note that parameters that do not have any effect on the rate constants (e.g. $[HMC]_{init}$) are neglected, and values below 10^{-1} were set to zero for clarity.

gregates may exist in a spectrum of sizes and configurations, and that this spectrum may have a wide variety of disaggregation rates. This hypothesis has been suggested in the literature to explain similar observations[80], but is not reflected in our current model.

This model can then be used to calculate the concentrations of all species as a function of time during irradiation. The modeled concentrations of MC, MCH^+ and H-MC in AAc, NIPAAm, and DMAEMA gels are shown in Figure 4.9D-F. In AAc and NIPAAm based gels we see that $[MCH^+]$ drops down to essentially zero very quickly, reflecting the extremely fast light-driven isomerization of MCH^+ to SP. The concentration of H-MC also decreases monotonically, although at slower rate. In contrast, [MC] increases by almost 50% in both gels before slowly decreasing towards the photostationary state. In AAc gels this increase in [MC] is insignificant due to the lower overall amount of chromophore found in the MC isomer, but in less acidic gels like NIPAAm this effect is much more substantial. This has important implications for the photoresponsiveness of these gels, as the MC isomer is also highly hydrophilic, so an increase in [MC] may actually cause swelling, or will at least counteract some of the contraction caused by the conversion of MCH^+ to SP, leading to an overall slower and lower magnitude response than in a more acidic gel with fewer aggregates. This may be an

important part of why spiropyran-functionalized NIPAAm gels are found to have a larger and more repeatable response to irradiation when a small amount of acrylic acid is also included[15].

We propose that aggregation dynamics can also explain the long-term fluorescence recovery dynamics observed after 405 nm excitation (Figure 4.5). Immediately after excitation there is depletion of both MC and MCH$^+$ relative to the background, leading to relatively lower fluorescence from both 405 nm and 561 nm excitation. However, recovery of equilibrium between SP, MC, and MCH$^+$ occurs on the timescale of minutes, leaving the formation of H-MC to be the only unequilibrated process at longer timescales. It has been hypothesized that aggregation is a continuous process, starting with smaller aggregates that form more quickly and are only slightly blue-shifted relative to the MC peak[80]. These smaller aggregates may fluoresce under 561 nm light, which is closer to their less-shifted absorption peak, leading to the slowly increasing intensity of the irradiated spot in poly(AAc-co-SP) under 561 nm excitation. The irreversibility of this process after one month suggests that after light-driven disaggregation the system is not able to reform the large initial aggregates. We hypothesize that these initial aggregates are possibly formed prior to polymerization, and so they may not be recoverable either due to the loss of unpolymerized spiropyran that was incorporated into the aggregate, or due to thermodynamic barriers to the spontaneous formation of such aggregates by polymerized spiropyran. Instead, our observations suggest the slow formation of smaller aggregates involving fewer MC molecules. This may also explain the reddening of bulk SP gels that occurs over several weeks post polymerization (Figure 4.10).

4.3 Conclusions and Outlook

We have used confocal fluorescence microscopy to directly observe the isomerization dynamics of spiropyran moieties in a variety of responsive polymer gel networks. The observed unusual non-monotonic, triexponential fluorescence data cannot be explained by the MCH$^+$/MC/SP isomeriza-
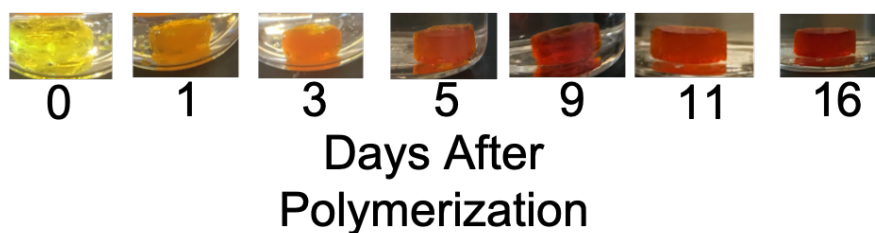
Figure 4.10: Images of 10 mm wide 4 mm tall cylindrical spiropyran-functionalized poly(AAm-co-AAc) gels taken over two weeks after photopolymerization. Immediately after polymerization gels are bright yellow. Over the course of two weeks they become orange and then red, possibly reflecting a gradual transformation of large, blue-absorbing aggregates into smaller green-absorbing aggregates.

tion scheme considered previously in the literature. This suggests the existence of H-aggregated MC, which was further confirmed with UV-vis spectroscopy of dissolved polymers. By incorporating H-MC into a model of spiropyran isomerization, we were able to fit the observed fluorescence dynamics and to attribute each timescale to different isomerization processes. We found that there is an initial fast conversion of MCH^+ to SP, followed by slower conversion of H-MC and MC to SP. This model provides insight into the ways that co-polymerized moieties affect the spiropyran isomerization kinetics, a topic that has received relatively little attention in the literature compared to direct modification of the spiropyran moiety.

These results have important implications for the design and optimization of light-responsive hydrogels for small length scales, where the timescale of poroelastic diffusion may be small. For example, at the micron scale of microfluidics[19, 20, 18, 21, 22], porous hydrogels[16], or self-trapped beams (Chapter 2), the timescale of poroelastic diffusivity can be seconds or less. In these cases the tens to hundreds of seconds we observe to be required for complete photoisomerization even under high-intensity focused laser light become limiting to the full photoresponse. Furthermore, fast, complete reversibility is often highly desirable, in contrast to the slow rate of aggregation we observe.

Based on this we conclude that pH and aggregation are important factors to consider when designing a multi-responsive spiropyran-functionalized hydrogel system. The importance of an acidic envi-

ronment in achieving a large, reversible photoresponse has been demonstrated previously[15], and by revealing the underlying reaction network we elucidate precisely how an acidic environment creates a large equilibrium concentration of MCH^+ and also aids in a faster conversion of all merocyanine species into SP upon visible light irradiation.

Aggregation has not been previously suggested as an important factor in the photoactuation of spiropyran-functionalized hydrogels. While aggregation adds further complexity and responsivity to spiropyran-functionalized gel systems, it also may be undesirable due to significantly slower kinetics. Thus, if aggregation is undesirable then modified spiropyran moieties that do not aggregate should be used, such as doubly-acrylated spiropyran crosslinkers, or spiropyrans with modified linkages that sterically impede aggregation. These design considerations are broadly important for the use of multi-responsive spiropyran-functionalized hydrogels for applications in a wide variety of fields, including microfluidics[19, 20, 18, 21, 22], soft robotics[23, 17], drug delivery[24], and nonlinear optics[14, 58].

5

Spontaneous Pattern Formation in

Light-Responsive Gels

THE PREVIOUS THREE CHAPTERS have laid out a comprehensive foundation for the design of SP gels as nonlinear optical materials. We have shown the relevant physical processes that lead to nonlinear optical phenomena, and how rational design of the polymer and spiropyran chemistry can be used

to add or modify different aspects of the gel's response. In this chapter we will show, as an example of what can be done using the foundational knowledge of SP gels laid out in this thesis, that a properly designed SP gel system has the potential to lead to the spontaneous formation of optical Turing patterns.

Spontaneous pattern formation is ubiquitous in nonlinear optical systems, usually taking the form of spatial modulation instability and corresponding beam filamentation[88, 89, 57]. In a typical spatial modulation instability experiment a broad beam is shone on a nonlinear optical material. Small variations in the local light intensity causes some regions to increase refractive index more than surrounding regions, causing more light to focus in those areas, further reinforcing the local increase in refractive index. This process causes the relatively uniform initial beam to spontaneously break up into a disordered array of focused spots. These spots will be randomly distributed with a characteristic length scale that depends on the strength of the nonlinearity and the intensity of the light[88, 89], although external symmetry breaking can lead to very regular patterns[45, 47]. This phenomenon has been used to create materials that can do basic computation through the interaction of beams undergoing modulation instability[46].

Turing patterns[90], in contrast, are extremely rare in optical systems[43]. Turing patterns arise when local nonlinear activation, such as what occurs in modulation instability, is combined with long-range inhibition. This can lead to a wide variety of different patterns, from spots to stripes to targets[91, 92], with well-defined characteristic length scales. Turing patterns have been suggested to play a role in many patterns and morphogenic processes in nature[93, 94, 95, 96, 97, 98] and have been shown to arise in a number of chemical reaction-diffusion systems where a difference in the diffusivity between an activator species and an inhibitor species can be created[99, 100, 101, 91, 102, 103].

Spiropyran-functionalized hydrogels are a promising system for the rational design and control of optical Turing patterns, which could be used to create reconfigurable, bottom-up photomasks for large-scale surface patterning. The local isomerization of tethered spiropyran moieties already leads to

local activation and, as we show below, modulation instability. However, unlike most other nonlinear optical systems, SP gels combine reversibility with the potential for diffusive, long-range interactions between beams. We will show that this has the potential to generate Turing patterns using relatively simple, known chemistries.

5.1 Modulation Instability in SP Gels

We will start by considering the linear stability analysis of broad beams in spiropyran-functionalized hydrogels, following the work of Bespalov and Talanov[88]. We consider the nonlinear paraxial wave equation without absorption and with an intensity dependent Δn:

$$0 = \nabla_\perp^2 A - 2ik\frac{\partial A}{\partial z} + 2k^2\frac{\Delta n(|A|^2)}{n_0}A \tag{5.1}$$

Where A is the complex field amplitude, k is the free space wavenumber, $n_0 = n(|A_0|^2)$ is the background refractive index, and $\Delta n(|A|^2) = n(|A|^2) - n_0$ is the local refractive index change. We can see immediately that $A = A_0$ is a steady-state solution. We apply a small perturbation to the solution, $(A_0 + a(x, y, z))$, where $a = a_1 + ia_2$ such that a_1 and a_2 are real and $|a| \ll A_0$. This gives us

$$0 = \nabla_\perp^2 a - 2ik\frac{\partial a}{\partial z} + 2k^2\frac{\Delta n(|A_0 + a|^2)}{n_0}(A_0 + a) \tag{5.2}$$

Focusing first on Δn we can approximate to first order in a:

$$\Delta n(|A_0 + a|^2) = n(|A_0 + a|^2) - n(|A_0|^2)$$

$$\approx n(A_0^2 + 2A_0 a_1) - n(A_0^2) \approx n(A_0^2) + \left.\frac{dn}{d|A|^2}\right|_{A=A_0} 2A_0 a_1 - n(A_0^2)$$

$$= 2\alpha A_0 a_1 \quad (5.3)$$

Where we have chosen A_0 to be entirely real, and defined α as the change in index as a function of intensity evaluated at A_0. Using this in equation (5.2) and approximating to first order in a we end up with

$$0 = \nabla_\perp^2 a - 2ik\frac{\partial a}{\partial z} + \frac{4k^2\alpha A_0^2}{n_0}a_1 \tag{5.4}$$

We can split this equation into real and imaginary parts:

$$0 = \nabla_\perp^2 a_1 + 2k\frac{\partial a_2}{\partial z} + \frac{4k^2\alpha A_0^2}{n_0}a_1 \tag{5.5}$$

$$0 = \nabla_\perp^2 a_2 - 2k\frac{\partial a_1}{\partial z} \tag{5.6}$$

and define the periodic spatial perturbation $a_{1,2} = Re[a_{1,2}^0 e^{-i\vec{k}_\perp \cdot \vec{r}_\perp - ihz}]$ where $k_\perp$ is the perturbation's wavenumber in the tangential directions, and h is the corresponding wavenumber in the direction of propagation. This results in the equations

$$0 = -k_\perp^2 a_1^0 - 2kha_2^0 + \frac{4k^2\alpha A_0^2}{n_0}a_1^0 \tag{5.7}$$

$$0 = -k_\perp^2 a_2^0 + 2kha_1^0 \tag{5.8}$$

71

We can define $a_r^0 = a_1^0/a_2^0$ and divide both equations by a_2^0 to get:

$$0 = -k_\perp^2 a_r^0 - 2kh + \frac{4k^2\alpha A_0^2}{n_0}a_r^0 \tag{5.9}$$

$$0 = -k_\perp^2 + 2kha_r^0 \tag{5.10}$$

We find the dispersion relation by solving these equations for h^2:

$$h^2 = \frac{k_\perp^2}{4k^2}(k_\perp^2 - \frac{4k^2\alpha A_0^2}{n_0}) \tag{5.11}$$

If we assume a nondimensionalized Kerr refractive index then $\Delta n = |A|^2 n_0/2$ and $\alpha = n_0/2$. If we also nondimensionalize such that $k = 1$ then this simplifies to

$$h^2 = \frac{k_\perp^2}{4}(k_\perp^2 - 2A_0^2) \tag{5.12}$$

Which is what was found by Bespalov and Telanov[88]. We can rearrange equation (5.11) slightly and define $k_{lim}^2 = 4k^2\alpha A_0^2/n_0$:

$$h^2 = \frac{k_\perp^2}{4k^2}(k_\perp^2 - \frac{4k^2\alpha A_0^2}{n_0}) = \frac{k_\perp^2}{4k^2}(k_\perp^2 - k_{lim}^2) \tag{5.13}$$

In the case of our gels we showed in Chapter 2 that

$$\Delta n = (n_p - n_s)\varphi_{eq}\psi \tag{5.14}$$

Where n_p and n_s are the refractive indices of the polymer and solvent phases respective, φ_{eq} is the equilibrium volume fraction, and $\psi = (\varphi - \varphi_{eq})/\varphi_{eq}$ is the normalized change in polymer volume fraction. At the steady state this is related to the spiropyran isomerzation by

$$\psi = \kappa C \tag{5.15}$$

$$C = \frac{k_f |A|^2}{k_b + k_f |A|^2} \tag{5.16}$$

$$\kappa = \frac{\chi_{sp} f_0 \varphi_{eq}^2}{\lambda + 2\mu} \tag{5.17}$$

Where $k_f |A|^2$ is the intensity dependent ring-closing isomerization rate and k_b is the intensity-independent ring-opening isomerization rate. λ and μ are Lamé's first and second coefficients respectively. f_0 is the monomer fraction of isomerizable spiropyran and χ_{sp} is the effect of isomerization on gel contraction. Overall this gives us

$$\delta n(|A|^2) = (n_p - n_s) \varphi_{eq} \kappa \frac{K_r |A|^2}{1 + K_r |A|^2} \tag{5.18}$$

Where $K_r = k_f / k_b$. This gives us

$$\Delta n'(|A|^2) = \alpha = \frac{K_r (n_p - n_s) \varphi_{eq} \kappa}{(1 + K_r |A|^2)^2} \tag{5.19}$$

The $k_\perp$ with the largest growth rate occurs at a minimum of h^2:

$$\frac{dh^2}{dk_\perp^2} = \frac{2k_\perp^2 - k_{lim}^2}{4k} = 0 \tag{5.20}$$

$$k_{\perp,max} = \frac{1}{\sqrt{2}} k_{lim} \tag{5.21}$$

A plot of $k_{\perp,max}$ for the parameter values shown in Table 2.1 is shown in Figure 5.1.
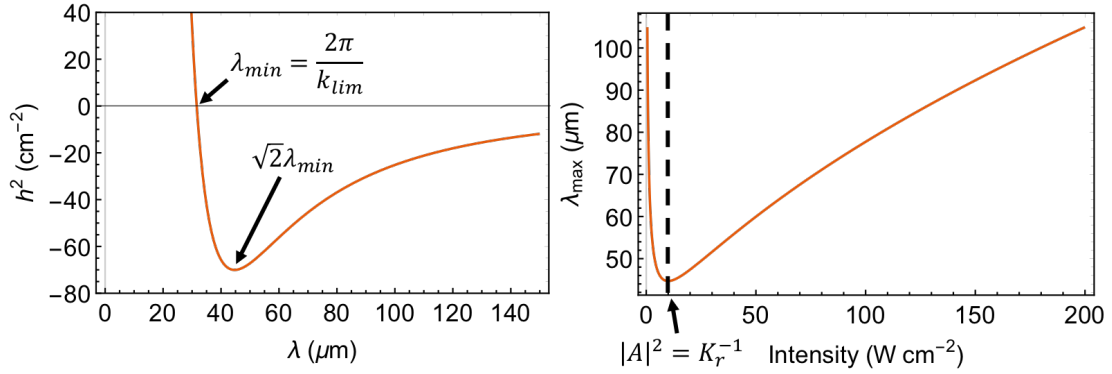
Figure 5.1: Analytical linear stability analysis showing modulation instability in SP gels. **(A)** Plot of h^2 vs. $\lambda = 2\pi/k_\perp$ using the dispersion relation (Equation (5.13)) and the parameters from Table 2.1. Negative values of h^2 result in modes that grow exponentially. **(B)** Plot of most unstable wavelength λ_{max} as a function of input light intensity $|A_0|^2$. The strongest modulation instability and correspondingly the smallest characteristic length scale occurs at intensities on the order of 10^5 W m^{-2}, much lower than those used in self-trapping experiments in poly(AAm-co-AAc) gels.

The maximum growth rate as a function of intensity occurs when

$$\frac{dk_{\perp,max}}{dA_0^2} = 0 \tag{5.22}$$

Which we find occurs when

$$A_0^2 = K_r^{-1} \tag{5.23}$$

Using the parameters in Table 2.1 $K_r \approx 10^{-5}$ m^2 W^{-1}. This corresponds to an intensity A_0^2 that is about two orders of magnitude lower than the intensities used for self-trapping experiments. At this value the most unstable wavelength is about 45 μm.

These calculations so far have neglected the effects of absorption. However, if the rate of wavenumber growth is less than the rate of decay due to absorption then modulation instability will be suppressed. This can be shown using numerical calculations, as shown in Figure 5.2.

We have experimentally observed modulation instability in spiropyran functionalized poly(NIPAAm-
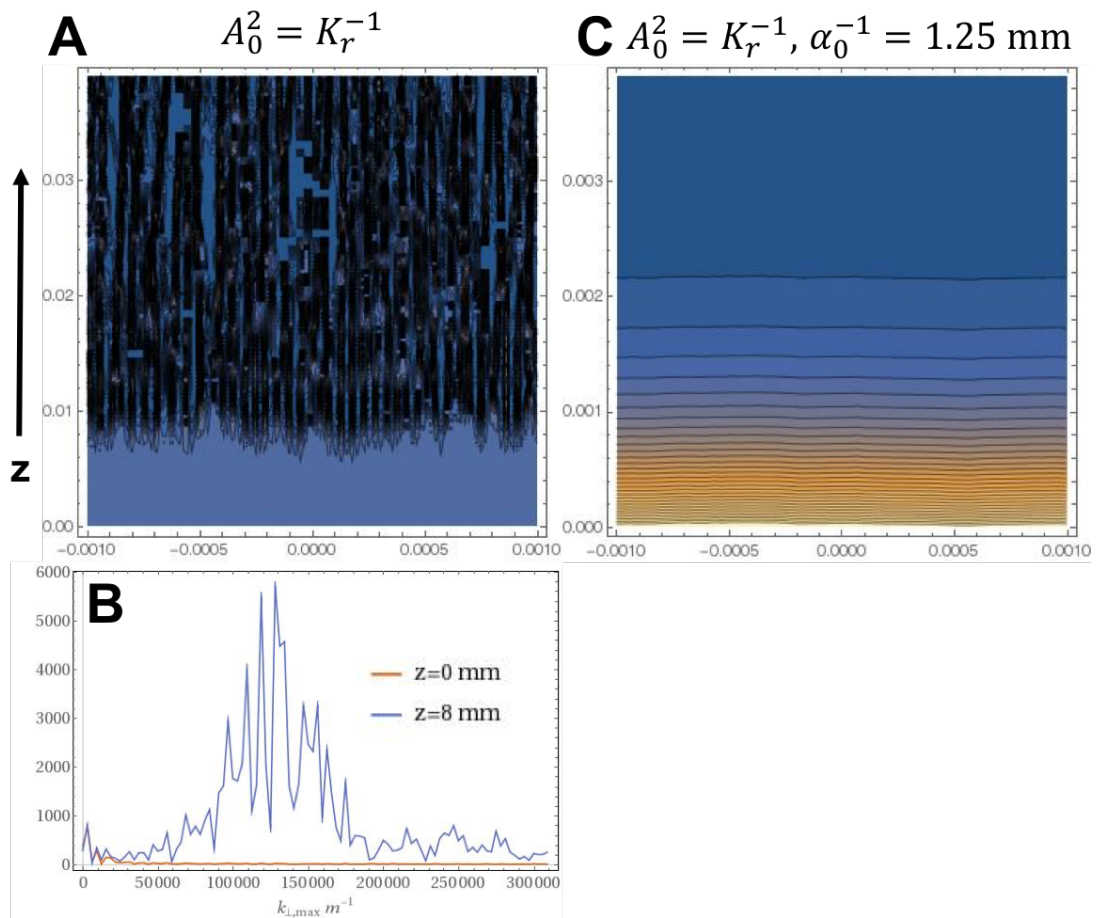
Figure 5.2: Numerical calculations of modulation instability in SP gels and the effect of absorption. **(A)** Numerical 2D solution of Equation (5.1) using the parameters from Table 2.1 and $|A_0|^2 = K_r$. Modulation instability is clearly seen to arise over the 4 cm simulation length. **(B)** Fourier power spectrum in the perpendicular direction at $z = 0$ mm and $z = 8$ mm. The wavenumbers with the largest growth rate occur between 100,000 and 150,000 m^{-1}, in agreement with the analytical calculations (Figure 5.1). **(C)** The same numerical calculation but with an absorption coefficient of 800 m^{-1}. This amount of absorption, similar to what was experimentally observed in our spiropyran-functionalized poly(AAm-co-AAc) hydrogels, effectively eliminates the modulation instability.

co-AAc) hydrogels, and the observed characteristic wavelength matches well with the estimate derived above from the linear stability analysis (Figure 5.3). The linear stability analysis assumes that the spiropyran isomerization and gel swelling are always at their steady-state solutions, which is unlikely to be the case in experiments where we see the modulation instability arising and changing over time.

The linear stability analysis also neglects absorption, which is significant in experiments and likely leads to further differences between the two.
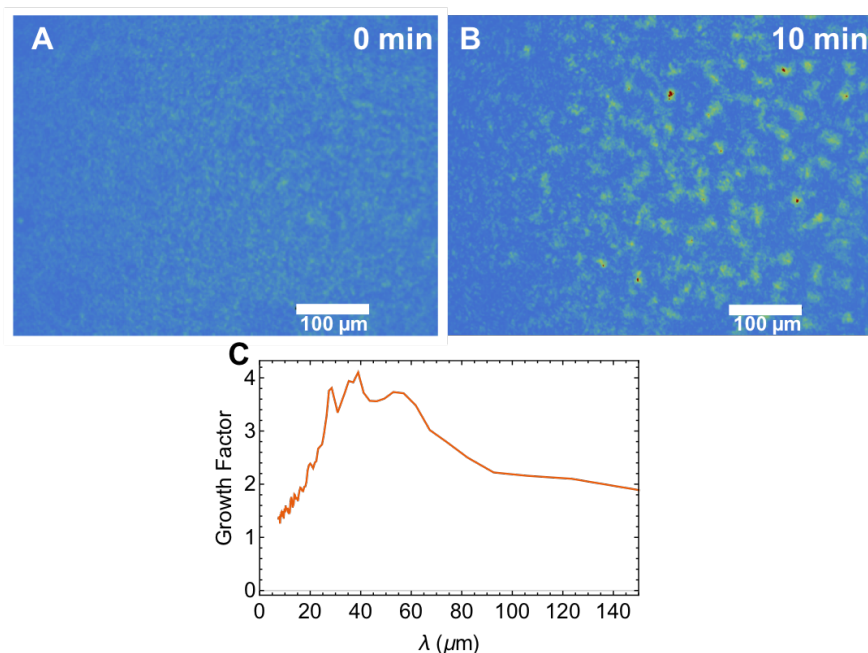
Figure 5.3: Experimental observation of modulation instability in a spiropyran-functionalized poly(NIPAAm-co-AAc) hydrogel. **(A)** Initial intensity on the exit face of the gel irradiated with a 600 μW, 1 mm wide beam of 561 nm laser light. A random speckled pattern arises from scattering within the gel. **(B)** The same experiment 10 minutes later. Modulation instability leads to the formation of a random array of bright spots with a characteristic size of about 30–60 μm. **(C)** Growth of spectral components was found by dividing the radial average spectral power of each 2D Fourier component at 10 minutes by the corresponding spectral power at 20 s. A clear peak is seen in the range of 30–60 μm, which matches well with the theoretical region of instability shown in Figure 5.1A.

5.2   A Theory of Turing Patterns in SP Gels

We develop a theory of Turing pattern formation in SP gels by adding a diffusing inhibitor to the linear stability analysis shown in Section 5.1. The combination of local activation and diffusing inhibition could be accomplished using both tethered and untethered spiropyran in an aniline-functionalized poly(2-(4-Aminophenyl)ethyl methacrylate) (poly(APEMA)) based gel, as considered in Section 3.1.

The light-induced change in hydrophobicity of tethered moieties will cause the gel to locally contract, while the pH change due to the isomerization of untethered MCH will cause swelling that is able to diffuse away from areas of local high-intensity light. We can model this by considering the steady state equation for a diffusing, light-driven isomerization separately from the light-driven gel contraction:

$$0 = D\nabla_\perp^2 C + K_r|A|^2(1 - C) - C \qquad (5.24)$$

Where we have defined $K_r = k_f/k_b$ and $\widetilde{D} = D/k_b$ and then have dropped the tilde. In the spatially homogeneous case where $A = A_0$ we have the solution:

$$C_0 = \frac{K_r|A_0|^2}{1 + K_r|A_0|^2} \qquad (5.25)$$

We assume that C will independently affect Δn, so equation (5.1) becomes:

$$0 = \nabla_\perp^2 A - 2ik\frac{\partial A}{\partial z} + 2k^2\frac{\Delta n(|A|^2, C)}{n_0}A \qquad (5.26)$$

Applying a small perturbation $c \ll C_0$ in addition to a leads to a small perturbation in Δn:

$$\Delta n(|A_0^2|, C) = f(|A_0^2|) + g(C) \approx 2\alpha A_0 a_1 + \beta c \qquad (5.27)$$

where

$$\beta = \left.\frac{dn}{dC}\right|_{C=C_0} < 0 \qquad (5.28)$$

B is a measure of the strength of the inhibition, related to how much the light-driven isomerization of untethered MCH causes the gel to swell. Following the same process as in Section 5.1 we get the system of equations:

$$0 = -Dk_\perp^2 c^0 + 2K_r A_0 a_1^0 - (K_r A_0^2 + 1)c^0 \tag{5.29}$$

$$0 = -k_\perp^2 a_1^0 - 2kha_2^0 + \frac{2k^2 A_0}{n_0}(2\alpha A_0 a_1 + \beta c^0) \tag{5.30}$$

$$0 = -k_\perp^2 a_2^0 + 2kha_1^0 \tag{5.31}$$

With the resulting dispersion relation:

$$b^2 = \frac{k_\perp^2}{4k^2}\left[k_\perp^2 - \frac{4k^2 A_0^2}{n_0}\left(\alpha + \frac{K_r\beta}{1 + K_r A_0^2 + Dk_\perp^2}\right)\right] \tag{5.32}$$

In contrast to modulation instability, which has a range of unstable wavelengths for any non-zero intensity, this dispersion relationship can lead to the onset of instability at only a single critical wavenumber, a Turing-type instability. By looking at the zeros of equation (5.32) we can see that the onset of instability occurs when the only solutions are $k_\perp = \{0, \pm m\}$ where m is real. We can find the requisite condition for this by solving the last term on the RHS of (5.32) for $k_\perp^2$ and considering the quadratic formula. From this we can see that $k_\perp$ will only have two distinct non-zero solutions if $k_\perp^2$ has only one solution, which will occur when the radical part of the quadratic formula, $b^2 - 4ac$, is equal to zero. From this we see that the onset of instability occurs if

$$0 = \left(4\alpha A_0^2 Dk^2 + A_0^2 K_r n_0 + n_0\right)^2 + 16A_0^2 Dk^2 K_r n_0 \beta \tag{5.33}$$

And from the non-zero part of the quadratic formula solution to $k_\perp^2$ we can immediately see that the critical wavenumber is

$$k_c = \sqrt{\frac{\sqrt{-K_r\frac{\beta}{\alpha}(1 + A_0^2 K_r - K_r\frac{\beta}{\alpha})} - (1 + A_0^2 K_r - K_r\frac{\beta}{\alpha})}{D}} \tag{5.34}$$

This can be thought of as analogous to the $k_\perp = \sqrt{K_r/D}$ relationship between critical wavenumber, characteristic reaction rate, and diffusion rate, as seen in the Turing instability. By considering that k_c must be real and greater than zero we get the additional constraint:

$$K_r \frac{\beta}{\alpha} \geq 1 + A_0^2 K_r \qquad (5.35)$$

Plugging in values from the modeling gives us $\alpha \approx 5 \times 10^{-10}$ W^{-1}. Using $K_r = 10^{-5}$ m^2 W^{-1}, $A_0^2 = 10^5$ W m^{-2}, $D/k_b = 10^{-9}$ m^2 s^{-1}, and $\beta = -1.08 \times 10^{-3}$ results in a plot of h^2 that has only a very small window of instability:
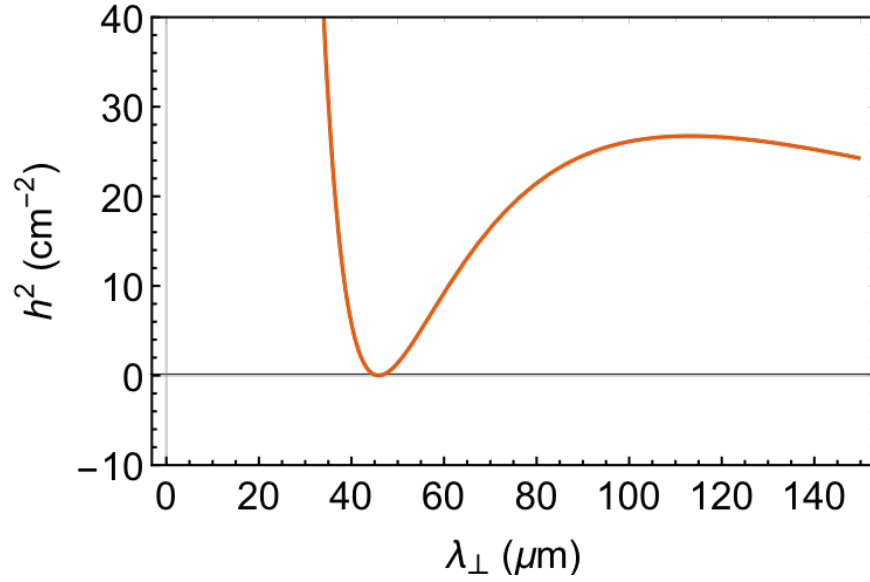
Figure 5.4: Plot of h^2 vs the perturbation wavelength for a system with a diffusing light-activated inhibitor. In contrast to modulation instability, where a large region of wavenumbers are always unstable, this system is able to undergo a Turing bifurcation in which a single critical wavenumber become unstable. For the parameters use here this occurs at $\lambda \approx 45$ μm.

5.3 Conclusions and Outlook

We have shown that a diffusing, light-activated inhibitor in spiropyran-functionalized hydrogels should, under the right circumstances, lead to a Turing-type instability. We hypothesize that this could be experimentally realized in poly(APEMA) gel with both tethered and untethered spiropyran. The theoretical results developed here can be used to guide and interpret the experiments.

Experimental demonstration of designed Turing patterns in spiropyran-functionalized hydrogels would open the door to a wide variety of exciting possibilities. Much of this thesis has been devoted to demonstrating how SP gels are a platform with many different aspects that can be rationally tuned. This tunability could then be applied to Turing patterns, where changes to the strength of activation, inhibition, or the gel's response to the environment could all affect the resulting patterns. Patterns could also be sculpted with light, where spatial changes in light intensity or wavelength could lead to spatially heterogeneous pattern formation. Altogether these techniques could be used to create bottom-up photomasks for the creation of large-scale, microstructured surfaces.

6
Conclusions and Outlook

We have demonstrated that spiropyran-functionalized hydrogels have the potential to be a designable platform for nonlinear optics applications. The physical processes leading to nonlinear optical behavior, including photoisomerization, gel poroelastic dynamics, and heat transfer, can be modeled and used to predict behavior under a variety of conditions. Different gel chemistries can be used to change relevant parameters, including the direction and magnitude of the photoresponse. Variations in the spiropyran chromophore, such as whether or not it is untethered, singly tethered, or doubly tethered,

can also be used to significantly change aspects of the gel's response. This flexibility should make SP gels a fruitful ground for future studies into the nonlinear optical dynamics of soft materials.

Despite this promise, several disadvantages of SP gels remain. One is the relatively slow timescale of observed self-trapping, which occurs over the scale of minutes. Recovery also occurs on the timescale of several minutes. While a several minute cycle time may be sufficient for use with slower physical processes, such as sun tracking or chemical sensing, it is far slower than is desired for general all-optical computer applications.

However, it is possible that further exploration and optimization could significantly improve the speed of these dynamics. We have observed some indications of full self-trapping on timescales of <1 s, followed by defocusing and then slower re-focusing (Figure 6.1). This is commensurate with our observations of fast direct photoisomerization (Figure 4.2), which occurs on a timescale of milliseconds. The several minute timescale of slower self-trapping is also not set by the timescale of poroelastic diffusion, which for a characteristic length scale of 10 microns and an estimated poroelastic diffusivity of 2×10^{-11} m^2 s^{-1} is on the order of seconds. In terms of recovery, ter Schiphorst et al.[19] have identified acrylated spiropyran monomers showing significantly faster rates of thermal ring-opening than the spiropyran molecules used in this work. All of this suggests that there is space for vast improvement in the timescale of reversible self-trapping in SP gels.

Another significant disadvantage of the SP gels we utilize is the relatively high rate of absorption. Over the 4 mm gel thickness used here to demonstrate self-trapping, about 96% of light intensity is lost, which limits applications in which the output pattern or intensity may be used to trigger further functions, such as cascaded logic gates in all-optical computing applications, or photopolymerization in the case of dynamic, reconfigurable photomasks. This high degree of absorption also likely means that the mW laser power at the input side of the gel may be higher than what is actually needed for full self-trapping. Thus achieving robust self-trapping with lower absorption has many advantages.

The easiest way to achieve this would be to lower the concentration of spiropyran. Our AFM
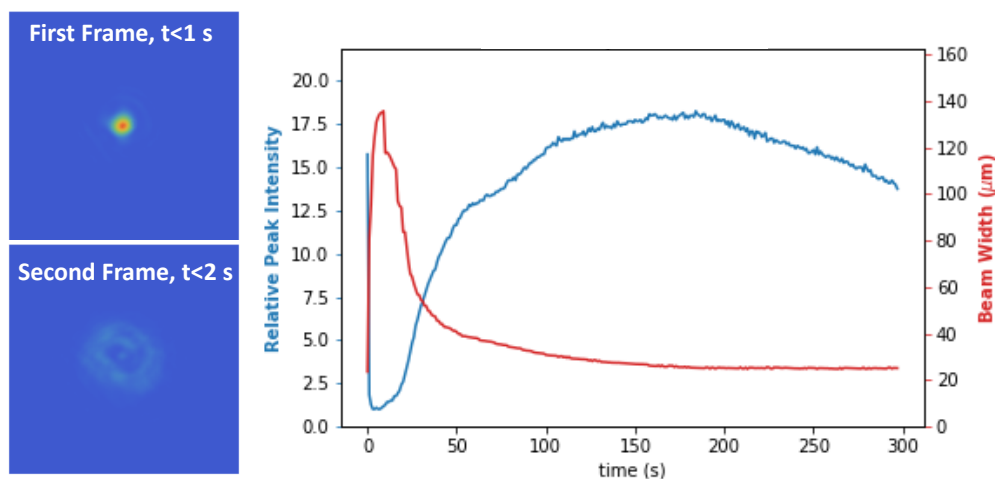
Figure 6.1: Observation of self-trapping on timescales <1 s. **(A)** First frame of a video of the exit face intensity of a spiropyran-functionalized poly(AAm-co-AAc) hydrogel with a 2 mW laser power. In the first frame (taken less than one second after the beam is switched on) the laser is observed to be fully self-trapped down to the 20 µm beam width. **(B)** The second frame from the same video as in (A) showing that the beam has begun to defocus. **(C)** Plot of the beam width and relative intensity for the full video including frames (A) and (B). The beam is observed to be fully self-trapped at the first data point, then it rapidly defocuses to a width of about 140 µm before slowly refocusing down to a 20 µm width over several minutes.

experiments already suggest that the amount of light-driven contraction is more than what is needed for self-trapping by at least an order of magnitude (Figure 2.8). Furthermore, modifications to the overall system could significantly increase the amount of contraction caused by isomerization. For example, we showed that the proton released by isomerization of MCH^+ actually increases the overall counterion pressure and contributes to a swelling pressure that counteracts the contraction caused by the change in hydrophilicity. This is true also of thermal swelling effects in poly(AAm-co-AAc) gels. Careful design of the gel chemistry to eliminate both thermal and counterion swelling could significantly enhance the gel's contraction in response to light, requiring a lower concentration of spiropyran to achieve the same degree of self-trapping, resulting also in lower total absorption.

Our experiments also suggest that much of the absorption of 532 nm light in older gels may be a result of aggregates (Figure 4.7). These aggregates would be expected to display much slower photokinetics while contributing disproportionately to the amount of absorption. Thus inhibiting the

formation of aggregates could greatly improve absorption while also potentially improving the response time. We have shown that one way to do this is to use doubly-tethered spiropyran crosslinkers (Figure 4.7). In the case of doubly-tethered spiropyran it is also possible that the conformational differences between the ring-open and ring-closed isomers may lead to an additional contraction due to the mechanical response of the polymer network to shortened crosslinks[104, 10, 53, 105]. Exploring the nonlinear optical behavior of hydrogels using doubly tethered spiropyran is a promising avenue of future research.

The ability for hydrogels to be designed to respond to a huge variety of potential stimuli (Figure 6.2) is unique among nonlinear optical materials. This additional responsivity means that nonlinear optical phenomena like self-trapping and spontaneous pattern formation can be coupled to environmental stimuli, such as extremely low concentrations of specific biomolecules in the case of aptamer functionalized gels[78]. Optical phenomena like beam bending are an ideal readout of very small changes in gel swelling due to the extreme sensitivity to very small changes in the refractive index. Using this principle one could imagine a simple sensing device made from properly functionalized light-responsive gels and a commonplace 5 mW handheld green laser (Figure 6.3). Future extensions of this idea may lead to low-power sensors for entirely-soft robotic systems or as interfaces with all-optical computing systems. These devices may also find applications in microfluidics, where a small change in biomolecule concentration could trigger the bending of a beam of light to actuate a light-responsive microfluidic valve, providing a diagnostic signal or perhaps built-in feedback.

As a final idea for the future we envision that the bottom-up, tunable optical Turing patterns proposed in Chapter 5 could be used as photomasks for the creation of large-scale microstructured materials. Since the basic principles of nonlinear optics in SP gels should work also with white, incoherent light, and the estimated intensities needed for pattern formation ($\sim 10^5$ W m^{-2}) are about two orders of magnitude greater than solar intensity ($\sim 10^3$ W m^{-2}), some focusing or tuning of the spiropyran kinetics could lead to such gels being used on a large scale with sunlight driving the pattern formation
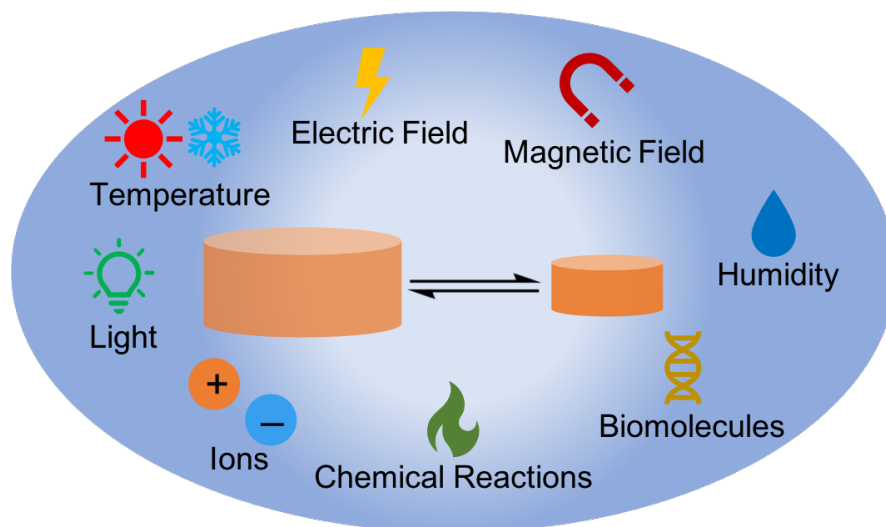
Figure 6.2: Hydrogels can be designed to be responsive to a wide variety of stimuli, including temperature[73], electric fields[71], magnetic fields[77], humidity[106], light[15, 62], ions[8, 107], chemical reactions[108], and biomolecules[78, 79].
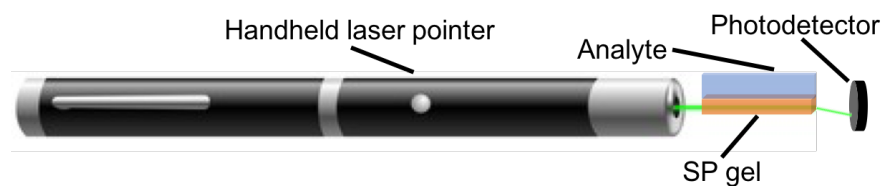
Figure 6.3: Schematic of a handheld sensor using a commonplace 5 mW 532 nm laser and a spiropyran-functionalized hydrogel and photodetector.

process. This could lead to a photomask with micron scale patterns covered objects on the scale of vehicles, airplanes, or even buildings.

Overall, the field of nonlinear optics in hydrogels is essentially brand new. Yet, already there are myriad exciting directions for future study and potential applications. We hope that this thesis provides a foundation and a starting point for these future possibilities.

A

Materials And Methods

A.1   Materials

Acrylamide, acrylic acid, N-isopropylacrylamide, 2-dimethylaminoethyl methacrylate, N,N'-methylenebis(acrylamide),
N-isopropylacrylamide, dimethyl sulfoxide (DMSO), triethylamine (TEA), tetrahydrofuran (THF),
2-Hydroxy-4′-(2-hydroxyethoxy)-2-methylpropiophenone, acryloyl chloride, trifluoroacetic acid (TFA),
acetonitrile, ethyl acetate, sodium bicarbonate, (hydroxyethyl)methacrylate (HEMA), and hydrochlo-

ric acid were all purchased from MilliporeSigma (Missouri, USA). 1',3',3'-trimethyl-6-hydroxyspiro(2H-1-benzopyran,2-2'-indoline) (Acros Organics, New Jersey, USA) was used without further purification.

A.2 Synthesis of acrylated spiropyran

Spiropyran acrylate monomer (1',3',3'-trimethylspiro[chromene-2,2'-indolin]-6-yl acrylate) was synthesized based on a procedure described previously[20]. Briefly, 1',3',3'-trimethyl-6-hydroxyspiro(2H-1-benzopyran,2-2'-indoline) was treated with acryloyl chloride and triethylamine in THF at 0 °C and reacted for 15 h at 25 °C. The product was washed in ethyl acetate with saturated aqueous sodium bicarbonate solution and brine. After the solvent was removed in a vacuum, ethyl acetate and a saturated sodium hydrogen carbonate aqueous solution were added, and the aqueous phase was extracted with ethyl acetate. The recovered organic phase was washed with brine, dried over anhydrous magnesium sulfate and filtered. After evaporation of the solvent, the residue was purified by silica gel column chromatography (1/6 ethyl acetate/n-hexane as an eluent) to obtain the acrylated spirobenzopyran monomer. Product purity was checked with H-NMR.

A.3 Synthesis of spiropyran-functionalized hydrogels

The standard method we used to make spiropyran functionalized hydrogels was to dissolve 40% w/v of the non-SP monomer in 4 : 1 v/v DMSO:deionized water. SP gels containing NIPAAm were dissolved in pure DMSO rather than a mixture with water in order to avoid phase separation during polymerization. To this solution, 2% w/v N,N'-methylenebis(acrylamide) was added as crosslinker. Acrylated spiropyran monomer was dissolved in the pre-polymer solution at a concentration of 0.25 mol% of total monomer. 2-Hydroxy-4'-(2-hydroxyethoxy)-2-methylpropiophenone was added as a photoinitiator and the hydrogel pre-polymer solution was dispensed into a rectangular aluminum

mold (4 mm × 10 mm × 0.5 mm) and sandwiched between glass slides. The polymer inside of the mold was cured under a UV lamp (60 Hz, 3.5 A, 115 V, Blak-Ray, UVP, California, USA) at ambient temperature for 5 minutes. Cured hydrogel samples were then immersed in a bath of deionized water many times the gel volume to remove unreacted monomer and excess solvent. Samples were placed into a petri dish with fresh DIW for experiments.

A.4 Synthesis of uncrosslinked linear polymers

Linear polymer solutions for UV-vis experiments were prepared using the same recipe as for gels except without any N,N'-methylenebis(acrylamide) crosslinker. Copolymers with acrylamide were made with 40% w/v comonomers at a 1 : 1 ratio. Prepolymer solutions were dispensed into a glass vial and degassed for at least 15 minutes. Subsequently, they were cured for 10 minutes under the UV lamp. Photopolymerization resulted in a viscous liquid. Subsequently, 3 mL DIW was added to the resulting polymers and the polymers redissolved in an orbital shaker overnight (16-20 hours) at 50 °C.

A.5 Optical experiments

A.5.1 Single beam

The optical assembly for single beam self-trapping experiments is shown in Figure A.1a. A continuous wave diode-pumped solid-state laser (Thorlabs, Inc., New Jersey USA) was used as the excitation source. The beam (λ = 532 nm) was collimated (L1, f = 2.54 cm) before passing through a $\lambda/2$ waveplate (W) and a polarizing beam splitter cube (C). It was then passed through an absorption filter (F) and then through a focusing lens (L2, f = 2.54 cm). This produced a beam focused to a diameter of $\sim$20 μm onto the entrance face of a hydrogel sample within the sample cell (S). The profile of the beam at the exit face of the sample was imaged by a pair of planoconvex lenses (L3, f = 25.4 mm; L4, f = 25.4 mm; total magnification = 20x) onto a charge-coupled device (CCD) camera (1200 (H) × 1600
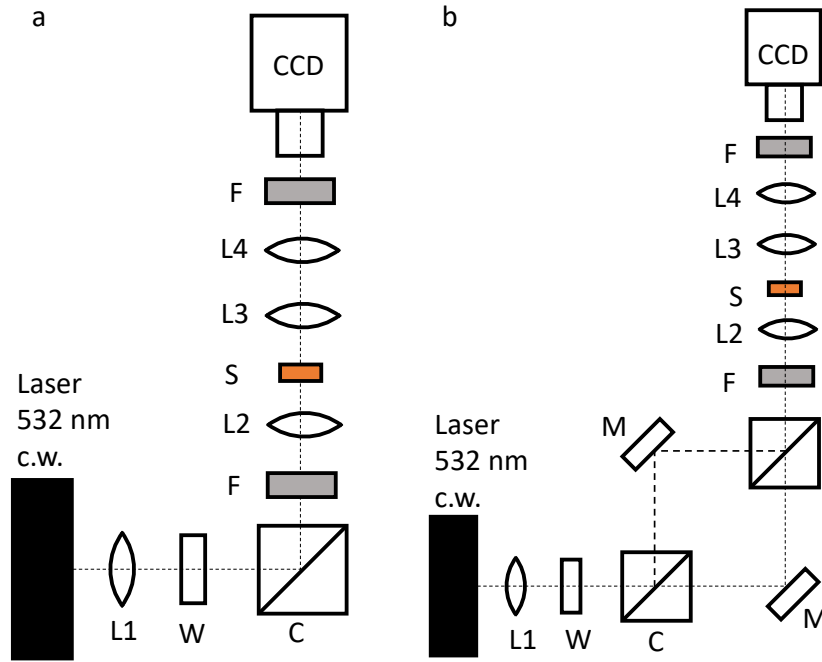
Figure A.1: a) Single beam optical self-trapping experiment including the sample (S), a $\lambda/2$ wave plate (W), polarizing beam splitter cube (C), absorption filters (F), biconvex lenses (L1-L4) and a CCD camera. **b)** Double-beam optical self-trapping experiment with additional beam splitter cube and mirrors (M).

(W) pixels, 7.4 μm (H) x 7.4 μm (W) pixel size; Retiga-2000R Colour Cooled, QImaging, British Columbia, Canada). The camera was operated using the open-source μManager software, and images were analyzed using Python and Mathematica. As beams self-trap their peak intensity increases significantly. Saturation was avoided by changing the exposure time of the camera during acquisition. Changes in exposure time were recorded and corrected for after acquisition. In all self-trapping experiments, the beam diameter was measured at the exit face of the sample. Beam radius was calculated by counting the number of pixels with intensity greater than $1/e^2$ of the peak intensity and then calculating $\sqrt{A/\pi}$ where A is the area corresponding to the number of pixels.

A.5.2 Two beam

Double beam self-trapping experiments were carried out on an optical assembly similar to the single beam setup, but with the introduction of a second beam parallel to the first beam (Figure A.1b). The output beam was passed through a $\lambda/2$ waveplate (W) and split into two beams using a polarizing beam splitter cube (C). The $\lambda/2$ waveplate orientation was adjusted to change the ratio of intensities between the two beams. The beams were directed by mirrors (M) and a second polarizing beam splitter cube, through a set of filters (F) and a biconvex lens (L2, f = 2.54 cm), which focused the beams to a diameter of 20 μm onto the entrance face of the sample in the sample cell. The separation distance between the focused beams could be adjusted using a linear stage to change the relative position of one of the mirrors. The result was two orthogonally polarized beams of light with variable separation at the entrance of the sample.

A.5.3 Glass split two-beam

Gels were prepared as described in Section A.3 except that the aluminum ring mold was cut into two pieces. Between the two halves of the ring a 4 mm by 12 mm piece of #0 glass was sandwiched with a small amount of silicone vacuum grease used to hold the assembly together. This mold was then filled with prepolymer solution and sandwiched between two glass slides before being cured under a mercury UV lamp. After curing the sandwiching glass slides were removed and the entire ring assembly with glass divider was immersed in water for three days with the water being replaced every 24 hours. After equilibration the gel shrinks slightly, and so a folded aluminum foil spacer is inserted to keep the two halves of the gel pressed against the glass divider.

A.5.4 Modulation instability

Experiments demonstrating modulation instability were conducted with 10 mm diameter by 4 mm thick poly(NIPAAm-co-AAc) gel cylinders prepared as described in Section A.3. The experimental setup was the same as the one used for single beam self trapping (Figure A.1a) except without the focusing lens L2. Thus the collimated ~1 mm wide beam was shone directly onto the gel to produce a wide region of roughly uniform intensity. A beam power of 600 μm was used. Spatial Fourier transforms of the resulting images were computed by taking a radial average of the 2D Fourier transform of a the mean-corrected intensity image. Growth factor was then computed by taking the dividing the spectral power of each Fourier component at 10 minutes by the corresponding spectral power 20 seconds after the beam was turned on. Computation and image analysis were done with Mathematica version 11.3.0.0.

A.6 Atomic Force Microscopy (AFM)

The contraction of spiropyran-functionalized p(AAm-co-AAc) hydrogels under an intense, focused c.w. 532 nm laser was measured using a JPK Instruments NanoWizard 4a atomic force microscope (AFM) with the C cantilever of an All-In-One AFM probe bought from BudgetSensors. A 532 nm c.w. laser was collimated and shone into the camera port of a Leica DMI8 inverted optical microscope upon which the AFM device was placed. Line traces of the gel surface were taken over the site where the laser was focused, and the laser was switched off and on.

Total gel thickness was measured using an upright Zeiss LSM 700 confocal microscope by determining the height of the gel surface focal plane above the focal plane of its substrate, as demonstrated in Supplementary Figure A.2. Linear contraction of the gel under laser light was then calculated by dividing the change in thickness of the gel under intense laser light by the total gel thickness.
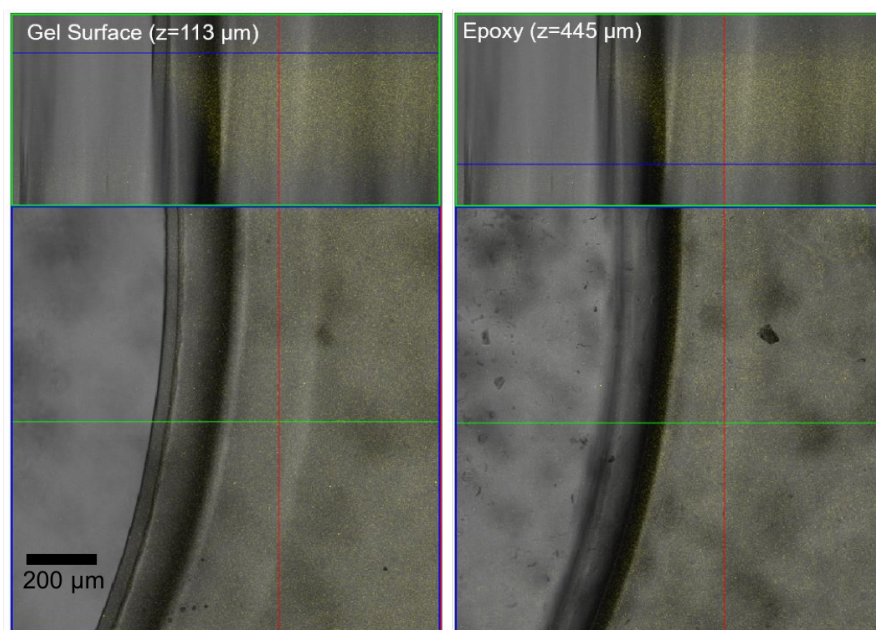
Figure A.2: Measurement of gel film thickness using optical and fluorescence microscopy.

A.7 Swelling measurements as a function of Temperature

Pre-polymer solution was prepared according to the method in Section A.3. A negative polydimethyl-siloxane (PDMS) mold patterned with small (10-100s micron width) and thin (<10 microns) cylinders was prepared using a preexisting patterned silicon wafer. Thin samples were desired for their rapid equilibrium timescale, while regular shapes were desired to simplify length/radius measurements. A small volume ($\sim$6 µL) of pre-polymer solution was deposited onto the mold and covered by a glass slide. The solution was cured directly in the mold for 5 minutes under a UV lamp (60 Hz, 3.5 A, 115 V, Blak-Ray, UVP, CA, USA). The mold was then immersed in deionized water to release the gel samples.

For all measurements, the temperature was manually adjusted using an Instec STC 200 temperature controller. During experiments, the gels were contained in a sample holder consisting of a custom

3.8 cm × 3.8 cm × 0.6 cm aluminum block with a 1.3 cm diameter hole through its center. The aluminum block was sandwiched between two glass slides adhered on each side of the hole with vacuum grease, thus creating a sealed, transparent well in which the samples could be deposited and equilibrated in deionized water. The sample holder was placed under a Zeiss LSM 700 confocal microscope on a stage connected to the temperature controller. The temperature was adjusted at regular intervals (5 °C). Corresponding images of the gel samples at each temperature setpoint were captured using a compatible software (ZEN Black 2011).

The radius measurements were obtained by first processing the image using a Gaussian filter, followed by applying Hough circle transform provided by the OpenCV Python library. The function performs edge detection, then determines a circle center and calculates a radius. For each image set, an appropriate set of parameters (minimum and maximum radius, distance between circles, edge intensity, etc.) was used. As these gels swell isotropically, the swelling ratio is $S = [r(T)/r(T_0)]^3$, where S is the swelling ratio, $r(T)$ is the radius at temperature T, and $r(T_0)$ is the radius at the initial temperature.

A.8   UV-vis

Buffer solutions for absorption measurements of the linear polymers were prepared at 0.2 M using appropriate amounts of citrate buffer for the pH range 3 to 6, and phosphate buffer for the pH range 6 to 8.5. These buffers were adjusted to their final pH with aqueous sodium hydroxide or hydrogen chloride solutions. Solutions of linear polymers were freshly prepared by diluting 35 μL of polymer solution in 2 mL of 0.2 M pH buffers. UV-vis spectra were obtained on an Agilent 8453 UV-vis diode array spectrophotometer equipped with a Peltier-based temperature-controlled cuvette holder (Agilent). Samples were prepared from deionized water and measured in cuvettes (disposable PMMA cuvettes) of 10 mm pathlength. Spectra were baseline corrected for their absorption at 700 nm. UV-vis

spectra of linear polymer solutions were normalized with respect to their absorption at 279 nm (Irgacure 2959). Data-analysis was performed using GraphPad–Prism, R (https://www.r-project.org/) and Spectragryph software.

A.9 Confocal Fluoresence Microscopy

All measurements were taken on a Zeiss LSM 710 confocal microscope. Gel samples were immersed in deionized water in a polystyrene petri dish, and a 10x Zeiss water immersion lens was used for imaging. For an excitation wavelength of 561 nm we measured fluorescence intensity in a window of 625 to 675 nm, while for 405 nm excitation we use a window of 525 to 575 nm, corresponding to the fluorescence emission of MC and MCH$^+$ respectively. Excitation and fluorescence measurement can be done either in a single focused spot, or scanned over an area, and the excitation power can be controlled from μW to mW. For experiments we used two different intensities: a high-intensity to observe light-driven isomerization dynamics, and a low-intensity with short exposure times to observe dark thermally-driven isomerization dynamics. High-intensity experiments correspond to a power of 5.5 mW for 561 nm light and 4.7 mW for 405 nm light. Low-intensity experiments used a power of 9.1 μW for 561 nm light and 5.6 μW for 405 nm light. Laser power was measured with a PM120D Si photodiode power sensor (Thorlabs).

B

Poroelastic Diffusivity Measurement

The poroelastic diffusivity of the spiropyran-modified p(AAm-co-AAc) hydrogels was measured using the method described in Hu et al[56]. Briefly, this method involves indenting a bulk hydrogel sample immersed in water and measuring the force relaxation over time. We used a cylindrical punch of radius 559 µm. For a cylindrical punch the given empirical formula used to solve for the poroelastic
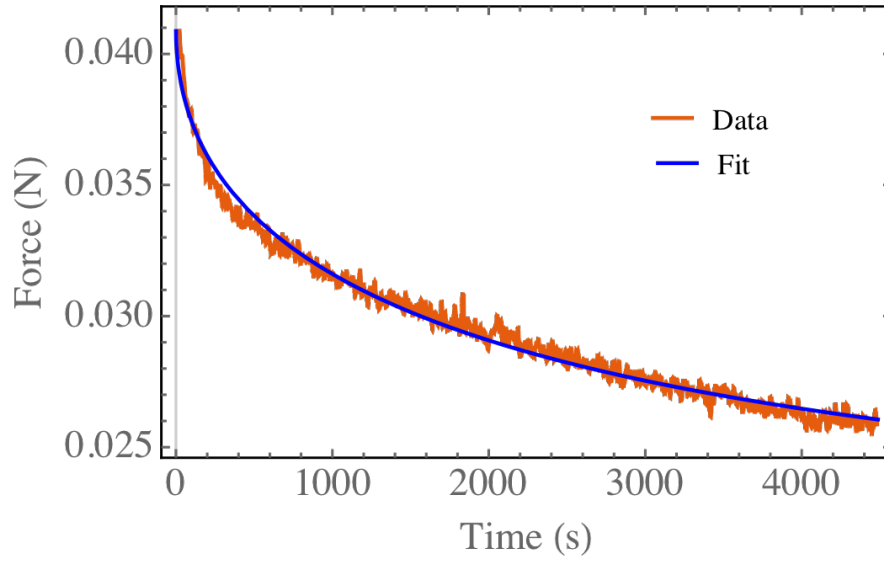
Figure B.1: Measurement of force over time for a constant indentation with a cylindrical punch of radius 559 μm. The blue line shows a fit of equation (B.1)

.

diffusivity D is:

$$\frac{F(t) - F(\infty)}{F(0) - F(\infty)} = 1.304e^{-\sqrt{\frac{Dt}{a^2}}} - 0.304e^{-0.254\frac{Dt}{a^2}} \tag{B.1}$$

Where $F(t)$ is the force as a function of time t, and a is the radius of the cylindrical punch. We fit equation (B.1) to the force measurement data with D and $F(\infty)$ as free parameters using Mathematica version 11.3.0.0's built in NonlinearModelFit function. The best fit value of D was found to be 1.8×10^{-11} m^2 s^{-1}, and the fit is shown in Figure B.1.

C

Model of Counterion Pressure in Weak

Polyelectrolytes

We developed a model that calculates the counterion pressure as a function of gel composition, spiropyran isomer concentrations, external ionic strength, and external pH, based on the model of Doi et

al.[71]. In this model the counterion osmotic pressure Π is defined as:

$$\frac{\Pi}{RT} = \sum_i (c_{ig} - c_{is}) \tag{C.1}$$

Where c_{ig} is the concentration of the ith mobile counterion in the gel, and c_{is} is the concentration of the ith mobile counterion in the external solution. R is the gas constant and T is the temperature. The mobile species we consider are a cationic salt A, an anionic salt B, protons H, hydroxyls OH, and in the case of untethered, sulfonated spiropyran we have the negatively charged ring-open merocyanine MC and the ring-closed spiropyran SP. The Donnan equilibrium theory describes how the immobility of the fixed polyions in the gel leads to the formation of an electric double layer at the gel boundary and a corresponding potential drop $\Delta\psi$. This potential is related to the difference in ion concentrations by

$$\frac{c_{ig}}{c_{is}} = e^{-z_i \Delta\psi} \tag{C.2}$$

Where z_i is the charge of the ith mobile counterion. We can also write the charge neutrality condition for the solution phase

$$c_{As} + c_{Hs} = c_{Bs} + c_{OHs} + c_{MCs} + c_{SPs} \tag{C.3}$$

and the gel phase

$$c_{Ag} + c_{Hg} + z_m c_m + z_{mH} c_{mH} = c_{Bg} + c_{OHg} + c_{MCg} + c_{SPg} \tag{C.4}$$

where z_m is the charge of the mth unprotonated polymer moiety and c_m is the concentration of the mth unprotonated polymer moiety, while mH corresponds to the protonated form. The protonation

equilibrium of each moiety is determined based on the K_a:

$$K_{a,m} = \frac{[m][H^+]}{[mH]} \tag{C.5}$$

The water dissociation and MC protonation equilibria are

$$K_w = [OH^-][H^+] = 10^{-14} \tag{C.6}$$

$$K_{MC} = \frac{[MC][H^+]}{[MCH]} \tag{C.7}$$

We use a pK_a of 4.5 for carboxylic acid moieties[109], 6.5 for MC (Figure 4.8), 8.6 for DMAEMA[110], and 4.6 for aniline moieties[74]. Finally, the total number of polymer moieties of each species is conserved:

$$c_{m,total} = c_m + c_{mH} \tag{C.8}$$

The equations (C.2) through (C.8) allow us to solve for each c_{ig}, c_m, and c_{mH} given the set of c_{is}. The pH of the external solution is set by the difference between c_{As} and c_{Bs}, while the effect of light is imposed by setting c_{MCs}, c_{MCHs}, and c_{SPs}. For simplicity we assume a total spiropyran concentration of 14 mM, and that all spiropyran molecules exist as MC or MCH in the dark, while there is complete conversion to SP upon irradiation. Once the concentrations of all species within the gel are known the osmotic pressure can be calculated using equation (C.1). $\Delta\Pi$ between light and dark is then determined assuming that both systems are at the same temperature. Results for gels in solutions of varying pH and an ionic strength of 20 mM are shown in Figure 3.1. The concentration of carboxylic acid, amino, or aniline moiety in each gel is set to be 100 mM.

References

[1] B. K. Connizzo, S. M. Yannascoli, and L. J. Soslowsky, "Structure–function relationships of postnatal tendon development: A parallel to healing," *Matrix Biol.*, vol. 32, no. 2, pp. 106–116, 2013.

[2] O. Lieleg and K. Ribbeck, "Biological hydrogels as selective diffusion barriers," *Trends Cell Biol.*, vol. 21, no. 9, pp. 543–551, 2011.

[3] A. J. Sophia Fox, A. Bedi, and S. A. Rodeo, "The basic science of articular cartilage: Structure, composition, and function," *Sports Health*, vol. 1, no. 6, pp. 461–468, 2009.

[4] M. Bahram, N. Mohseni, and M. Moghtader, "An Introduction to Hydrogels and Some Recent Applications," in *Emerg. Concepts Anal. Appl. Hydrogels*, InTech, 2016.

[5] J. Li, Z. Suo, and J. J. Vlassak, "A model of ideal elastomeric gels for polyelectrolyte gels," *Soft Matter*, vol. 10, no. 15, pp. 2582–2590, 2014.

[6] O. E. Philippova, "Responsive polymer gels," *Polymer Science - Series C*, vol. 42, no. 2, pp. 208–228, 2000.

[7] Y. Lee, W. J. Song, and J.-Y. Sun, "Hydrogel soft robotics," *Materials Today Physics*, p. 100258, 2020.

[8] D. J. Beebe, J. S. Moore, J. M. Bauer, Q. Yu, R. H. Liu, C. Devadoss, and B.-H. Jo, "Functional hydrogel structures for autonomous flow control inside microfluidic channels," *Nature*, vol. 404, no. 6778, pp. 588–590, 2000.

[9] L. Dong and H. Jiang, "Autonomous microfluidics with stimuli-responsive hydrogels," *Soft Matter*, vol. 3, no. 10, p. 1223, 2007.

[10] R. Klajn, "Spiropyran-based dynamic materials," *Chem. Soc. Rev.*, vol. 43, no. 1, pp. 148–184, 2014.

[11] L. Kortekaas and W. R. Browne, "The evolution of spiropyran: fundamentals and progress of an extraordinarily versatile photochrome," *Chem. Soc. Rev.*, vol. 48, no. 12, pp. 3406–3424, 2019.

[12] A. Suzuki and T. Tanaka, "Phase transition in polymer gels induced by visible light," *Nature*, vol. 346, no. 6282, pp. 345–347, 1990.

[13] A. Sutton, T. Shirman, J. V. I. Timonen, G. T. England, P. Kim, M. Kolle, T. Ferrante, L. D. Zarzar, E. Strong, and J. Aizenberg, "Photothermally triggered actuation of hybrid materials as a new platform for in vitro cell manipulation," *Nature Communications*, vol. 8, p. 14700, 2017.

[14] D. R. Morim, A. Meeks, A. Shastri, A. Tran, A. V. Shneidman, V. V. Yashin, F. Mahmood, A. C. Balazs, J. Aizenberg, and K. Saravanamuttu, "Opto-chemo-mechanical transduction in photoresponsive gels elicits switchable self-trapped beams with remote interactions," *Proceedings of the National Academy of Sciences of the United States of America*, vol. 117, no. 8, pp. 3953–3959, 2020.

[15] B. Ziółkowski, L. Florea, J. Theobald, F. Benito-Lopez, and D. Diamond, "Self-protonating spiropyran-co-NIPAM-co-acrylic acid hydrogel photoactuators," *Soft Matter*, vol. 9, no. 36, pp. 8754–8760, 2013.

[16] B. Ziółkowski, L. Florea, J. Theobald, F. Benito-Lopez, and D. Diamond, "Porous self-protonating spiropyran-based NIPAAm gels with improved reswelling kinetics," *Journal of Materials Science*, vol. 51, no. 3, pp. 1392–1399, 2016.

[17] T. Satoh, K. Sumaru, T. Takagi, and T. Kanamori, "Fast-reversible light-driven hydrogels consisting of spirobenzopyran- functionalized poly(N-isopropylacrylamide)," *Soft Matter*, vol. 7, no. 18, pp. 8030–8034, 2011.

[18] K. Sumaru, T. Takagi, S. Sugiura, and T. Kanamori, "Spiropyran-Functionalized Hydrogels," in *Soft Actuators*, pp. 309–320, Springer Singapore, 2019.

[19] J. Ter Schiphorst, S. Coleman, J. E. Stumpel, A. Ben Azouz, D. Diamond, and A. P. Schenning, "Molecular Design of Light-Responsive Hydrogels, for in Situ Generation of Fast and Reversible Valves for Microfluidic Applications," *Chemistry of Materials*, vol. 27, no. 17, pp. 5925–5931, 2015.

[20] S. Sugiura, A. Szilágyi, K. Sumaru, K. Hattori, T. Takagi, G. Filipcsei, M. Zrínyi, and T. Kanamori, "On-demand microfluidic control by micropatterned light irradiation of a photoresponsive hydrogel sheet," *Lab on a Chip*, vol. 9, no. 2, pp. 196–198, 2009.

[21] S. Sugiura, K. Sumaru, K. Ohi, K. Hiroki, T. Takagi, and T. Kanamori, "Photoresponsive polymer gel microvalves controlled by local light irradiation," *Sensors and Actuators, A: Physical*, vol. 140, no. 2, pp. 176–184, 2007.

[22] J. ter Schiphorst, G. G. Melpignano, H. E. Amirabadi, M. H. Houben, S. Bakker, J. M. den Toonder, and A. P. Schenning, "Photoresponsive Passive Micromixers Based on Spiropyran Size-Tunable Hydrogels," *Macromolecular Rapid Communications*, vol. 39, no. 1, 2018.

[23] W. Francis, A. Dunne, C. Delaney, L. Florea, and D. Diamond, "Spiropyran based hydrogels actuators—Walking in the light," *Sensors and Actuators, B: Chemical*, vol. 250, pp. 608–616, 2017.

[24] R. Tong, H. D. Hemmati, R. Langer, and D. S. Kohane, "Photoswitchable nanoparticles for triggered tissue penetration and drug delivery," *Journal of the American Chemical Society*, vol. 134, no. 21, pp. 8848–8855, 2012.

[25] G. I. Stegeman and M. Segev, "Optical Spatial Solitons and Their Interactions: Universality and Diversity.," *Science (New York, N.Y.)*, vol. 286, no. 5444, pp. 1518–1523, 1999.

[26] S. Biria, D. R. Morim, F. A. Tsao, K. Saravanamuttu, and I. D. Hosein, "Coupling nonlinear optical waves to photoreactive and phase-separating soft matter: Current status and perspectives," *Chaos*, vol. 27, no. 10, p. 104611, 2017.

[27] R. Y. Chiao, E. Garmire, and C. H. Townes, "Self-trapping of optical beams," *Phys. Rev. Lett.*, vol. 13, no. 15, pp. 479–482, 1964.

[28] S. Trillo and W. Torruellas, eds., *Spatial Solitons*, vol. 82 of *Springer Series in Optical Sciences*. Berlin, Heidelberg: Springer Berlin Heidelberg, 2001.

[29] A. W. Snyder and A. P. Sheppard, "Collisions, steering, and guidance with spatial solitons," *Opt. Lett.*, vol. 18, no. 7, p. 482, 1993.

[30] W. Królikowski and S. A. Holmstrom, "Fusion and birth of spatial solitons upon collision," *Opt. Lett.*, vol. 22, no. 6, p. 369, 1997.

[31] W. Królikowski, B. Luther-Davies, C. Denz, and T. Tschudi, "Annihilation of photorefractive solitons," *Opt. Lett.*, vol. 23, no. 2, p. 97, 1998.

[32] A. V. Buryak, Y. S. Kivshar, M. F. Shih, and M. Segev, "Induced coherence and stable soliton spiraling," *Phys. Rev. Lett.*, vol. 82, no. 1, pp. 81–84, 1999.

[33] M. Peccianti, C. Conti, G. Assanto, A. De Luca, and C. Umeton, "All-optical switching and logic gating with spatial solitons in liquid crystals," *Applied Physics Letters*, vol. 81, no. 18, pp. 3335–3337, 2002.

[34] C. Rotschild, B. Alfassi, O. Cohen, and M. Segev, "Long-range interactions between optical solitons," *Nature Physics*, vol. 2, no. 11, pp. 769–774, 2006.

[35] S. Jradi, O. Soppera, and D. J. Lougnot, "Fabrication of polymer waveguides between two optical fibers using spatially controlled light-induced polymerization," *Appl. Opt.*, vol. 47, no. 22, pp. 3987–3993, 2008.

[36] J. Yang, P. Zhang, M. Yoshihara, Y. Hu, and Z. Chen, "Image transmission using stable solitons of arbitrary shapes in photonic lattices," *Opt. Lett.*, vol. 36, no. 5, p. 772, 2011.

[37] Y. Kivshar, "Bending light at will," *Nat. Phys.*, vol. 2, pp. 729–730, nov 2006.

[38] A. W. Snyder and F. Ladouceur, "Light Guiding Light: Letting Light Be the Master of Its Own Destiny," *Optics & Photonics News*, vol. 10, no. February, pp. 35–39, 1999.

[39] R. W. Boyd, *Nonlinear optics*. Amsterdam: Academic Press, 3rd ed. ed., 2008.

[40] K. D. Moll, A. L. Gaeta, and G. Fibich, "Self-Similar Optical Wave Collapse: Observation of the Townes Profile," *Phys. Rev. Lett.*, vol. 90, no. 20, p. 4, 2003.

[41] G. C. Duree, J. L. Shultz, G. J. Salamo, M. Segev, A. Yariv, B. Crosignani, P. Di Porto, E. J. Sharp, and R. R. Neurgaonkar, "Observation of self-trapping of an optical beam due to the photorefractive effect," *Phys. Rev. Lett.*, vol. 71, pp. 533–536, jul 1993.

[42] M. Segev, B. Crosignani, A. Yariv, and B. Fischer, "Spatial solitons in photorefractive media," *Phys. Rev. Lett.*, vol. 68, no. 7, pp. 923–926, 1992.

[43] I. Andrade-Silva, U. Bortolozzo, M. G. Clerc, G. González-Cortés, S. Residori, and M. Wilson, "Spontaneous light-induced Turing patterns in a dye-doped twisted nematic layer," *Scientific Reports*, vol. 8, no. 1, p. 12867, 2018.

[44] C. Conti, M. Peccianti, and G. Assanto, "Route to Nonlocality and Observation of Accessible Solitons," *Phys. Rev. Lett.*, vol. 91, no. 7, p. 73901, 2003.

[45] I. B. Burgess, M. R. Ponte, and K. Saravanamuttu, "Spontaneous formation of 3-D optical and structural lattices from two orthogonal and mutually incoherent beams of white light propagating in a photopolymerisable material," *Journal of Materials Chemistry*, vol. 18, no. 35, p. 4133, 2008.

[46] A. D. Hudson, M. R. Ponte, F. Mahmood, T. Pena Ventura, and K. Saravanamuttu, "A soft photopolymer cuboid that computes with binary strings of white light," *Nature Communications*, vol. 10, no. 1, p. 2310, 2019.

[47] A. D. Hudson, C. Bacus, M. Whinton, M. A. Brook, and K. Saravanamuttu, "Single-Step Generation of Flexible, Free-Standing Arrays of Multimode Cylindrical Waveguides," *Advanced Engineering Materials*, vol. 21, no. 2, p. 1800875, 2019.

[48] D. R. Morim, I. Vargas-Baca, and K. Saravanamuttu, "Reversibly Trapping Visible Laser Light through the Catalytic Photo-oxidation of I^- by $Ru(bpy)_3^{2+}$," *Journal of Physical Chemistry Letters*, vol. 7, no. 8, pp. 1585–1589, 2016.

[49] O. Kuksenok and A. C. Balazs, "Modeling the photoinduced reconfiguration and directed motion of polymer gels," *Advanced Functional Materials*, vol. 23, no. 36, pp. 4601–4610, 2013.

[50] M. Dehghany, H. Zhang, R. Naghdabadi, and Y. Hu, "A Thermodynamically-Consistent Large Deformation Theory Coupling Photochemical Reaction and Electrochemistry for Light-Responsive Gels," *Journal of the Mechanics and Physics of Solids*, no. 17, 2018.

[51] V. V. Yashin and A. C. Balazs, "Theoretical and computational modeling of self-oscillating polymer gels," *Journal of Chemical Physics*, vol. 126, no. 12, p. 124707, 2007.

[52] Chemical Retrieval on the Web, "Polymer Properties Database." 2015. http://polymerdatabase.com/home.html. Online; accessed 3 March 2021.

[53] A. Shastri, *Integrated Stimuli-Responsive Functionalities:From Bioseparation to Dynamic Optics*. Doctoral dissertation, Harvard University, 2016.

[54] T. Takigawa, Y. Morino, K. Urayama, and T. Masuda, "Poisson's Ratio of Polyacrylamide (PAAm) Gels," *Polym. Gels Networks*, vol. 4, no. 1, pp. 1–5, 1996.

[55] T. Boudou, J. Ohayon, C. Picart, R. I. Pettigrew, and P. Tracqui, "Nonlinear elastic properties of polyacrylamide gels: Implications for quantification of cellular forces," *Biorheology*, vol. 46, no. 3, pp. 191–205, 2009.

[56] Y. Hu, X. Zhao, J. J. Vlassak, and Z. Suo, "Using indentation to characterize the poroelasticity of gels," *Applied Physics Letters*, vol. 96, no. 12, p. 121904, 2010.

[57] A. B. Villafranca and K. Saravanamuttu, "An experimental study of the dynamics and temporal evolution of self-trapped laser beams in a photopolymerizable organosiloxane," *J. Phys. Chem. C*, vol. 112, no. 44, pp. 17388–17396, 2008.

[58] A. Meeks, R. Mac, S. Chathanat, and J. Aizenberg, "Tunable Long-Range Interactions between Self-Trapped Beams driven by the Thermal Response of Photoresponsive Hydrogels," *Chemistry of Materials*, vol. 32, no. 24, pp. 10594–10600, 2020.

[59] E. Y. Kramarenko, O. E. Philippova, and A. R. Khokhlov, "Polyelectrolyte networks as highly sensitive polymers," *Polym. Sci. Ser. C*, vol. 48, pp. 1–20, jul 2006.

[60] G. Schuszter, T. Gehér-Herczegh, Á. Szucs, Á. Tóth, and D. Horváth, "Determination of the diffusion coefficient of hydrogen ion in hydrogels," *Physical Chemistry Chemical Physics*, vol. 19, no. 19, pp. 12136–12143, 2017.

[61] Y. Hirata, Y. Kato, N. Andoh, N. Fujiwara, and R. Ito, "Measurements of thermophysical properties of polyacrylamide gel used for electrophoresis.," *Journal of Chemical Engineering of Japan*, vol. 26, no. 2, pp. 143–147, 1993.

[62] C. Li, A. Iscen, L. C. Palmer, G. C. Schatz, and S. I. Stupp, "Light-Driven Expansion of Spiropyran Hydrogels," *Journal of the American Chemical Society*, vol. 142, no. 18, pp. 8447–8453, 2020.

[63] M. Hammarson, J. R. Nilsson, S. Li, T. Beke-Somfai, and J. Andréasson, "Characterization of the thermal and photoinduced reactions of photochromic spiropyrans in aqueous solution," *Journal of Physical Chemistry B*, vol. 117, no. 43, pp. 13561–13571, 2013.

[64] T. Stafforst and D. Hilvert, "Kinetic characterization of spiropyrans in aqueous media," *Chemical Communications*, vol. 0, no. 3, pp. 287–288, 2009.

[65] D. S. Achilleos and M. Vamvakaki, "Multiresponsive spiropyran-based copolymers synthesized by atom transfer radical polymerization," *Macromolecules*, vol. 43, no. 17, pp. 7073–7081, 2010.

[66] G. Assanto, M. Peccianti, and C. Conti, "Nematicons: Optical Spatial Solitons in Nematic Liquid Crystals," *Optics and Photonics News*, vol. 14, no. 2, p. 44, 2003.

[67] H. M. Bandara and S. C. Burdette, "Photoisomerization in different classes of azobenzene," *Chem. Soc. Rev.*, vol. 41, no. 5, pp. 1809–1825, 2012.

[68] A. Goulet-Hanssens, F. Eisenreich, and S. Hecht, "Enlightening Materials with Photoswitches," *Adv. Mater.*, vol. 32, no. 20, 2020.

[69] Z. Shi, P. Peng, D. Strohecker, and Y. Liao, "Long-lived photoacid based upon a photochromic reaction," *Journal of the American Chemical Society*, vol. 133, no. 37, pp. 14699–14703, 2011.

[70] P. J. Flory and J. Rehner, "Statistical mechanics of cross-linked polymer networks II. Swelling," *The Journal of Chemical Physics*, vol. 11, no. 11, pp. 521–526, 1943.

[71] M. Doi, M. Matsumoto, and Y. Hirose, "Deformation of Ionic Polymer Gels by Electric Fields," *Macromolecules*, vol. 25, no. 20, pp. 5504–5511, 1992.

[72] A. E. Ivanov, N. L. Eremeev, P. O. Wahlund, I. Y. Galaev, and B. Mattiasson, "Photosensitive copolymer of N-isopropylacrylamide and methacryloyl derivative of spyrobenzopyran," *Polymer*, vol. 43, no. 13, pp. 3819–3823, 2002.

[73] C. Zhao, Z. Ma, and X. X. Zhu, "Rational design of thermoresponsive polymers in aqueous solutions: A thermodynamics map," *Progress in Polymer Science*, vol. 90, pp. 269–291, 2019.

[74] National Center for Biotechnology Information, "PubChem Compound Summary for CID 6115, Aniline." 2021. https://pubchem.ncbi.nlm.nih.gov/compound/Aniline. Online; accessed 8 March 2021.

[75] D. R. Morim, D. Bevern, I. Vargas-Baca, and K. Saravanamuttu, "3-D Spiraling Self-Trapped Light Beams in Photochemical Systems," *The Journal of Physical Chemistry Letters*, vol. 10, no. 19, pp. 5957–5962, 2019.

[76] X. Liu, J. Liu, S. Lin, and X. Zhao, "Hydrogel machines," *Mater. Today*, vol. 36, pp. 102–124, 2020.

[77] X. Zhao, J. Kim, C. A. Cezar, N. Huebsch, K. Lee, K. Bouhadir, and D. J. Mooney, "Active scaffolds for on-demand drug and cell delivery," *Proc. Natl. Acad. Sci. U. S. A.*, vol. 108, no. 1, pp. 67–72, 2011.

[78] S. W. Bae, J. S. Lee, V. M. Harms, and W. L. Murphy, "Dynamic, Bioresponsive Hydrogels via Changes in DNA Aptamer Conformation," *Macromol. Biosci.*, vol. 19, no. 2, pp. 1–6, 2019.

[79] A. Cangialosi, C. K. Yoon, J. Liu, Q. Huang, J. Guo, T. D. Nguyen, D. H. Gracias, and R. Schulman, "DNA sequence–directed shape change of photopatterned hydrogels via high-degree swelling," *Science*, vol. 357, no. 6356, pp. 1126–1130, 2017.

[80] G. Such, R. A. Evans, L. H. Yee, and T. P. Davis, "Factors Influencing Photochromism of Spiro-Compounds Within Polymeric Matrices," *Journal of Macromolecular Science - Polymer Reviews*, vol. 43, no. 4, pp. 547–579, 2003.

[81] M. J. Feeney and S. W. Thomas, "Tuning the Negative Photochromism of Water-Soluble Spiropyran Polymers," *Macromolecules*, vol. 51, no. 20, pp. 8027–8037, 2018.

[82] J. E. Stumpel, D. Liu, D. J. Broer, and A. P. Schenning, "Photoswitchable hydrogel surface topographies by polymerisation-induced diffusion," *Chemistry - A European Journal*, vol. 19, no. 33, pp. 10922–10927, 2013.

[83] E. Goldburt, F. Shvartsman, S. Fishman, and V. Krongauz, "Intramolecular interactions in photochromic spiropyran-merocyanine polymers," *Macromolecules*, vol. 17, no. 6, pp. 1225–1230, 1984.

[84] E. Goldburt and V. Krongauz, "A simple relationship between rate of color change and molecular weight of a photochromic spiropyran polymer," *Macromolecules*, vol. 19, no. 1, pp. 246–247, 1986.

[85] E. Goldburt, F. Shvartsman, and V. Krongauz, ""Zipper" crystallization of polymers with spiropyran side groups," *Macromolecules*, vol. 17, no. 9, pp. 1876–1878, 1984.

[86] C. Berton, D. M. Busiello, S. Zamuner, E. Solari, R. Scopelliti, F. Fadaei-Tirani, K. Severin, and C. Pezzato, "Thermodynamics and kinetics of protonated merocyanine photoacids in water," *Chemical Science*, vol. 11, no. 32, pp. 8457–8468, 2020.

[87] V. M. Breslin and M. A. Garcia-Garibay, "Transmission spectroscopy and kinetics in crystalline solids using aqueous nanocrystalline suspensions: The spiropyran-merocyanine photochromic system," *Cryst. Growth Des.*, vol. 17, pp. 637–642, feb 2017.

[88] V. I. Bespalov and V. I. Talanov, "Filamentary Structure of Light Beams in Nonlinear Liquids," *ZhETF Pis ma Redaktsiiu*, vol. 3, pp. 471–476, 1966.

[89] M. Soljacic, M. Segev, T. Coskun, D. N. Christodoulides, and A. Vishwanath, "Modulation Instability of Incoherent Beams in Noninstantaneous Nonlinear Media," *Physical Review Letters*, vol. 84, no. 3, pp. 467–470, 2000.

[90] A. M. Turing, "The Chemical Basis of Morphogenesis," *Philos. Trans. R. Soc. Lond. B. Biol. Sci.*, vol. 237, no. 641, pp. 37–72, 1952.

[91] I. Lengyel and I. R. Epstein, "Turing Structures in Simple Chemical Reactions," *Acc. Chem. Res*, vol. 26, pp. 235–240, 1993.

[92] A. Preska Steinberg, I. R. Epstein, and M. Dolnik, "Target turing patterns and growth dynamics in the chlorine dioxide-iodine-malonic acid reaction," *Journal of Physical Chemistry A*, vol. 118, no. 13, pp. 2393–2400, 2014.

[93] A. Blagodatski, A. Sergeev, M. Kryuchkov, Y. Lopatina, and V. L. Katanaev, "Diverse set of Turing nanopatterns coat corneae across insect lineages," *Proceedings of the National Academy of Sciences*, vol. 112, no. 34, pp. 10750–10755, 2015.

[94] S. A. Newman, "The Turing mechanism in vertebrate limb patterning," *Nat. Rev. Mol. Cell Biol.*, vol. 8, no. 6, pp. 1–1, 2007.

[95] D. Karig, K. Michael Martini, T. Lu, N. A. DeLateur, N. Goldenfeld, and R. Weiss, "Stochastic Turing patterns in a synthetic bacterial population," *Proc. Natl. Acad. Sci. U. S. A.*, vol. 115, no. 26, pp. 6572–6577, 2018.

[96] S. Guo, M.-z. Sun, and X. Zhao, "Wavelength of a Turing-type mechanism regulates the morphogenesis of meshwork patterns," *Sci. Rep.*, vol. 11, no. 1, p. 4813, 2021.

[97] D. Menshykau, O. Michos, C. Lang, L. Conrad, A. P. McMahon, and D. Iber, "Image-based modeling of kidney branching morphogenesis reveals GDNF-RET based Turing-type mechanism and pattern-modulating WNT11 feedback," *Nat. Commun.*, vol. 10, no. 1, pp. 1–13, 2019.

[98] S. Okuda, T. Miura, Y. Inoue, T. Adachi, and M. Eiraku, "Combining Turing and 3D vertex models reproduces autonomous multicellular morphogenesis with undulation, tubulation, and branching," *Sci. Rep.*, vol. 8, no. 1, p. 2386, 2018.

[99] H. Liu, J. A. Pojman, Y. Zhao, C. Pan, J. Zheng, L. Yuan, A. K. Horváth, and Q. Gao, "Pattern formation in the iodate-sulfite-thiosulfate reaction-diffusion system," *Physical Chemistry Chemical Physics*, vol. 14, no. 1, pp. 131–137, 2012.

[100] D. E. Strier, P. De Kepper, and J. Boissonade, "Turing patterns, spatial bistability, and front interactions in the [ClO^2, I^2, I^-, $CH_2(COOH)_2$] reaction," *Journal of Physical Chemistry A*, vol. 109, no. 7, pp. 1357–1363, 2005.

[101] J. Horváth, I. Szalai, and P. De Kepper, "An experimental design method leading to chemical Turing patterns.," *Science*, vol. 324, no. 5928, pp. 772–775, 2009.

[102] V, Castets and E, Dulos and J, Boissonade and P, De Kepper, "Experimental Evidence of a Sustained Standing Turing-Type Nonequilibrium Chemical Pattern," *Phys. Rev. Lett.*, vol. 64, no. 24, pp. 2953–2957, 1990.

[103] K. Showalter and I. R. Epstein, "From chemical systems to systems chemistry: Patterns in space and time," *Chaos An Interdiscip. J. Nonlinear Sci.*, vol. 25, no. 9, p. 097613, 2015.

[104] C. M. Kingsbury, P. A. May, D. A. Davis, S. R. White, J. S. Moore, and N. R. Sottos, "Shear activation of mechanophore-crosslinked polymers," *J. Mater. Chem.*, vol. 21, no. 23, pp. 8381–8388, 2011.

[105] H. Chen, F. Yang, Q. Chen, and J. Zheng, "A Novel Design of Multi-Mechanoresponsive and Mechanically Strong Hydrogels," *Adv. Mater.*, vol. 29, no. 21, p. 1606900, 2017.

[106] A. Buchberger, S. Peterka, A. M. Coclite, and A. Bergmann, "Fast optical humidity sensor based on hydrogel thin film expansion for harsh environment," *Sensors*, vol. 19, no. 5, pp. 9–12, 2019.

[107] Z. Zhang, A. S. Keys, T. Chen, and S. C. Glotzer, "Self-assembly of patchy particles into diamond structures through molecular mimicry," *Langmuir*, vol. 21, no. 25, pp. 11547–11551, 2005.

[108] P. Borckmans, P. de Kepper, A. R. Khokhlov, and S. Métens, eds., *Chemomechanical Instabilities in Responsive Materials*. Dordrecht: Springer Netherlands, 1 ed., 2009.

[109] National Center for Biotechnology Information, "PubChem Compound Summary for CID 6581, Acrylic acid." 2021. https://pubchem.ncbi.nlm.nih.gov/compound/Acrylic-acid. Online; accessed 16 March 2021.

[110] J. S. Laurence, B. N. Nelson, Q. Ye, J. Park, and P. Spencer, "Characterization of acid-neutralizing basic monomers in co-solvent systems by NMR," *Int. J. Polym. Mater. Polym. Biomater.*, vol. 63, no. 7, pp. 361–367, 2014.